University of California,

Irvine

Utilization of Integrated Electrochemical Devices for in-situ Methane Hydrate Recovery in Deep Ocean Sediments

Thesis

Submitted in partial satisfaction of the requirements

for the degree of

Master of Science

In Mechanical and Aerospace Engineering

By

Mohammad Ali Azizi

Thesis Committee:

Professor Jacob Brouwer, Chair

Professor Derek Dunn-Rankin

Professor Yun Wang

2014

Dedication

I dedicate this thesis to My Mother and Father. There is no doubt in my mind that they will be there for me no matter what.

Table of Contents

List of Figures

List of Tables

Nomenclature and Symbols

ANS	Alaska's North Slope
APEP	Advanced Power and Energy Program
ATR	Autothermal Reforming
BOP	Balance of Plant
CCS	Carbon Capture and Sequestration
DOE	Department of Energy
DOPSL	Deep Ocean Power Systems Laboratory
DSG	Downhole Steam Generator
EGHR	Enhanced Gas Hydrate Recovery
FOA	Funding Opportunity Announcement
GT	Gas Turbine
LBNL	Lawrence Berkeley National Laboratory
LSM	Strontium-doped Lanthanum Manganite
NETL	National Energy Technology Laboratory
NFCRC	National Fuel Cell Research Center
PCI	Precision Combustion Inc
PEM	Proton Exchange Membrane
SMR	Steam Methane Reforming
SOEC	Solid Oxide Electrolysis Cell
SOFC	Solid Oxide Fuel Cell
UCI	University of California, Irvine
YSZ	Yttria-Stabilized Zirconia

Acknowledgements

I would like to express my warmest appreciations to my advisors, Professor Jacob Brouwer and Professor Derek Dunn-Rankin from whom I learned priceless lessons and to whom I will remain sincere and indebted forever. They taught me lessons by their insight, intelligence, genuineness, and authenticity. I will try my best to follow their professionalism and considerateness.

I would like to express my respect and thankfulness to technical staff at the University Of California, Irvine for their support during implementation stages of my project. I would like to thank my parents for being always besides me while distant. I would like to thank everyone who has contributed even a minute part in my progress.

Abatract of The Thesis

Utilization of Integrated Electrochemical Devices for in-situ

Methane Hydrate Recovery in Deep Ocean Sediments

By

Mohammad Ali Azizi

Master of Science in Mechanical and Aerospace Engineering

University of California, Irvine, 2014

Professor Jacob Brouwer, Chair

Significant amounts of methane exist in the form of methane hydrates in deep ocean sediments. Utilizing these energy sources could meet the growing U.S. energy demand, reduce dependency on foreign fuel supplies, and move toward lower greenhouse gas and criteria pollutant emitting energy sources. Despite the great interest in this amount of stored fuel resources, these resources have not yet been significantly utilized because there is no energy efficient method for recovery of methane hydrates.

The primary goal of the this study is to evaluate the feasibility of integrating and using electrochemical devices to accomplish energy efficient dissociation of methane hydrate gases in deep ocean sediments. Concepts for integrating electrochemical devices (e.g., fuel cells), efficient electricity production from released gases are developed. The technical feasibility of these integrated systems for operation in hydrate reservoirs in deep ocean sediments will be evaluated using thermodynamic and heat transfer

methods.

To meet the project goal, five formal objectives are evaluated: 1) Evaluate electrochemical devices based upon performance characteristics for use in integrated systems for methane hydrate dissociation, 2) Conceptualize integrated system cycles comprised of electrochemical devices to operate in a methane hydrate field, 3) Develop integrated systems models for each of the integrated cycles, 4) Accomplish thermodynamic analyses of electrochemical cycle concepts including system , and 5) Detailed and dynamic evaluation of the best performing concepts and comparison to traditional methods.

Chapter 1

Introduction

It is expected that global energy consumption rise by 41% from 2012 to 2035- compared to 55% over the past 23 years (52% over the past 20 years) and 30% over the past 10 years [1].

Power engineers are interested in potential resources of hydrocarbon hydrates since these resources are two orders of magnitude larger than the current conventional estimated gas reservoirs.

1.1 Background of Hydrates

In this section a part of gas hydrate literature provided by [2] is summarized. Today, it is well known that there are vast reservoirs on earth. Technical applications of hydrates were found 150 years after their discovery. It is known that gas hydrates

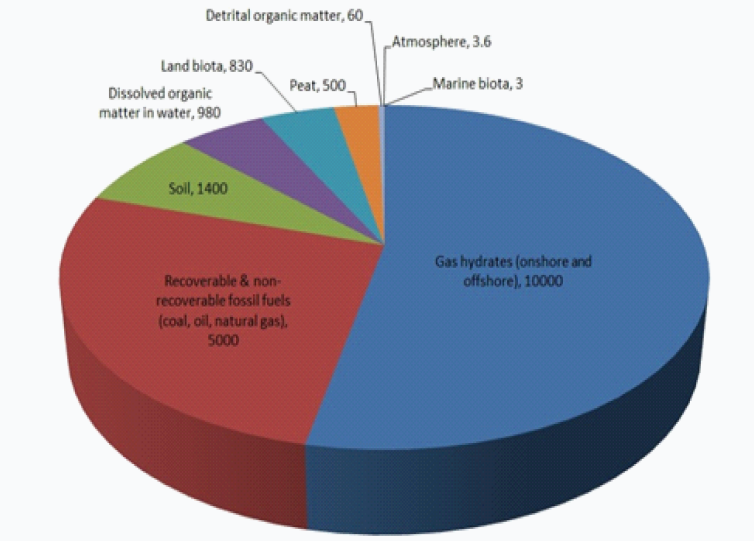

Figure 1.1: Distribution of oceanic carbon on earth, Numbers are in units of 10^{15} g carbon (Credit:USGS).

were first discovered in 1810 in the laboratory of Sir Humphrey Davy by cooling a liquid solution saturated with chlorine gas below 9° C. Hydrates of hydrocarbons. Pennwell Books.o obtain a crystal-ice material [3].

In another discovery, Joseph Priestley obtained hydrate of sulfur dioxide SO_2 from its water solution and from the gaseous phase and ice. He found the hydrate could be decomposed when put in an atmosphere of HCL, NH_3 and HF at atmospheric pressure and low temperature conditions, and it also keeps its state in the air. At that time, the effect of hydrate inhibition was discovered. It is known that SO_2-hydrate has been obtained by three researchers after Priestly and before Davy: T. Bergman (1783), A.F. de Fourcroy and L. N Vauquelin (1796, 1798), and A. F. de Fourcroy (1801) (Gmelins Handbunch, 1960).

More than 150 years after the gas hydrate discovery, they were only used for academic purposes. Hydrates did not have any application in the technological systems

at that time and hydrate properties could not be studied because of the technical limitations for their recovery. During that time, hydrates of several significant gases were made. Equilibrium plots have been presented at that time, and attempts to theoretically express the experimental results have been conducted on CO hydrates [4], H_2S , CH_4, C_2H_4, C_2H_2,N_3O and C_2H_6 hydrates and C_3H_8 hydrate [5]. It should be noted that, Villard was the first scientist who used the heat of the phase transition of hydrate formation for determination of the water/gas ratio of hydrate cage.

Villard and De Forcrand studied conditions of H_2S and CH_3Cl hydrate formation. He was the first one to use the Clausius-Clapeyron equation to specify the gas hydrates composition.

The first discovery of natural gas hydrates happened in the northern area of Siberia within the permafrost zone in *Messoyakhi* and *Ust-Vilyui* hydrate fields. Also, the first gas production from hydrate deposits was accomplished in these fields.

In the beginning of the 20th century oil and gas were world primary energy resources. Deep borehole drilling and deep oil recovery were producing significant amounts of natural gas which caused serious troubles for oil recovery technology and transport.

1930 and 1940 were the second technologically important decades in the history of hydrates. Main principles of hydrate plug formation and hydrate control were studied. Some of those methods are still being used today.[6] were the first scientists who demonstrated that individual gases and their mixtures can form hydrates in gaseous and liquid state. The most promising data in hydrate studies from 1930 to 1950 are

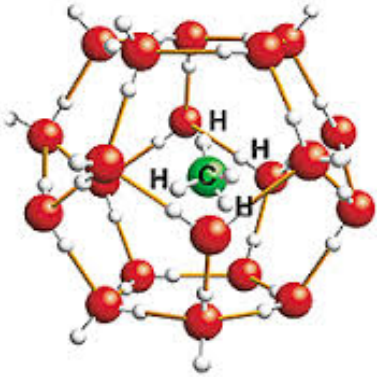

Figure 1.2: Sample of methane hydrate cage with methane molecule in the middle and surrounded by water molecules [99]

for D. Katz and R. Kobayashi[7]. In 1945, Katz reported a thorough equilibrium diagram that predicts the pressure and temperature of hydrate formation or dissociation. They also presented a diagram based on gas-solid phase equilibrium constants similar to water-vapor phase.

Today, leaders of hydrate research in the world are D.B. Robinson, E.D. Sloan, G.D. Holder, J.M. Brooks, M.S. Selim, P.R. Bishnoi, Y.P. Handa, H.J. Ng, V.A. Kammath, J.S. Tse, A. Vishniauskas and many others.

1.2 Hydrate Structure

In 1930s, researchers in Europe and Russian academia mostly studied the structure of crystal hydrates [8]. Fig. 1.2. shows a sample hydrate structure.

Nikitin, showed that hydrates of gases illustrate a crystal lattice built up from hydrogen and water molecules with cages contain gas molecules bonded to water by the weak Van der Waals forces. Stackelberg verified this theory by conducting X-

ray experiments and showing the two types of hydrate structure that also exist till today (Structure 1 and II) [9]. Davidson, Ripmeester, Tse and V.P Handa developed the experimental studies on hydrate structure types and hydrate thermal and electric properties.

Studies on technical area of gas hydrates started in 1934. Hydrate properties, formation and decomposition, effective systems of hydrate control in natural gas extraction systems and transport were among the main subjects of these studies.

1.3 Hydrate Formation Inhibition

Several methods of hydrate prevention in technological systems have been studied till now and the most promising ones are: thermal stimulation, chemical injection and inhibition, depressurization.

[10] developed several methods for hydrate prevention. The proof of hydrate existence was the hydrate saturated cores that were extracted during the exploration drilling in 1967. These explorations have been done at the Sredne-Viliuisk and Ust-Viliuisk fields in Yakutiya and at Messoyakhia field in Western Siberia [11]. Also ice cores containing air hydrate were extracted from the depth of 2164m at the American Antarctics station Byrd in 1968 [12].

1.4 Natural Gas Hydrate

The discovery of natural gas hydrate (Methane hydrate) first came from the Russian hydrate school, two hundred years after the first in-vitro hydrate discovery. The first proposal of hydrate existence was given by [13].

In 1963 a well drilled in *Markha*, North- West Yakutia, verified existence of permafrost rocks at depth of 1400 m. The possibility of hydrate formation in porous layers was investigated by Y.F. Makogon (1965, 1966) by analysis of thermodynamic data available that time and by comparing it with the results of studies on hydrate formation at the free gas-water contact.

Leading laboratories from several scientific centers in Russia, USA, Canada and other countries were attracted to the problem of natural gas hydrates. Methods of estimating hydrate gas resources and surveying of both onshore and offshore hydrate deposits were developed at that time.

1.5 World Hydrate Potential

World potential resources of hydrate methane were estimated by different authors and ranges from $7.6 \times 10^{18} m^3$ [14] to $3.1 \times 10^{15} m^3$ [15]. More Detailed examinations showed the potential resources to be $1.5 \times 10^{16} m^3$ [16]. Potential gas resources concentrated on earth in a hydrate state is more than $1.5 \times 10^{16} m^3$ ([16],[17]).

Sixty large hydrate main deposits have been discovered up to now in the ocean and

on the continents with total gas reserves greater than $700 \times 10^{12} m^3$.

Based on the current data, the portion of hydrate gas is estimated to be more than 15% in the next century.

1.6 Hydrate Types regarding Nucleation

The history of studies on natural gas hydrates has been presented in several articles. Today two major directions are distinguishable in hydrates: technogenic and natural gas hydrates.

Hydrates are solid cage like compounds whose properties and stability depend on the values of equilibrium thermodynamic pressure and temperature. If the hydrate dissociates, the rock formation becomes loose and loses its strength and stability. It should be noted that natural gas hydrate are dangerous during the recovery, drilling and operation of wells, platforms, pipelines and other offshore engineering structures and they should be treated carefully.

Hydrates easily form in producing wells or in gas and oil pipelines if they are in the stable region of the thermodynamic phase diagram. The prevention of hydrate formation needs significant investment as much as 15% of the productions cost. Removal of continuous hydrate plugs from an onshore and offshore pipelines costs $1 million and $3million respectively[2].

Some of the hydrate properties are unique. Pressure of free gas after dissociation of hydrate of methane in closed volume is up to 80-100 MPa.

Electrical resistivity of hydrates is usually very high. The specific volume of water while transitioning into hydrate state increases by 26-32%, whereas during freezing process the increase is about 9% which is considered high.

The main question is how to produce this amount of gas?

Gas hydrates are generally considered as chemical compounds since they have fixed composition. They are compounds of a molecular type initially formed because of the Van der Waals attraction forces between the molecules. Covalent bond is absent in gas hydrates because during their formation no pairing of valence electrons occurs[2].

1.7 Structural Forms of Hydrate

Generally Hydrates have six different structural forms [2]:

1. Molecular sieves characterized by interconnected cavity channels
2. Channel network when hydrate forming molecules form a crystalline
3. Layered network forming hydrate with interlaced molecular layers
4. Networks which form with large molecules
5. Polymeric networks formed by clathrate molecules, having a tube-like shape
6. fill in the closed cavities like sphere. Hydrate of gases and volatile liquids are related to this type of hydrates

Up to now, the unit cells of three hydrate structures have been determined. These hydrates have different sizes of molecules. Each unit cell includes a specified number of bonded hydrogen-water molecules. Size and shape of the unit cells are specified by

the size and the energy of the enclathrated hydrate former guest molecule.

Several potential gas hydrates are tabulated in Table.1.1. :

The basic cage of gas hydrate consists of a certain number of water and gas molecules. Molecular ratio of water and gas is a function of the size of the hydrate former gas molecules.

Generally in nature, hydrates have one of structures of type I or type II which will be described later in the text.

1.8 Impact & Benefits of the Study

Although new carbon-neutral renewable power (e.g., solar, wind, geothermal) will offset some of the growing worldwide demand for affordable power without significantly affecting climate, projections show that these alternatives will provide only a small fraction of the world energy need. There will be growing economic pressure to burn hydrocarbons and emit CO_2 into the atmosphere, with potentially devastating global environmental consequences. Hence, every feasible strategy for utilizing fossil fuels while limiting the carbon release should be examined.

The proposed research will improve the understanding of the dynamic characteristics of the SOFC system. If successful, the reversible SOFC's can be applied to not only to the methane hydrate dissociation system but also to hydrogen energy storage integrated with intermittent wind and solar power sources. This could be followed by much more commercial viability and marketability of SOFC technology with reversible

Alkane	**Alkenes, Alkynes, Aromatics**
Methane (I)	Ethylene (I)
Ethane (I)	Proylene (II)
Propane (II)	Isoburylene (II)
Isobutane (II)	Allenwe (II)
Butane (II)	Cis -2- Butene (II)
Neopentane (II)	2,3 Dimethyl-2-butene (H)
2 Methylbutane (H)	2,3 Dimethyl-1-butene (H)
2,2 Dimwthylbutane (H)	3,3 Dimethyl -2 butene (H)
2,3 Dimethylbutane (H)	Acetylene (I)
2,2.3 Trimethylbutane (H)	Methylacetylene (II)
Hexamethylethane	3.3 Dimethyl-2 butyne (H)
2,2 Dimethylethane	Benzene (II)
3,3 Dimethylethane	
Inorganics	
$O_2(II)$	
$N(II)$	
$H_2S(II)$	
$CO_2(II)$	
$SO_2(II)$	
$Cl_2(II))$	
$CFC's$	

Table 1.1: Several potential gas hydrates that are tabulated [2].

operating capabilities, and support the nations renewable power market to enable it to reach required levels. Reversible SOFCs are not currently available in the market. The research could improve high temperature and high pressure fuel cell system durability and marketability. Operating in simulated deep ocean environment, increased market penetration will be beneficial to the California electric market since SOFC systems have proven high fuel-to-electricity conversion efficiency with ultra-low pollutant emissions [18]. It is also known that SOFC performs at high pressures. The simulated high pressure fuel cell for hydrate recovery can also reveal benefits of high pressure fuel cell by Increased efficiency. These types of SOFCs are critical for future power generation and reduced greenhouse gas emissions. The ultra-low pollutant emissions support continuing efforts to reduce the environmental impact of methane hydrate dissociation.

Heat generation is the most promising method among other gas hydrate dissociation methods. The only state-of-the-art way to produce heat is by steam generators or combustors. Combustors generate more heat in comparison to fuel cells. However, downhole combustors require air or oxygen delivery to downhole and hydrate reservoir. The idea of heat production is that combustor can burn some of the dissociated fuel from hydrate reservoir. The determination of flow rate of methane needed for thermal stimulation device is one of the goals of this project. Fuel cells operated under high pressures have this advantage over combustors that they also produce electricity. The produced electricity could be delivered to the integrated high pressure electrolyzer in the proposed system. The rest of the energy is in form of heat that could dissociate the methane hydrate. In addition the exit CO_2 gas of high temperature fuel cell could be

used to produce more methane from gas hydrate by the process of CO_2/CH_4 exchange. Fuel cells are more energy efficient rather than heat engine due to the direct electrochemical conversion of the fuel. A fuel cell integrated with an electrolyzer will further increase the total efficiency compared to combustor since electrolyzer could produce portion of hydrogen fuel for SOFC.

Chapter 2

Hydrate Formation Condition

Hydrate formation conditions are specified during the design of the production technical aspects. The most exact parameters of hydrate formation from a real gas of complex composition can be obtained experimentally or theoretically. Hydrates can be divided into two main groups according to their initial formation:
1) Natural: which form and exist in nature with no human intervention. 2) Technogenic: which form in technological systems controlled by humans.

Natural and technogenic gas hydrates are identical in their basics, however the research goals and purposes are different.

2.1 Conceptual Problems regarding Natural Gas Hydrates

Conceptual problems regarding natural gas hydrate are:

1. Conditions of formation, accumulation , stability and dissociation
2. Discovery of hydrate formation zones offshore and onshore
3. Estimation of resources of hydrocarbons accumulated in natural gas hydrate
4. Preventing gas hydrate formations at oil and gas pipeline locations
5. Influence of natural gas hydrate on local and global environment
6. Development of technically feasible methods for natural gas hydrate extraction and recovery

2.2 Effects of Natural Gas Hydrates on Climate

Hydrates play a significant positive role in controlling the heat flow of our planet, and a potentially negative role by releasing a vast amount of methane gas into the atmosphere.

First experiments that studied the formation of natural gas formation conditions and parameters indicated that natural gas forms natural gas hydrate with rock water in porous media at appropriate P_T conditions [19]. The first world map of gas hydrate

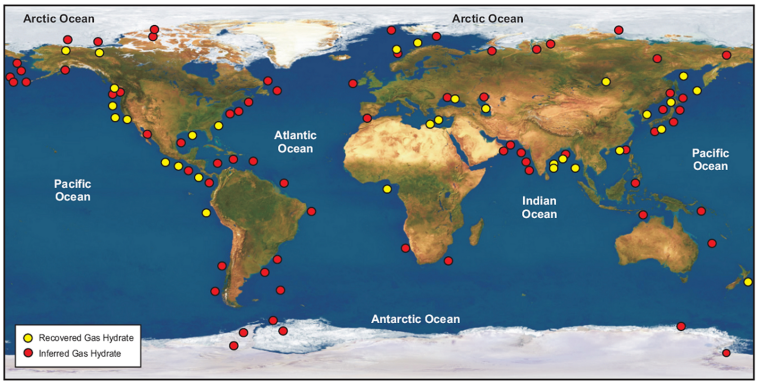

Figure 2.1: Main methane hydrate resources distribution on earth,[100]

deposits locations was reported in 1985, in which 23 fields were shown [2]. Fig. 2.1. shows the main methane hydrate resources.

2.3 Pressure and Temperature Conditions of operation Wells

In order to study prevention of hydrate formation, it is necessary to know the equilibrium conditions of hydrate formation from a gas of known composition and the change of gas flow parameters in the well. Dependence on the equilibrium temperature is determined by formulation of thermodynamic equilibrium conditions. Conditions for hydrate formation and accumulation in the reviewed part of the technological system exist at $P_w > P_{Hydrate}$ or $T_w < T_{Hydrate}$, where P_w and T_w are the equilibrium pressure and temperature of the operating system, and $P_{Hydrate}$ and $T_{Hydrate}$ are the pressure and temperature of the hydrate formation.

2.4 Technological Applications of Natural Gas Hydrates

Knowing the properties of hydrates, hydrate formation process, and a change of hydrate former characteristics during their transition from a free into a bounded hydrate state and back is needed to produce technologies. Change of specific volume during their transition from a free state into hydrate state or from a hydrate into a free state (by 9% during transition into ice state) is one property of hydrate. These properties are used in methods for storage and transportation for large volume of gas in a hydrate state at low pressures and to produce energy efficient methods without compressors to increase density for gases. Gas hydrates can be used for thermal compression of gases, generation of cold and energy production during the use of a low-potential heat.

Recently, a technology of using gas hydrates for desalinization of water was tested. Only water molecules go into a hydrate phase during hydrate formation and the minerals dissolve in water concentrate. During hydrate formation process, fresh water and mineral solutions will be separated, so we can use this method to provide fresh water for electrochemical devices such as electrolyzers that can operate using fresh water. Water vapor pressure is lower around hydrates than water in free state. This property can be used in gas drying process. Different gaseous and liquid hydrate formers produce hydrate at different thermodynamic parameters. So the methods of separation and dissociation are based on the properties of gases.

2.5 Composition of Gas and Conditions of Natural Gas Hydrate Formation

The first work regarding natural gas hydrates was for methane gas. Calculations of the amount of energy stored in hydrates are based on the amount of methane stored in hydrate cages. However, several cores have shown the very different methane percentage in gas hydrates after drilling. In real conditions, generation of gas water saturated sedimentary rock is accompanied with active migration of gas and water. Knowing the component and isotopic composition of gas in a hydrate, one can predict the stability of hydrate for an extended period of time. At a ratio of $\frac{CH_4}{C_2H_6 + C_3H_8} \geq 100$, gas is usually of biogenic origin. At $\frac{CH_4}{C_2H_6 + C_3H_8} \geq 80$ gas has thermogenic origin.

2.6 Conditions of Natural Gas Hydrate Formation

At normal thermodynamic conditions, hydrates are stable in the presence of liquid water and methane gas at certain pressures and temperatures. The process of hydrate formation has common basis when they form from free water and gas. Also, conditions such as capillary pressure, surface tension, salt content of fluid, and properties of the medium should be considered during the process of hydrate formation. The gas hydrate formation process is catagorized as following:

1. Formation of hydrates from dissolved gases: in this case the rate of hydrate formation is determined by diffusive influx of gas from water

2. Formation from free gas in the pores : This case of formation is because of change in thermodynamic equilibrium parameters

Chapter 3

Current State of Methane Hydrate Dissociation Technology

The earth stores significant quantities of methane (about 10 times of the conventional storage of natural gas) in ice-like methane hydrates buried in sediments deep beneath the ocean surface, and in permafrost. The volume of oceanic methane hydrate is poorly known, but, based on NETLs 2011 report [20] the amount of natural gas in hydrate form is estimated at 20000 trillion cubic meters. Methane hydrate deposits are abundant throughout the world and have been estimated to represent the greater portion of the worlds fossil energy reserves. Estimates of hydrate natural gas on the North Slope of Alaska are in the 10's of trillions of cubic feet, with additional 100's of trillions of cubic feet in other areas in the same region, and on the order of 1,000's of trillions of cubic feet beneath the U.S. continental margin. Energy efficient extraction

of these fuel resources could fulfill the U.S energy demand for many years. Despite the great interest in this amount of stored fuel resources, there is no energy efficient method for mining methane hydrate. Methane hydrate is not stable in sea level conditions, therefore methods for in-situ energy efficient dissociation of gas hydrate and delivering it to the sea surface with little contamination are required. Highly specialized tools and facilities for collecting gas hydrate samples and analyzing them with minimal contamination and disturbance are also significant challenges, even before considering strategies for hydrate mining.

Engineering extraction efforts are under processing in China, Korea, Japan, and Norway [21]. One possible strategy, and the subject of this thesis, for dissociation of the methane, is the in-situ (deep ocean environment) utilization of integrated electrochemical systems based primarily upon the use of high temperature Solid Oxide Fuel Cell (SOFC) technology system. Such systems have unique features of oxygen extraction from water, efficient electricity production from released gases, and both heat and CO_2 production for methane hydrate gas dissociation that may be useful in methane dissociation from hydrate fields.

Currently, many projects are being conducted by the government agencies, industry and academia to probe the dissociation, utilization and the potential impacts of methane hydrates. ConocoPhillips conducted an experimental study at Ignik Sikumi#1 well in the Prudhoe Bay unit on Alaska's North Slope (ANS). This study evaluated the results of a field trial for methane hydrate production by the injection of carbon dioxide (CO_2) molecules that are exchanged in situ with methane molecules within

a hydrate structure, releasing the methane for the production and use [22]. In this study, about 210,000 standard cubic feet of mixed carbon dioxide/nitrogen (CO_2/N_2) gas was injected into the targeted hydrate-bearing portion of the well. There was sustainable flow-back of gas from the well over an extended portion of approximate 30 days of the production period. In addition, data from the well, including temperature, pressure and gas compositions (CO_2, CH_4, N_2) and constituent volumes was collected. From these data, the temperature behavior of the injection fluid and the heating capacity of hydrate sediments have been studied [22]. Laboratory experiments conducted by ConocoPhillips have suggested that exchange of CO_2 and CH_4 is possible without forming further secondary hydrate and while maintaining high hydrate saturation [22]. The Georgia Tech Research Corporation has conducted an experimental study on gas replacement as a potential production mechanism to reduce reservoir deformation and closure in fine-grained systems. In this study, CO_2 molecules replace CH_4 molecules within the larger cages; the heat released in this exchange could maintain overall reaction. The addition of nitrogen to carbon dioxide, promotes further exchange where by the smaller nitrogen molecule can replace methane in the smaller cages increasing methane production from 64% to 85% ([23],[24]). Also, nitrogen can prevent condensation to hydrate phas. ConocoPhillips study concluded that nitrogen alone will cause methane hydrate dissociation (accompanied by lowering the reservoir temperature) [22]. The pressure vs. temperature phase equilibrium diagram for hydrate mixtures of varying molar percent concentrations of carbon dioxide and nitrogen gas is demonstrated in [25] and [26].

Precision Combustion Inc (PCI), has conducted a study to demonstrate a novel, oxyfuel downhole steam generator (DSG) that will efficiently recover gas from methane hydrate deposits while reducing emissions and also having the potential for carbon dioxide (CO_2) sequestration [27]. Results from this project show that natural gas can be produced from its hydrate at an energy cost of approximately 15% of the heating value of the produced gas. This study showed 15% methane consumption for its production from hydrates, as predicted by their model. Instead of steam, CO_2 could be used as an injection gas; however, we should consider that CO_2 injection may affect the produced natural gas quality. On the other hand, overall production may be enhanced through exothermic formation of CO_2 hydrates [20].

Lawrence Berkeley National Lab evaluated the gas production potential of the Mt. Elbert hydrate deposit and other North Slope accumulations by simulation. By solving coupled equations of mass and heat balance they modeled non-isothermal gas release, phase behavior, and flow of fluids and heat under conditions for common natural methane (CH_4)-hydrate-bearing deposits in complex formations. This model can be applied to a variety of hydrate dissociation mechanisms, e.g., depressurization, thermal stimulation, salting-out effects, and inhibitor-induced effects and has been used to evaluate long term hydrate production capabilities at various sites within Prudhoe Bay and Milne Point [[20], [28]-[32]].

Georgia Institute of Technology, conducted research on Gas production during depressurization, heating, and $CO_2 - CH_4$ replacement. They have used 2-D experiments data to simulate the thermodynamics and transport process of hydrate dissociation [33].

Battelle Pacific Northwest Division, conducted research on a comparative study of conventional and innovative approaches for producing methane from gas hydrate-bearing geologic reservoirs through numerical simulation. According to this study, the most promising method to produce hydrate accumulation is to make a hydrate free zone at the injection location ([34],[35]).

Rice University has conducted research that shows the CO_2-hydrate energy of formation will keep the desired temperature for the methane hydrate dissociation process [36]. They have also determined the velocity of the hydrate dissociation front or the rate of hydrate dissociation. They have studied the method in which warm water is utilized as a potential for hydrate dissociation. One of the primary goals of this project was the simulation of the total mass production of methane for different injection pressures and temperatures. Their study has shown that despite the fact that the depressurization method has high energy efficiency in dissociation, it has relatively low production rate in comparison to the warm water injection approach [36].

In this thesis, feasibility of the integrated electrochemical devices (e.g., fuel cells) and hydrate reservoir in deep ocean sediments, based on thermodynamic principles, will be examined. Thermal stimulation and CO2 injection dissociation approaches are investigated in this effort. Electrochemical devices proposed have very high energy conversion efficiency and may improve the current approaches of methane hydrate dissociation in the field studies. As provided in the literature, there are three main methods for gas recovery from hydrates:

1. Depressurization: In which by drilling wells in sediments and making lower pressure

than stable hydrate pressure around it, the gas hydrate will dissociate.

2. Thermal Stimulation: In this method hydrate decomposition will happen by thermally stimulating hydrate sediments at higher temperatures than the stable hydrate temperature.

3. Chemical inhibitors.

It is well known that major parameters governing methane hydrate stability are pressure, temperature and water salinity [37]. Modeling gas hydrate dissociation requires knowledge of the thermodynamic properties of hydrate at which it is stable. However, at equilibrium of three phases in pure water, the dissociation pressure of gas hydrate is a function of temperature and several experimental relation express theses relations ([38],[39]). Salinity is the other factor which has an effect on methane hydrate dissociation. [37] have found that salinity of water would decrease the chemical potential of water and the equilibrium would shift to methane production and consequently to methane hydrate dissociation. They have also calculated the effect of pressure on water activity. Thermodynamic equations of stability and solubility of methane hydrate were developed in this study using the method of Pitzer. . Dissociation pressures are calculated for different temperatures and salinities from 273 to 293 K and 0-70 ppt respectively. They have calculated the solubility of methane and methane hydrate in seawater. In contrast to previous methods, their approach calculates solubility parameters by considering a continuous variation of the control parameters over a wide range of conditions that are met in the deep ocean environment.

Duan et al., have calculated the fugacity of methane and coefficients of the equation

of state for $CH_4 - CO_2 - H_2O$ system based on second virial coefficients in deep ocean sediments. Numerical calculations of dissociation pressure at the temperature range of 273-293 [K] and water salinity of 0-70 ppthas been done by their research group ([40] , [41] and [42]). They have also concluded that the fugacity coefficient of CH4 in the vapor phase of $CH_4 - H_2O$ mixture differs very little from that in pure CH_4 for temperatures below 250°. They have presented a thermodynamic model to calculate methane solubility, liquid phase density and gas phase composition of the H_2OCH_4 and H_2OCH_4NaCl systems from 273 to 523 K , from 1 to 2000 bar and from 0 to 6 $mol.kg^{-1}$ of $NaCl$ with experimental verification.

[43] studied gas bubbles released from three vents of Louisiana at a water depth of 500m in the vicinity of hydrate deposits. The estimated methane released is from 0.026 (for oily vents) to 0.853 g/s (Pulsing vents). The bubbles had upward velocities of 0.026 (for oily vents) to 0.853 g/s [26]. It has been found that crude oil is the common component of emission from Gulf of Mexico seeps. [44] has studied gas discharge at the Northern summit of hydrate by pressure change to be in th order of 6×10^4 mol/day. Methane flux out of bacterial mat-covered sited was found to be 30 to $90\frac{mmol}{m^2day}$. They have collected samples with benthic instrumentation and from Alvin push cores and discovered a complex hydrogeologic system where fluid and methane fluxes from the seafloor vary by several orders of magnitude at sites separated by distances of only a few meters.

[45]has parametrically studied methane hydrate dissociation in oceanic sediments by thermal stimulation for different values of permeabilities. They have computed a

semi-analytical model of the problem based on local equilibrium and build upon previous studies in order to obtain further insight on the effects of various parameters that can affect methane production. They have examined parameters including permeability, porosity, and thermodynamic/transport properties of the system. In their work it is shown that, in contrast to previous studies on permafrost, for the case of oceanic sediments (low permeabilities), the rate of hydrate dissociation depends on the permeability of the porous sediments. Hydrate saturation values for Malik 2L-38 site at the arctic Mackenzie Delta are reported to be 35-40% and at the Northern Cascadia Margin is around 20-35%[46] . The hydrate saturation in some cases exceeded 80% [47].

[48] has calculated the pressure drop that is required to initialize the hydrate dissociation as a function of sediment temperature. In the region where the pressure is close to the dissociation pressure, it is reasonable to use depressurization as the main gas production method. However, For deposits that need very high pressure drop such as Black Ridge-1 (200bar), Mexico-2(250bar), Costa Rica(260bar), Peru-Chile-2(305bar), Nankai-2(415 bar) and Peru-Chile-1(430 bar) it is not reasonable to use depressurization, and other methods should be used . [49], conducted a comparative study of several depressurization and thermal injection numerical models and concluded that two models of (TOUGH2 developed at LBNL and in-house model) have the necessary features to describe field-scale, multi-phase methane hydrate recovery.

[32] developed the EOSHYDR2 module to model the nonisothermal methane release. The objective of that study was to analyze the various gas production scenarios

from five methane hydrate-bearing zones at the Mallik site. In Zone#1, numerical simulations using the EOSHYDR2 model indicated that gas production from hydrates at the Mallik site was possible by depressurizing a thin free gas zone at the base of the hydrate stability field. Zone #2 showed that a gas hydrate layer with an underlying aquifer, could yield significant amounts of gas originating entirely from gas hydrates, the volumes of which increased with the production rate. Zones #3, #4 and #5 were isolated gas hydrate deposits with no underlying zones of mobile gas or water. In these zones, thermal stimulation by circulating hot water in the well was used to initiate dissociation process.

[50] studied the feasibility of modeling gas production from hydrate capped gas reservoir using the 3D simulator. These investigations show the role of excessive water production and the requirement for water handling facilities. ([51],[52]) created numerical model to simulate the isothermal process of gas production from Berea sandstone by the depressurization mechanism. They developed experiments for hydrate dissociation. predicted the natural hydrate formation using depressurization and decomposition kinetics in hydrate dissociation .[54] conducted analytical approach to model gas hydrate production during hydrate decomposition.

[55] investigated the feasibility of hydrate production from a thermodynamic point of view and determined that the gas production is possible by thermally stimulating the hydrate sediments. [56] determined the upper and lower bounds on gas production and energy efficiency for a cyclic steam injection process .[65] treated the hydrate dissociation process as a 1-D mathematical model under thermal stimulation. They have

modeled hydrate dissociation as a moving boundary ablation process and extended their model to thermal stimulation by hot water injection [58]. [57] conducted experiments to calculate the rate of methane dissociation under a constant heat flux thermal source . [59] proposed a mathematical model of the dissociation process that contains two movable phase transition boundaries (hydrate dissociation and ice melting fronts) and solved it using similarity transformations.[60] proposed a numerical new approach for hydrate recovery using magnetic thermal stimulation of hydrate sediment using vertical and horizontal wells.[61] has modeled the methane hydrate dissociation using a combustion heat source. They have also investigated CO_2 hydrate formation. This method has been shown to significantly reduce the total energy input and verified the fact that CO_2 could be sequestered to produce further methane from hydrate sediments. Their results have indicated that it is possible to reach total energy efficiency of 90% for land based reservoirs in the case that hydrate loading is 20%. [63] and [56] suggested that thermal stimulation is most attractive for gas hydrate dissociation. [64] presented an approximate solution to the ablation problem using the heat balance integral method with a second degree polynomial approximation for the temperature profile. Lawrence Berkeley National Lab evaluated the gas production potential of the Mt. Elbert hydrate deposit and other North Slope accumulations by simulation. By solving coupled equations of mass and heat balance they modeled non-isothermal gas release, phase behavior, and flow of fluids and heat under conditions for common natural methane (CH_4) hydrate-bearing deposits in complex formations. This model can be applied to a variety of hydrate dissociation mechanisms and has been used to evalu-

ate long term hydrate production capabilities at various sites within Prudhoe Bay and Milne Point ([28]-[32]). Georgia Institute of Technology, conducted research on Gas production during depressurization, heating, and $CO_2 - CH_4$ replacement. They have used the 2-D experiments data to simulate the thermodynamics and transport process of hydrate dissociation [33].

3.1 Technical Feasibility Issues of Methane Hydrate Dissociation

The literature and our analyses suggest that there is no clearly superior or more energy efficient approach for deep ocean dissociation of methane hydrates. The methods based on CO_2 injection have slow kinetics. The methods of depressurization have slow production of methane. One of the most promising methods for hydrate dissociation is thermal stimulation. Experiments at Mallik hydrate sites show that thermal stimulation in the several zones (e.g., Zones# 3-5) that do not have underlying layers of mobile gas or water can produce more methane from hydrate reservoirs than does the depressurization method [32].

Most proposed techniques for recovering the natural gas from hydrate require too much energy input, raise safety concerns, or can only recover a fraction of the gas. This thesis research will investigate the use of the unique high efficiency and oxygen recovery from water characteristics of electrochemical devices to explore the technical

feasibility of novel integrated electrochemical systems for gas production in deep ocean hydrate reservoirs. As mentioned earlier, in one related study [61], the in-situ methane recovery method produced a heat source at the location of hydrate formation. In another study, in which mass production of methane has been simulated for different injection pressures and temperatures, results show that the depressurization method has a relatively slower production rate than the warm water injection approach. This study shows that the bare utilization of depressurization method has lower efficiency of methane recovery compared to the method that utilizes both depressurization and thermal stimulation [36].

Chapter 4

Northern California Hydrates state of the art

In this section a part of the northern California hydrate reservoir provided by [66] is summarized. Gas hydrates have been recovered in gravity cores within 10 m of the sea floor in sediment of the Gulf of Mexico, the offshore portion of the Eel River basin of California, the Black Sea, the Caspian Sea, and the Sea of Ok- hotsk [67]. Both Mendocino and Humboldt counties have vast reservoirs of oil and natural gas hydrates and most of them are just offshore. Today, Japan has made the most significant research development in methane hydrates and appears to be the closest to commercial production. Experiments show that hydrate formation is rapid in natural gas and sediment type affects the hydrate formation kinetics. In 1996, in-situ experiment has shown that the hydrate formation at Monteray hydrate bed is possible. Studies confirm

the indirect geophysical and geologic observations that gas hydrates are present north of the Mendocino Fracture Zone in sediments of the Eel River basin. The margin of northern California was surveyed in 1977, 1979, and 1980 by the U.S. Geological Survey to examine both the geologic framework and active geologic processes. During each survey, navigation systems accurate to 50 m were employed, and deep-penetration and high-resolution seismic reflection profiles were collected. ‘ The first evidence of gas hydrates in this region was reported by [68]. Their study identified the widespread (areal extent, $>$ 3000 km z) presence of a BSR in sedimentary strata of the offshore Eel River basin. The geology of the Eel river basin is described by [68] and [69]. Details of the margin structure were given by [70]. The gas-hydrate zone inferred by [68], extends for more than 130 km along the California margin and continues onto the Oregon margin. Gas hydrates were recovered or suspected at seven sites in the Eel River basin of northern California at water depths between 510 and 642 m. A total of seven gas-hydrate containing cores were recovered out of 74 cores taken in water depths below 500 m in the Eel River basin. The recovered gas hydrates consist mostly of methane and small amounts of ethane. Sediment samples collected from one of the cores revealed thermogenic hydrocarbons, which indicates that some natural gas is present in the offshore Eel River Basin [36]. Seismic records from both sound sources showed an extensive bottom-simulating reflector (BSR) which shows the base of a zone cemented by a natural-gas hydrate below the sea floor. Acoustically, inferred gas hydrate we discuss here was previously identified by Field et al. (1980) and Biddle and Seely (1983) and is the first to be noted in sediment on the western continental

margin of the conterminous United States.

[71] evaluated the potential geological distribution of gas hydrates in Northern California and found that the major regional differences between the areas north and south of the Mendocino Fracture Zone are likely to form gas-hydrate in the north (Eel River). They have estimated the possible gas-hydrate resource north of the Mendocino Fracture Zone of 1 trillion cubic feet (TCF) per 1 meter thickness of hydrate-bearing sediment (average thickness of the MFZ is 250 m).

Using standard phase boundary diagrams for hydrate stability, It is estimated the local geothermal gradient within the gas hydrate to be about 55 C/km [68]. Phase boundary diagram applied to inferred gas hydrates off northern California, showing geothermal gradients derived for three depths: (1) Minimum water depth of 725 m and related BSR at 135 m; (2) Typical water depth of 1000 m and related BSR at 225m; and (3) Maximum water depth of 2000 m and related BSR at 315 m. It is found that gas and pore-fluid migration in the offshore Eel River Basin is: (1) Associated with surface morphology; (2) Helps to seabed roughness; (3) A significant mode of sediment redistribution on the upper slope; and (4) A factor in significant slope failures. In the Eel river Basin, enough gas and elements necessary for over-pressurizing fluid are present. The regional presence of large amounts of gas is indicated onshore by the Tompkins Hill gas field, which has an expected recovery of over 3.34 km3 (120 bcf) of natural gas [72]. In an attempt to quantify the role of water column methanotrophy (microbial methane oxidation) as a control on methane release, water column methane profiles are measured (concentration and $\delta^{13}C$) and oxidation rates at eight stations

in an area of active methane venting in the Eel River Basin, off the coast of northern California.

There is an enormous natural gas basin off the Humboldt Coast 90% of Eel river natural gas hydrates are offshore. Little work has been done on the production potential and technical feasibility of gas hydrate recovery. It is reported that one exploration well has reached 9500 feet depth. Production zones are reported at 4000 to 6000 feet and 9400 feet. It is reported that production wells will use fracture stimulation technique. Biogenic gas hydrates were recovered in shallow cores (higher than 6m deep) from the Eel River basin in offshore northern California.

The gas hydrates contained primarily methane and occurred as spread crystals, small nodules, and layered bands within the sediment. These hydrates, recovered in sediment at water depths between 510 and 642 m, match with areas that show bottom- simulating reflectors (BSRs) on seismic-reflection records. This study confirms geophysical and geological observations that gas hydrates are present north of the Mendocino Fracture Zone in sediments of the Eel River basin. This discovery extends the confirmed sites of gas hydrates in the eastern Pacific region beyond the Peruvian and Central American margins to the northern California margin. The other deep-sea collections of gas hydrates have resulted from deeper coring studied by the Deep Sea Drilling Project (DSDP) and the Ocean Drilling Program (ODP) in the Blake Bahama Outer Ridge. Offshore northern California is one of at least 30 offshore localities worldwide with inferred gas- hydrate reservoirs [73].

California's northernmost large onshore part of the offshore Pacific Coast Tertiary

basin is the Eel River basin. The main part of the basin, in the Eel River Valley area, contains approximately 12,000 ft of Tertiary and Quaternary sedimentary rock ranging in age from late Miocene to late Pleistocene and Recent. The federal Minerals Management Service estimates that there is 2 trillion cubic feet of natural gas in those deposits, mostly in the Eel River area.

4.1 Distribution of Northern California gas Hydrates

The gas-hydrate zone inferred by [68], extends for about 130 km along the California margin and continues onto the Oregon margin.

Gas hydrates were recovered or suspected at seven sites in the Eel River basin of northern California in water depths between 510 and 642 m. The hydrates were recovered as part of a surface geochemical exploration program in offshore northern California in the Eel River and Point Arena basins. A total of seven gas-hydrate containing cores were recovered out of 74 cores taken in water depths below 500 m in the Eel River basin.

A high percentage (about 10%) of gas hydrates collected in the Eel River basin which indicates that gas hydrates are common phenomenan in the shallow sea-floor of the Eel River basin. Krason and Ciesnik (1986) evaluated the geologic distribution of gas hydrates in northern California and found that the major regional differences

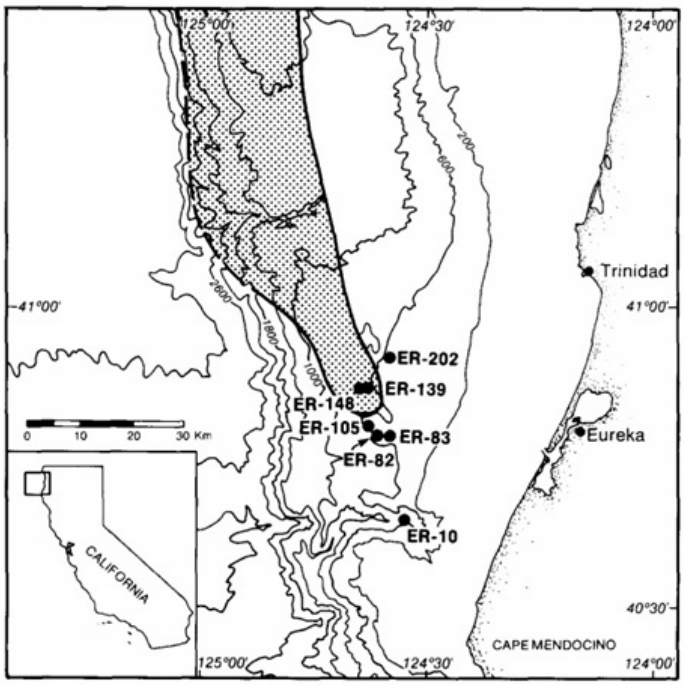

Figure 4.1: Showing the extent of gas hydrates inferred from BSR in seismic reflection records and location of the cores [102]

between the areas north and south of the Mendocino Fracture Zone seem to favor gas-hydrate formation in the north (Eel River) while preventing hydrate occurrence south of the fracture zone (Point Arena)[71]. Plate convergence north of the Mendocino Fracture Zone has produced thick forearc- basin deposits that are gas prone.

4.2 Northern California Composition of Gas Hydrates

Hydrogen sulfide, detected by smell, was present in all the gas-hydrate-containing cores. Analyses show that the gas hydrates are primarily biogenic in origin. Table.4.2

Core	**Latitude**	**Longitude**	**Water depth(m)**	H_2S
ER-10	40°38′14.32”	124°32′35.52″	510	Yes
ER-82	40°47′08.23”	124°35′33.12″	512	Yes
ER-83	40°47′08.31″	124°35′26.4″	518	Yes
ER-105	40°48′31.44″	124°37′38.58″	567	Yes
ER-139	40°52′27.49″	124°38′33.13″	623	Yes
ER-148	40°52′45.85″	124°39′16.00″	642	Yes
ER-202	40°56′51.18″7	124°34′28.71″	559	Yes

Table 4.1: Gas hydrate locations in Eel River basin, Northern California [102]

shows the molecular and isotopic compositions of the decomposed gas.

The inner continental margin of northern California is 50 to 80 km wide and composed of a near-shore shelf and an offshore plateau system that extends to water depths of more than 1000 m. The plateau system is a sloping surface lying 600 to 1000 m deep that is bounded on the seaward side by a steep continental slope. Much of the shelf and the plateau are underlain by the Eel River Basin, a thick Neogene and Quaternary sedimentary sequence. In the area of Eureka, the Eel River Basin extends inland about 50 km; offshore, it trends 200 km north-northwest to the vicinity of Cape Sebastian, Oregon. Pliocene and Quaternary deformation have produced numerous folds and faults that largely parallel the north-northwest basin trend ([74], [75]). Sediment samples collected from one of the diapirs yielded thermogenic hydrocarbons, in dictating that some natural gas is present in the offshore Eel River Basin [68].

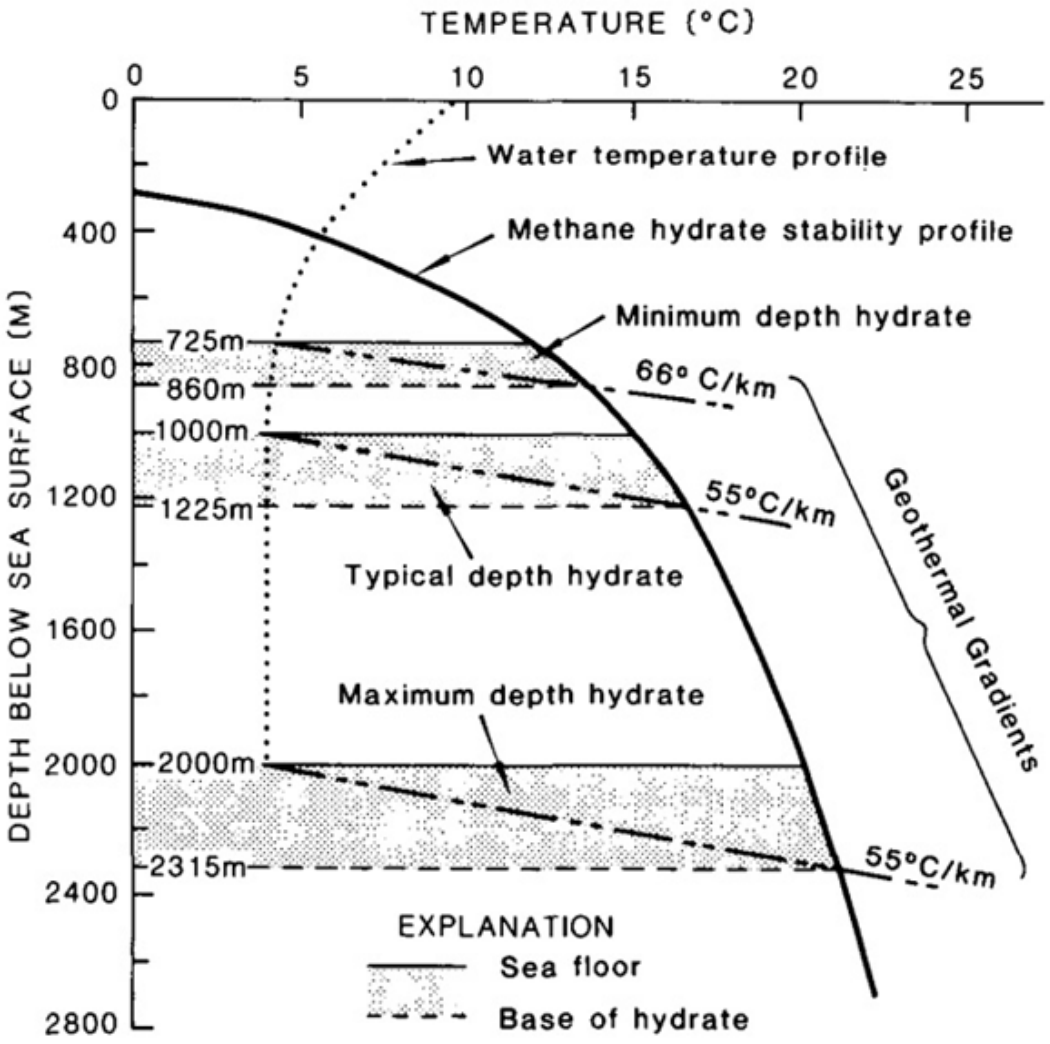

Figure 4.2: Phase boundary diagram applied to northern California hydrates [68]

Core	**Methane**	**Ethane**	**Propane**	$\delta^{13}C - C_{1\%}$	$\delta^{13}C - C_{2\%}$	C1/C2	Depth in the core
ER-10							1.8
ER-82	66.3	0.03	Not determined	9.6		2209	0-0.3
ER-83	92.9	0.02	Not determined			5158	$\prec$ 1.5
ER-105	93.2	0.01	Not determined	57.6		10591	0-0.2
ER-139	93.4	0.12	Not determined	61.1		803	1.8-2
ER-148	90.5	0.02	Not determined	59.7		5324	0-1.8
ER-202	86.6	0.05	Not determined	69.1	27.1	1603	2.2-2.8

Table 4.2: Gas hydrates composition in Eel River basin, Northern California, [102]

The margin of northern California was surveyed in 1977, 1979, and 1980 by the U.S. Geological Survey to examine both the geologic framework and active geologic processes. During each survey, navigation systems accurate to 50 m were employed, and deep-penetration and high-resolution seismic reflection profiles were collected. Seismic records from both sound sources showed an extensive bottom-simulating reflector (BSR) which we believe represents the base of a zone cemented by a natural-gas hydrate below the sea floor. There are at least 12 localities worldwide where the presence of bottom-simulating reflectors suggest the presence of gas hydrates beneath continental margins [37]. The acoustically inferred gas hydrate was previously identified by Field et al. (1980) and Biddle and Seely (1983) and is the first to be noted in sediment on the western continental margin of the conterminous United States. The BSR is attributed

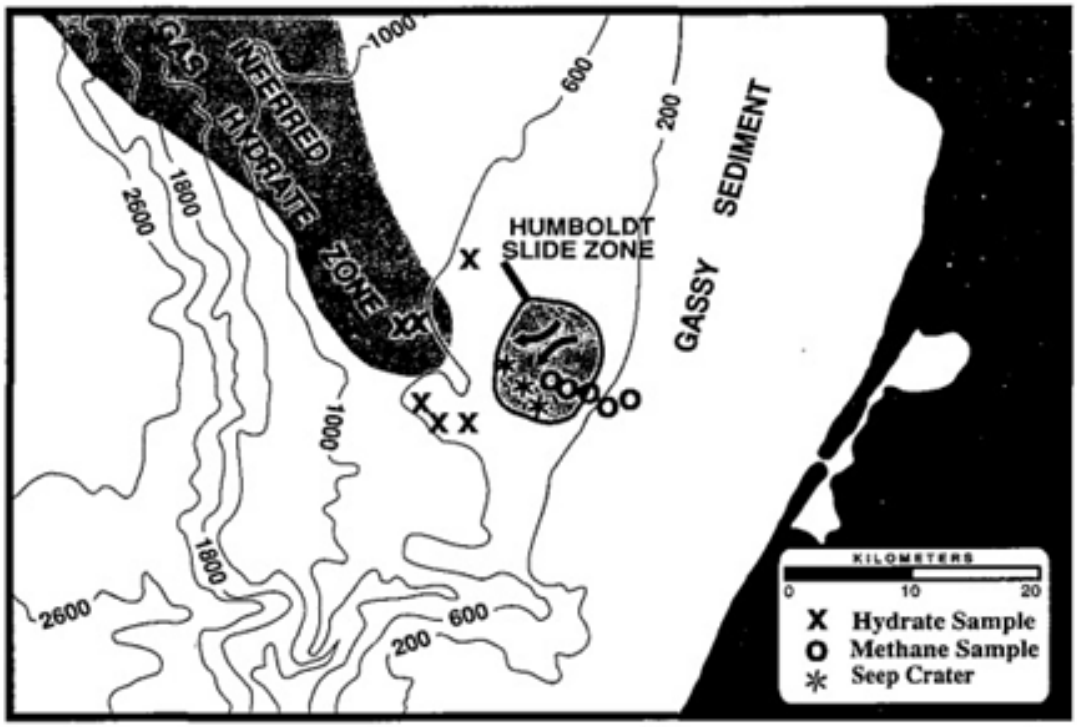

Figure 4.3: Study area showing the relationship between the location of Humboldt slide zone and observations of shallow gas and gas hydrates. The arrows indicate the direction of the movement [103]

to gas hydrate because it occurs at depths that satisfy the pressure-temperature requirements for gas-hydrate stability and because the BSR becomes deeper in the sediment with increasing water depth.

The geologic setting of the Eel river Basin helps to the presence and migration of gas and overpressurized fluid. Convergence between the Gorda and North American plates at 2.5 to 3 cm/yearhelps drive fluid overpressuring by the processes of tectonic compaction, cementation, and deformation[76]. Sources of methane in both models for gas hydrate formation discussed previously, the methane is considered to be mainly microbial in origin. This conclusion is based on geochemical investigations of recovered

gas hydrates and of hydrocarbon gases from sediment sections known to contain gas hydrates, such as occur offshore from the southeastern United States, northern California, and Peru, and in the Black Sea and at some sites in the Gulf of Mexico (Table 1). Methane in all cases constitutes more than 99% of the hydrocarbon gas mixtures.

Regions	**Type of Sample**	$CH_4, \%$	$\delta^{13}C, \%$	**Reference**
Offshore SE United States, Black Outer Ridge				
DSDP leg 11	sediment	≥ 99	-88 to -70	Claypool et al. [1973]
DSDP leg 76	sediment	≥ 99	-93.8 to -65.4	Kvenvolden et al. [1983]
	gas hydrate	≥ 99	-68	Brooks et al
Offshore Peru, Peru-Chile Trench				
ODP leg 112	sediment	≥ 99	-59 to -55	Kvenvolden et al. [1990]
ODP leg 112	gas hydrate	≥ 99	-65 to -59 .6	Kvenvolden et al. [1990]
Offshore northern California				
Eel River Basin	gas hydrate	≥ 99	-69.1 to 57.6	Brooks et al. [1991]
Black Sea	gas hydrate	≥ 99	-63.3, -61.8	Ginsburg et al [1990]
Gulf of Mexico				
DSDP leg 96		≥ 99	-73.7 to -70.1	Pflaum et al. [1986]
DSDP leg 96		≥ 99	-71.3	Pflaum et al. [1986]
Garden Banks		≥ 99	-70.4	Brooks et al. [1986]
Green Canyon		≥ 99	-69.2,-66.5	Brooks et al. [1986]
Green Canyon		62,74,78	-44.6,-56.5, 43.2	Brooks et al. [1986]
Mississippi Canyon		97	-48.2	Brooks et al. [1986]
Caspian Sea	gas hydrate	59 to 96	-44.8 to -55.7	Ginsburg et al. [1992]
Offshore Guatemala, Middle America Trench				
DSDP leg 84	Sediment	≥ 99	-71.4 to -39.5	Kvenvolden and McDonald [1985]
DSDP leg 84	gas hydrate	≥ 99	-43.6 to -36.1	Kvenvolden et al [1984]
DSDP leg 84	gas hydrate	≥ 99	-46.2 to -40.7	Brooks et al [1985]

Table 4.3: Carbon isotopic composition and concentration of methane in natural gas hydrates [101]

Chapter 5

Malik Zones Parameters

The parameters that was used by [77] were, porosity ($\Phi = 0.28$), intrinsic permeability , ($k = 2 \times 10^{-14} m^2$), composite thermal conductivity of rock reservoir fluids system ($k_\theta = 1.5 \frac{W}{m.C}$), Rock specific heat, $c_R = 800 \frac{j}{kg.C}$, Hydrate specific heat, $c_H = 1600 \frac{j}{kg.C}$.

Zone I is the deepest hydrate accumulation at Malik site, and has 20m hydrate bed thickness the base of which is at (-1108.4 m) (hydrate stability zone). The initial temperature at the bottom of the hydrate layer is $T = 13.18°C$ which is the gas hydrate equilibrium temperature T_H at the formation pressure of $P = 10.8 Mpa$. Gas hydrate interval has a uniform hydrate saturation S_H=0.8 and water saturation of S_W=0.2. Fluids were produced from the well at cumulative mass flow rate of $Q = 1.67 \times 10^{-3} kg/s$ using trial and error. They have calculated the mass fraction of methane in production well while hydrate dissociating. They have shown that gas is the only component

only for six days of production. After the sixth day, it is shown that water is also produced beside natural gas. However, fraction of produced gas contributed by hydrate dissociation increases over time. It should be not forgotten that the water production limits the gas production by decreasing the gas mass fraction. In case two, they have used a horizontal well 0.25 m below the hydrate layer and the perforated interval had a length of 20m. In case 3 and 4 they have investigated the combination effects of depressurization and thermal stimulation for two vertical wells at Zone#1 of Malik site. In case 3 steam was injected in the hydrate bed with enthalpy ($H = 3200kJkg$) corresponding to $T = 420°C$ (superheated at that pressure). The steam injection rate and the liquid production rate were same and equal to $Q = 1.67 \times 10^{-3}(kgs)$. Case 4, was injection of CH_4 at rate of $Q = 8.35 \times 10^{-4}(kgs)$ and fluids were produced at the rate of $Q = 2.51 \times 10^{-4}(kgs)$.

Zone#2 is characterized by 16-m thick hydrate bearing interval (From -899 to -915m) with $T = 7.5°C$ and $P = 9MPa$ at the base of hydrate interval. The hydrate saturation is $S_H = 0.5$. Zone#3: Extends from a depth of about -1081 to -1091m, with $S_H = 0.8$, $T = 12.8°C$ and $P = 10.74MPa$. It is the deepest and warmest of these three zones. Zone#4 extends from the depth of -1007 to -1017 m and has hydrate saturation (S_H=0.5) and the base of hydrate interval, $T = 10.5°C$ and $P = 10MPa$. Zone #5 ($S_H = 0.5$ and $P = 8.9MPa$) and -905 to -915 m and $T = 7.5°C$.

5.1 Effects of Hydrate Saturation (S_H)

For a constant well temperature, a higher hydrate saturation is expected to be associated with the higher mass production.[77] found that by increasing the hydrate saturation from 0.5 to 0.8 the gas production increases.

5.2 Effects of Initial Formation Temperature and Thermal Conductivity

Their study found that the initial formation temperature has a dramatic effect on the amount of gas production. They have found that increasing the formation temperature (T_H) from 7.5°C to 11°C will increase the gas production by the factor of 4.

5.3 Effects of Boundary Conditions

In addition, they have shown that by increasing the well temperature (T_W) from 50 to 70°C, gas volume production increases by 25%, since the methane production depends on the temperature difference between the well temperature and the hydrate formation. However, as the time goes further, this temperature difference decreases as the formation temperature increases to reach the well temperature. It has been shown that heat addition (Q_w) by the amount of 6kW will increase the production by 40%.

5.4 Effects of Permeability (k), Hydrate Heat Capacity (C_H) and Rock Heat Capacity (C_R)

The study shows that gas production is insensitive to the formation permeability k when k increased from $2 \times 10^{-14} m^2$ to $10^{-13} m^2$.

Chapter 6

Candidate Sites for Model Development

Candidate sites should be found to deploy a power system that uses seafloor methane hydrate on the seafloor and dissolved oxygen in sea water to generate power of the order of 1000W net. For these purposes, candidate sites for this proof-of-concept are evaluated. Site selection is an important step in the verification of the modelling process, since it establishes many of the critical design parameters, such as fuel quality, ambient oxygen levels, operation depth, operating pressures and temperatures, currents, methane solubility, accessibility, etc. Based on a survey of the methane resource, several sites in different areas were identified. The first area is GC185 and GC234 in the northern Gulf of Mexico southeast of Mississippi River Delta., shown in Fig. 6.1. verified [43]. Three different seepages were imaged and analyzed in that area.

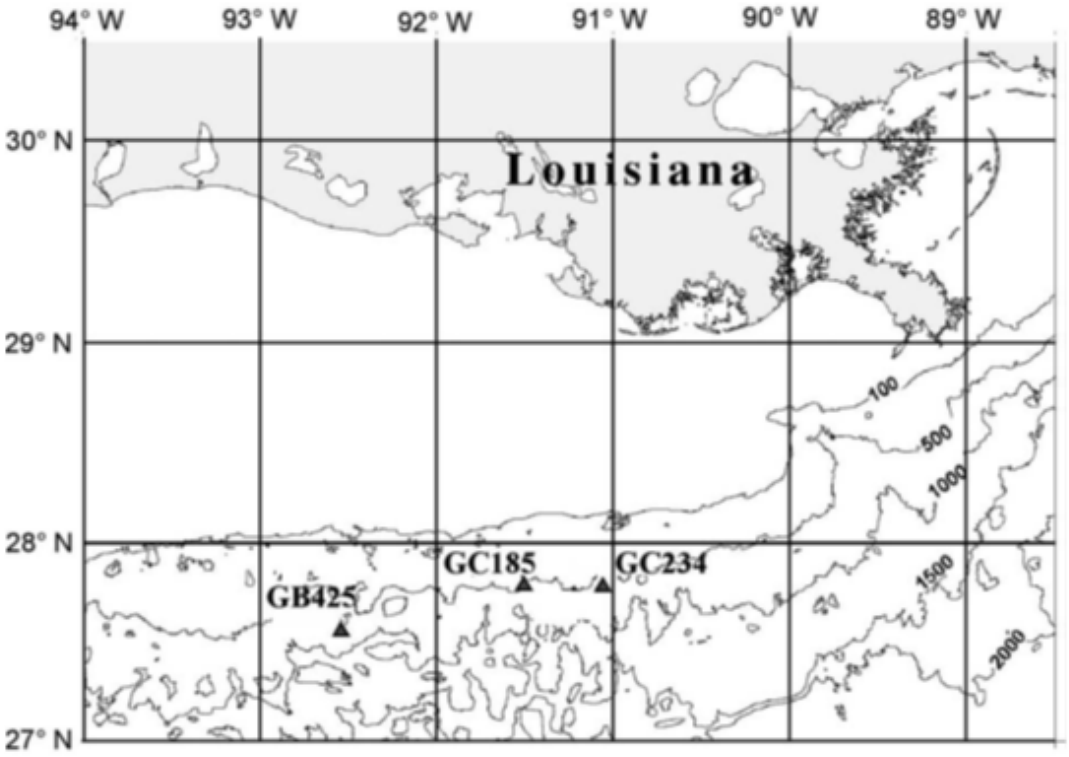

Figure 6.1: GC185 and GC234 in northern Gulf of Mexico southeast of Mississippi River Delta [43]

The total observed gas flux was 62.3×10^{-3}mol/s, mostly methane. 50% of the bubble mass was contained in the largest bubbles, $r > 5500\mu m$.

Louisiana site has three mounds and corresponding gas bubble seeps which is discussed in [43]. Coordinates of these sites are shown in Fig. 6.1. Other site overlying seafloor hydrate mounds in the Gulf of Mexico (GOM) also attract attention. These include the Atwater Valley mounds shown in Fig. 6.2. and surveyed by NETL.

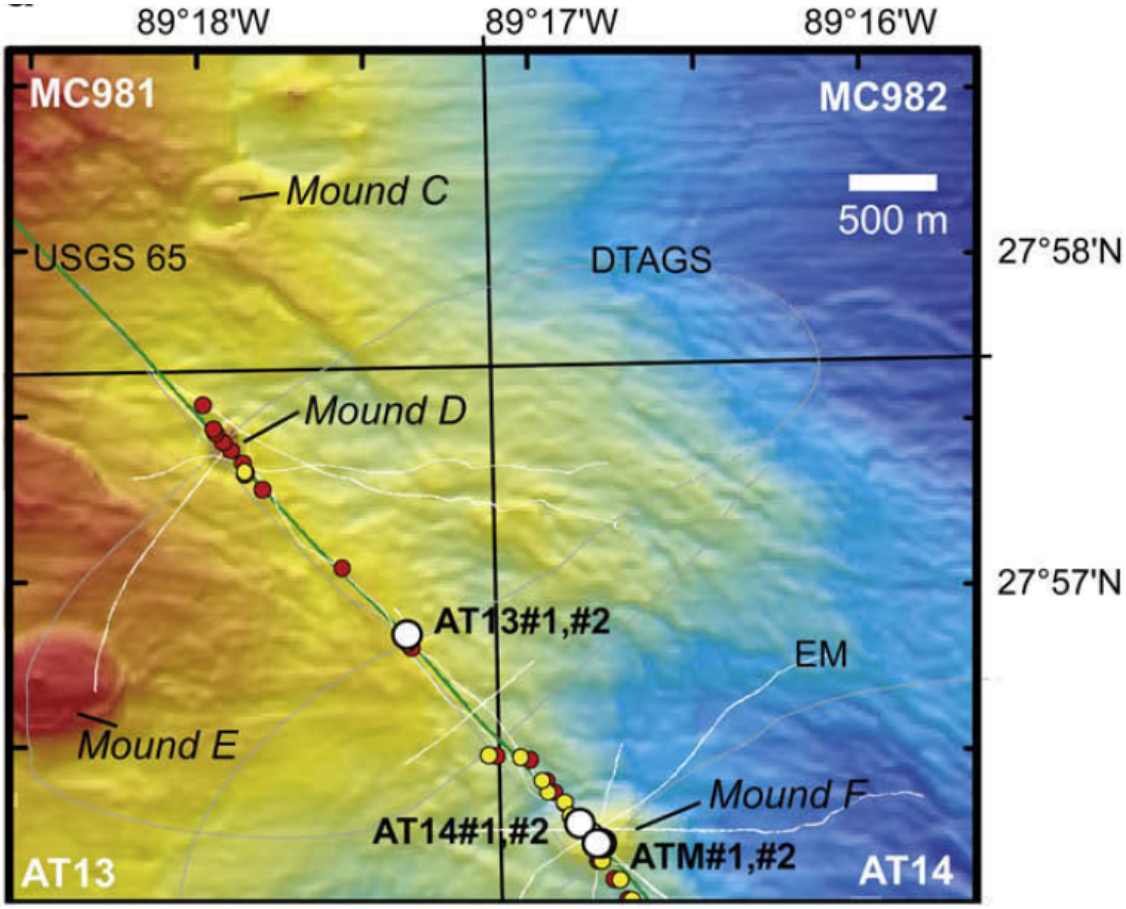

Figure 6.2: Atwater Valley mounds [104]

Chapter 7

Methane Source Investigation

Using current technologies that exist, it is estimated to produce about 1000 W electricity for a long period of time for years. The main question is whether these technologies are feasible in deep ocean sediments to produce enough natural gas regarding volume, concentration and purity required for a fuel reformer (SMR, ATR) or solid oxide fuel cell (SOFC). Also the energy penalties associated with these devices have to be considered.

In depth lower than 500 m, vast quantities of methane hydrate are found worldwide dispersed in the sediments on continental margins. Although most of this hydrate lies beneath the seafloor, surface hydrate mounds have been observed to occur at many locations. Methane gas seeps, usually from thermogenic sources, have been detected over a range of depths. Methane dissolved in sea water or sediment pore water can be found throughout the oceans.

Resource	**Advantages & Disadvantages**
Methane gas vents	1) Huge mass flow of gas 2) No energy required to produce gas 3) Mostly exists in shallow water 4) Not Available at all locations 5) High level of contamination
Hydrates	1) Huge source of Energy , Mostly in deep environment ($> 500m$) 2) Recovery technology limitations 3) Best energy efficient method is not proved
Pore water methane	Available but very low concentrations
Dissolved methane in sea water	Available but very low concentrations

Table 7.1: Advantages and Disadvantages of methane resources in deep ocean

Pore water methane and dissolved methane in sea water are available throughout the oceans with very low concentrations. So, they could not be a very good choice for power plant at one location. However, seafloor vents of free methane gas and methane hydrates have highly concentrated sources of fuel. In the long-term, methane hydrates (depth<500m) and shallow deposits beneath the seafloor will be viable candidates for exploitation, since they are more widely available than vents. Recovery of methane gas from the solid hydrates has technical disadvantage. Recovery has technical deficiencies on system and techniques that are efficient are verified.

7.1 Fuel Contaminants

Solid Oxide Fuel Cells are targeted to be employed at the power generating unit, the raw fuel gas will need to be converted to H_2 via a reforming step (in this case Steam Methane Reforming (SMR)). Catalytic thermochemical reforming (followed by water-shift) is used in the study at a manageable level of risk when adapted to the relatively unique conditions of the present application (e.g., high pressure, limited available oxidizer; No maintenance); So, using Steam Methane Reforming is currently the method of choice. Literature is documented regarding the sensitivity of fuel cell and reformer to various catalyst poisons. It is essential, that contaminant species of consequence in the raw gas (methane dissociated from hydrate sediment) entering the reformer and consequently the fuel cell exist at acceptably low levels so that they do not to degrade performance or lifetime of these components (e.g. SMR, SOFC, Catalytic

combustor, Heat exchangers).

Based on the literature reviews [78], It is found that the limiting concentration of contaminants is 1000 ppmV H_2S for performance of system components without degradation. Data on gases released from the strong vents offshore Coal Oil Point in the Santa Barbara Channel that have been documented verify 1000 ppmV H_2S. In the case of methane gas released from hydrates, several examples have been reported where H_2S was detected more than 1000 ppmV. [79] analyzed hydrates from the Cascadia Margin and determined an average sulfide concentration of 0.27% (i.e., 2700 ppmV). It has been observed that there can be large variations in H_2S over the same general area. [81] reported sulfide concentrations as high as 18.5% (185,000 ppmV) in hydrates from one location on the Cascadia Margin. Pre-deployment investigations should be made in order to specify sites in which power system should be installed.

7.2 Oxygen Resource

Since the start of this project, we have been concerned about the oxygen to down-hole regions adjacent to strong seafloor methane sources. Since the performance of the present system is oxygen-limited, any reduction of dissolved oxygen levels is a considerable problem. This does not focus on methods of oxygen delivery, but on the physics of the high pressure fuel cell and hydrate deposits at deep ocean conditions.

Chapter 8

Current State of SOFC/SOEC Technology

Solid Oxide Fuel Cell (SOFC) technology is an attractive, emerging electric power generation technology. SOFC directly converts fuel to electricity. The direct electrochemical conversion of fuel allows for high fuel-to-electric conversion efficiencies without pollutant emissions. The interest in developing SOFC systems is substantial. VersaPower, FuelCell Energy, Bloom Energy, LG Fuel Cell Systems, Delphi, Ceramic Fuel Cells Limited, and other companies have been developing SOFC technology for a long time (from more than 10 to more than 20 years). Many companies have demonstrated small scale (1-5 kW), and distributed generation scale (100 and 800 kilowatt) integrated SOFC systems that have shown high efficiency and low emissions ([18],[82],[83]). In addition, some companies have demonstrated 200 to 330 kilowatts pressurized SOFC/gas

turbine hybrid systems (e.g., Siemens Power, LG Fuel Cell Systems).

Recently, the robust and high efficiency performance of SOFC technology has sparked an interest in reversible solid oxide fuel cells for use as electrolyzers solid oxide electrolysis cell (SOEC) in energy conversion/storage systems. The reversible SOFC offers dual-mode operation capable of distributed electrical power generation in the fuel cell mode and hydrogen production by steam electrolysis in the reverse mode. The hydrogen and oxygen can be used for other purposes or can be reconverted on-demand to electricity and water through the fuel cell. In the proposed effort, the SOEC will be considered as one of the electrolysis components for use in the integrated electrochemical systems designed for methane dissociation from hydrate fields in the deep ocean. Other electrolysis technologies (e.g., alkaline, proton exchange membrane) will also be considered.

The most common anode materials for fuel oxidation in current SOFC systems are nickel/yttria-stabilized zirconia (Ni/YSZ) cermets, which possess excellent catalytic activity and conductivity. However, the Ni/YSZ anode has some disadvantages, including nickel coarsening, sulfur poisoning and carbon deposition, which can hinder the direct use of practical fuels (e.g., natural gas), and volume instability during redox cycles, which can cause catastrophic cell fracture. Recently perovskite oxides such as donor-doped strontium titanate (SrTiO3) have been considered to be a promising alternative SOFC electrode material [[25] , [84]-[88]]. Several investigators have recently studied the use of traditional SOFC materials sets in reversible SOFC stacks using a YSZ electrolyte with Ni-YSZ anode and a strontium-doped lanthanum manganite

(LSM) cathode. These studies have advanced understanding of reversible SOFC technology and provided useful insights into means of optimizing electrode performance, expected degradation rates in fuel cell and electrolysis modes, and manufacturing process impacts on reversible SOFC performance [92]. In addition, these studies generally confirm the robust performance of the YSZ materials set in the fuel cell mode. However, the reversible SOFC technology advanced to-date has not been proven robust and especially exhibits high rates of degradation in electrolysis mode ([89]-[91]).

The reversible SOFC technology operates at relatively high temperature so that electrolysis of steam consumes less electrical energy compared to electrolysis at lower temperatures due to the more favorable thermodynamic and electrochemical kinetic conditions, and due to the lower polarization losses for the reactions. Reversible SOFC systems are also likely to have advantages over competing electrolysis technologies. The analyses proposed will consider these features as integrated into methane dissociation systems in deep ocean hydrate fields. However, alkaline and proton exchange membrane electrolyzers are more commercially advanced than are SOEC systems. As a result the proposed effort will include conceptualization and detailed analyses of integrated methane dissociation systems that use alkaline and PEM electrolyzers as the base case systems for consideration.

Chapter 9

Model Description

9.1 Power Generation

The objective is to produce electricity for electronic devices such as AUVs (autonomous underwater vehicles) or UUVs (unmanned underwater vehicles), or other instruments and screening devices, specially those with greater electrical requirements than batteries.

9.2 Fuel Production

The objective is to produce and store fuel (e.g., H_2, pure CH_4) and, possibly oxygen. From a thermal systems perspective, this application is a subset of the first application: which is, the fuel cell (SOFC) is transferred from being part of the elec-

trical power generation system to the end-use. The primary functions that need to be performed by the electrical power generation system, like fuel gas purification and reforming to hydrogen are the same as for Fuel Production.

The selection of a fuel cell as the power module defines the other components of the systems which can be divided into three categories: 1) fuel supply, 2) oxidizer supply; 3) ancillary equipment (Heat exchangers). The main function of the reformer is to provide H_2 to the fuel cell with an acceptable level of contaminants at a rate to sustain system net power production of the order of 1000 W. Specific contaminant species concentration that fuel cell system tolerates depend on the type of fuel cell. For instance, the performance of the PEMFC is degraded by CO while the alkaline fuel cell is sensitive to CO_2. However SOFC is chosen in this study because it is tolerant to both CO and CO_2 contaminants, since it operates at high temperatures. The fuel supply has an equipment to collect and clean the raw dissociated methane gas, to convert it to H_2. There is no need for additional steps of fuel cleaning, because of the reasons that were explained above.

Options that could be considered to convert the chemical energy of methane to electrical power are Otto, Brayton, and Rankine cycles (i.e., internal combustion, gas turbine, and vapor power cycles). In the application of extremely low target power and no sustain maintenance make these options feasible. Also, Otto, Brayton, and Rankine cycles require moving components that are subject to wear and failure in the case of no maintenance. Fuel cells have this advantage that, they do not have any moving parts. On the other hand, are well-suited to generate power in the range of interest

(i.e., of the order of 1000 W). However, pumps and fans are required to supply fuel and oxidizer to the anode and cathode, and to circulate liquid electrolytes or remove condensates. Electricity is created directly by the fuel cell. The main drawbacks of fuel cells are their vulnerability to catalyst poisons in the reactant flows and limited validated lifetimes due to degradation.

Ancillary equipment includes heat exchangers and catalytic combustor. The model studies: 1) Identification of viable candidate technologies for the two major components: the fuel reformer and the fuel cell module; 2) Characterization of the performance of these technologies under simulated deep ocean operating conditions; and 3) Integration of these models to perform a first-order systems analysis to estimate net power production. 4) Determination of the net methane production over time.

Conventional fuel cell technology will be applied in the system which requires minimal or no servicing for deeply deployed devices. This provides a significant performance benefit over batteries. The two most vulnerable components are fuel cell module and reformer catalysts because of the poisoning. Operating histories of conventional fuel cells have been reported extensively in the literature. The range of reported lifetimes are: PEMFC about 3,000 hours; Alkaline FC about 5,000 hours; SOFC $>$ 10,000 hours. SOFC has this advantage over other types of fuel cell that has longer lifetime because of being less vulnerable to poisoning. These values generally correspond to well-maintained units operating with conventional design limits.

Fig. 9.1. shows a schematic of the model operation in which Solid Oxide Fuel Cell (SOFC) is used as a thermal heat source to provide heat to the hydrate sediment. Due

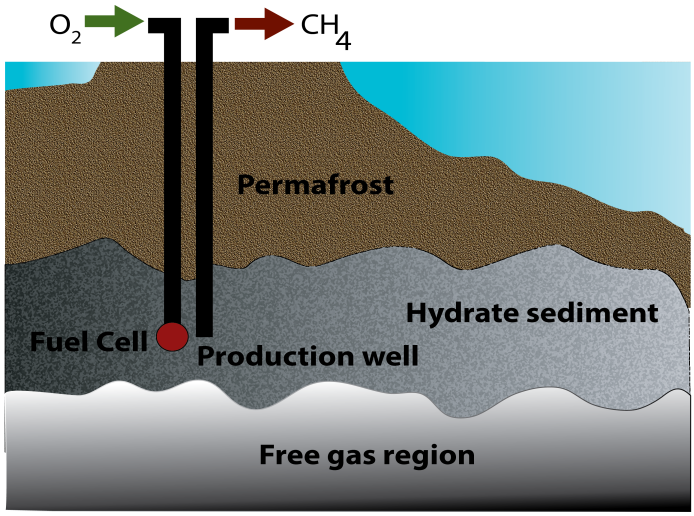

Figure 9.1: Utilization of fuel cell in deep ocean and its relative location to hydrate sediments

to this constant heat flux, natural gas hydrate will dissociate. In this study, a one dimensional model of hydrate bed dissociation is investigated. Two major methods of thermal stimulation and depressurization are studied and compared. Steam methane reformer (SMR) is used as a reformer, to convert methane into hydrogen for the Solid Oxide Fuel Cell. System operation for different parameters of the fuel cell at high pressure is studied. Steam Methane Reformer (SMR) is used as a reformer, to convert methane into hydrogen for the SOFC system. System operation for different parameters of fuel cell (e.g., utilization) at high pressure is studied.

The project studies an extensive literature review regarding electrochemical components and systems, requirements for deep ocean operation, component and balance of plant performance characteristics expected, etc. From the literature review and analyses of the data and observations, the study evaluates electrochemical devices and balance of plant components based upon the measured and/or expected performance

characteristics for use in integrated systems for methane hydrate dissociation. Electrochemical components being evaluated for the methane hydrates dissociation systems are including but not limited to: Solid oxide fuel cells, Solid oxide electrolyzer and various types of fuel reformer. The screening will involve selection of only those technologies that are reasonably proven capable of operation in integrated systems and operation at conditions expected in deep ocean environments. System component candidates will be evaluated under the unique operating conditions associated with in-situ methane hydrate dissociation.

9.3 Cycle Conceptualization

This study conceptualizes integrated system cycles comprised of the selected electrochemical devices and all of the balance of plant equipment required to operate in the deep ocean environment of a methane hydrate field. Each cycle will attempt to exploit the unique features efficient electricity production from released gases, and both heat and CO_2 production for methane hydrate gas dissociation that may be useful in methane dissociation in hydrate fields. Each of the cycle concepts developed are schematically drawn and will be thoroughly described for clarity of integrated system design reasoning as well as individual component performance expected and interactions amongst system components. Each of the cycles is sufficiently rendered to enable detailed thermodynamic and dynamic system analyses, including resolution of all relevant physical, chemical and electrochemical performance characteristics and all losses

in the major system components and balance of plant. In our studies, some integrated systems are designed and analyzed, and the schematics of the integrated systems are shown in Fig. 9.2 to Fig. 9.4. One approach for in-situ methane hydrate dissociation is shown schematically (not all cycle details are shown) in Fig. 9.2. Such an integrated system utilizes a direct electrochemical solid oxide fuel cells to provide heat and CO_2 to the hydrate reservoir (the electrolyzer can also provide heat). Methane is directly converted to electricity and heat in the SOFC without using a fuel reformer/processor. Currently, there are many solid oxide fuel cells operating on direct conversion of methane to products. This system requires high temperature operation around $700 - 800°C$ for the fuel cell. In the current SOFC study, the temperature of the inlet gases is set to $700°C$. A portion of the extracted methane from the hydrate sediments will be used to provide the SOFC fuel or the steam methane reformer. while oxidant is supplied from an electrolyzer. According to analyses and considering the amount of heat required for hydrate dissociation (e.g., 10% of the methane heating value), the amount of produced methane is four times greater than the amount of consumed methane in the fuel cell for this system configuration without considering the possible enhanced recovery that the CO_2/CH_4 exchange process may provide.

Current analyses demonstrate that the major portion of the dissociated methane could be delivered to a land-based power plant. Efficient high pressure electrolysis will eliminate the use of electric wires from the land-based power plants. Despite the fact the high pressure electrolysis (e.g., 100 ATM) will require 12% more power than land-based electrolysis, preliminary analysis shows that an efficient electrolyzer could

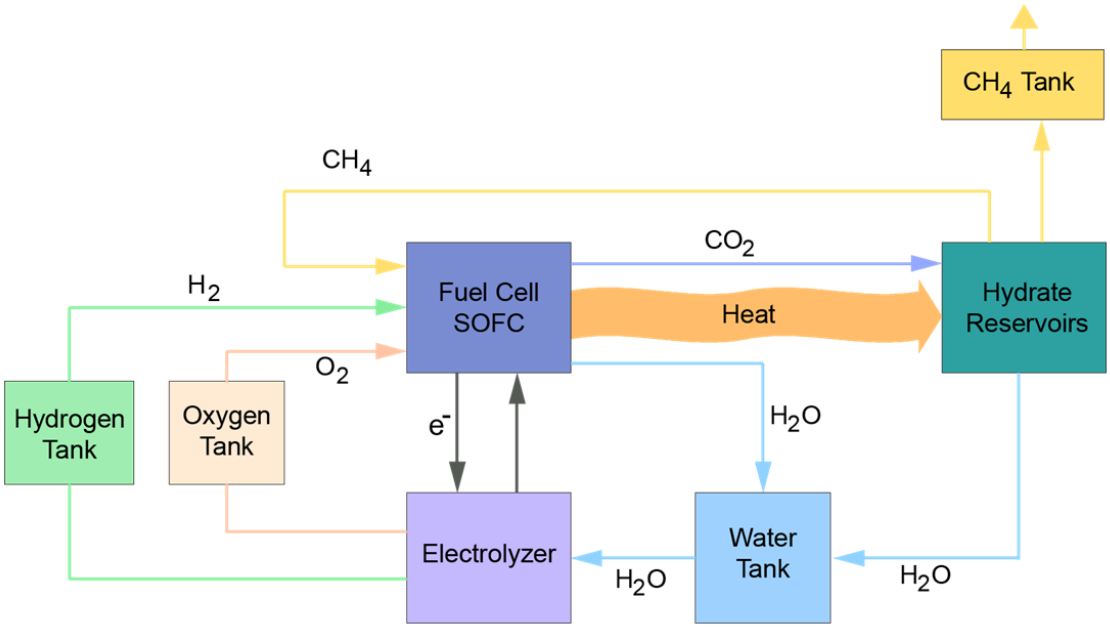

Figure 9.2: Direct electrochemical SOFC integrated with the hydrate sediments.

produce the required oxygen for the fuel cell system. These performance characteristics of the electrolyzer will be thoroughly evaluated in the proposed effort and verified. In addition, the electrolyzer produces additional hydrogen, which could be used directly in the fuel cell system or could be mixed into the methane to produce a synthetic natural gas.

Another example system configuration is shown schematically in the Figure indicating the integrated use of a fuel cell with a fuel reforming/processing system. The various types of internal and external fuel reforming systems (e.g., steam methane reforming SMR, autothermal reforming ATR) should be investigated for use in deep ocean environments. The current study, uses SMR as the reformer for the SOFC. In the fuel reforming system, a portion of the dissociated methane will be converted to the

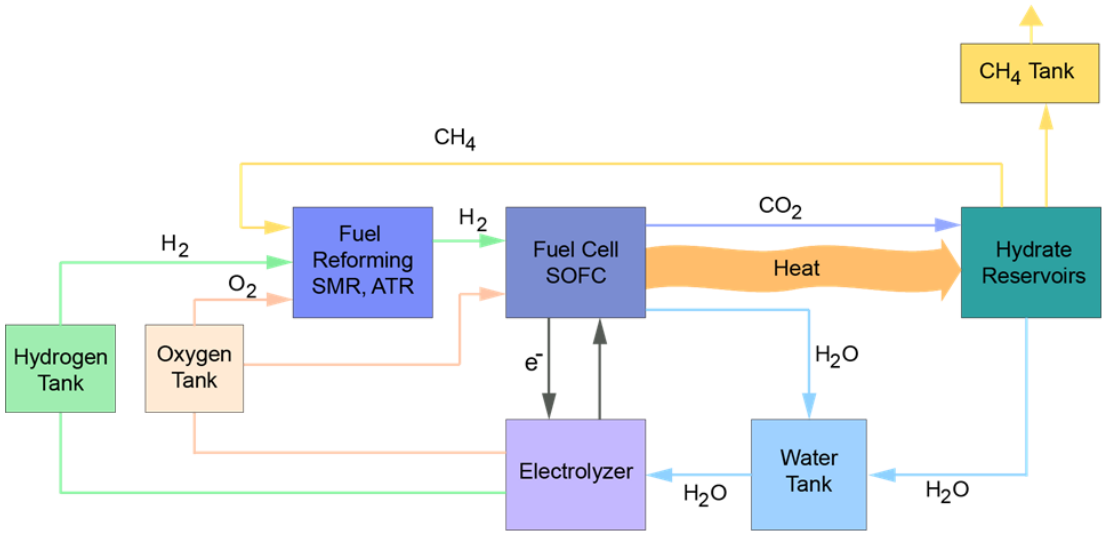

Figure 9.3: Fuel reformer and fuel cell/electrolyzer integrated with the hydrate sediment.

hydrogen and CO_2 through water gas shift reaction. The exit CO_2 has the potential to make CO_2 hydrate in the sediment field. Simulations could be conducted through the available CO_2 injection data in the Ignik Sikumi #1. Based on some preliminary thermodynamic analyses, pure oxygen delivery to the downhole has a much higher energy efficiency than sending air to the deep ocean hydrate sediments. However, according to some new studies nitrogen could replace the CH_4 in smaller cages and produce further methane ([22],[23]). This process will be verified through simulation of air delivery to the high pressure fuel cells.

Fuel cells have the potential advantage to be integrated with an electrolyzer and produce the required oxygen in-situ. In the case that the electrolyzer could not produce a sufficient amount of the oxygen, other approaches could be investigated. One of these approaches is delivery of liquefied oxygen to the downhole, as shown schematically in Fig. 9.4. The energy required for the oxygen liquefaction is 50 KJ/mol. Preliminary

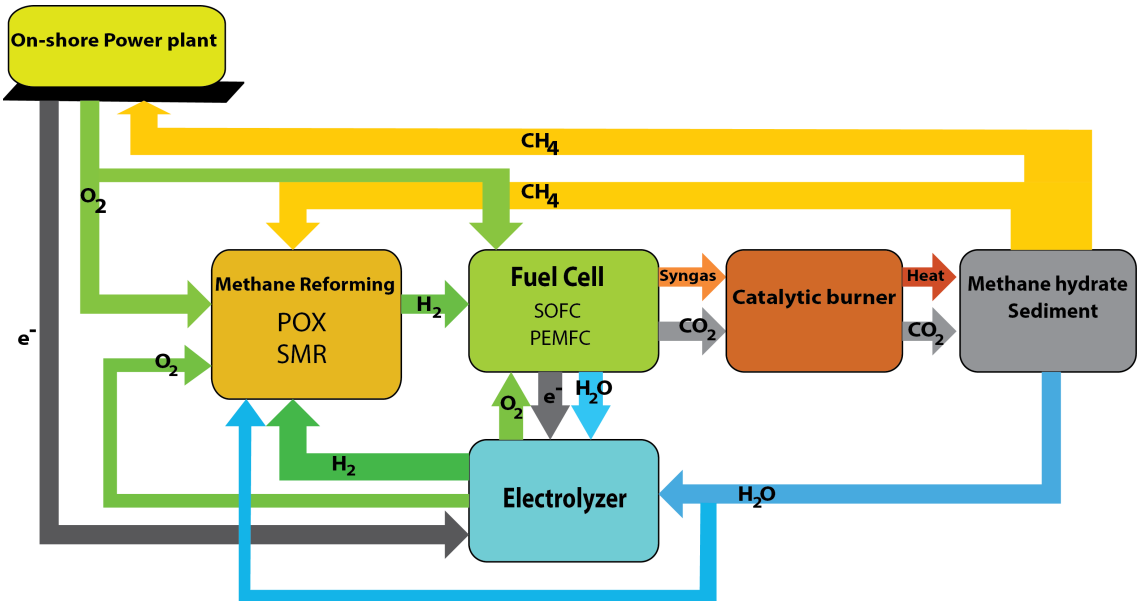

Figure 9.4: Detailed components of the system of study

analyses show that a portion of the delivered methane to the onshore power plant could be used to liquefy oxygen and send it to the downhole.

This would be the first time that electrochemical devices for hydrate dissociation are investigated analytically. The main objective of this study is to select the most efficient method for hydrate dissociation under controlled conditions. The other main objective of this study is to measure the potential natural gas production over a specified period of time. The formation and dissociation are described by:

$$X(CH_4 + N_m.H_2O) \rightarrow X.CH_4 + X.N_m.H_2O$$

where, X is the mole number of hydrate and N_m is the hydration number. This study involves combination of possible dissociation mechanism including, depressurization, and thermal stimulation.

9.4 Equation of Change for Non-Isothermal Systems

The equation of change for energy is obtained by [93] through applying the law of conservation of energy to a small element of volume $\Delta x, \Delta y, \Delta z$ and then allowing the dimensions of the volume element to become vanishingly small. Both kinetic energy and internal energy may be entering and leaving the system by convective transport. Heat may enter and leave the system by heat conduction as well.

(Rate of increase of kinetic and internal energy)=

Net rate of kinetic and internal energy addition by convective transport +

Net rate of heat addition by molecular transport (Conduction) +

Rate of work done on system by molecular mechanisms +

Rate of work done on the system by external forces

The rate of increase of kinetic and internal energy within the volume element $\Delta x \Delta y \Delta z$ is:

$$\Delta x \Delta y \Delta z \frac{\partial}{\partial t}(\frac{1}{2}\rho v^2 + \rho \hat{u}) \tag{9.1}$$

Where, $\hat{u}$, is the internal energy per unit mass (Specific internal energy). $\rho\hat{u}$, is the internal energy per unit volume . $\frac{1}{2}\rho v^2$, is the kinetic energy per unit volume

The amount of the energy that enters the volume is:

$$\Delta y \Delta z(E_x - E_{x+\Delta x}) + \Delta x \Delta z(E_y - E_{y+\Delta y}) + \Delta x \Delta y(E_z - E_{z+\Delta z}) \tag{9.2}$$

E contains the convective transport of kinetic and internal energy, the heat conduction, and molecular work. The rate of doing work on the fluid by external forces is expressed as:

$$\rho \Delta x \Delta y \Delta z(v_x g_x + v_y g_y + v_z g_z) \tag{9.3}$$

So the energy of equation will become:

$$\frac{\partial}{\partial t}(\frac{1}{2}\rho v^2 + \rho \hat{u}) = -(\bigtriangledown.(\frac{1}{2}\rho v^2 + \rho \hat{u})\vec{v}) - (\bigtriangledown.\vec{q}) - (\bigtriangledown.p\vec{v}) - (\bigtriangledown.(\tau.\vec{v})) + \rho(\vec{v}.\vec{g}) \tag{9.4}$$

The most useful form of the energy equation is one in which the temperature appears. So the energy equation can be written in the form:

$$\frac{\partial}{\partial t}(\rho \hat{u}^2) = -(\bigtriangledown.(\rho \hat{u})\vec{v}) - (\bigtriangledown.\vec{q}) - p(\bigtriangledown.\vec{v}) - (\tau : \bigtriangledown \vec{v}) \tag{9.5}$$

With no further assumptions the equation can also be written in the form:

$$\rho \frac{D\hat{U}}{Dt} = -(\bigtriangledown.\vec{q}) - p(\bigtriangledown.\vec{v}) - (\tau : \bigtriangledown \vec{v}) \tag{9.6}$$

If we switch to the enthalpy form:

$$\rho\frac{D\hat{H}}{Dt} = -(\bigtriangledown.\vec{q}) - (\tau : \bigtriangledown\vec{v}) + \frac{DP}{Dt} \tag{9.7}$$

Writing the energy equation in enthalpy form gives us:

$$\rho\frac{DH}{Dt} = -(\nabla.\vec{q}) - (\tau : \nabla\vec{v}) - (\frac{\partial \ln P}{\partial \ln T})_p\frac{DP}{Dt} \tag{9.8}$$

This is the equation of change for temperature, in terms of heat flux vector q and the viscous momentum flux τ.

This is the equation of change for temperature, in terms of heat flux $\vec{q}$ and the viscous momentum flux τ.

9.5 One Dimensional Model

Fig. 9.5 shows the model developed by [65], in which, gas and water are produced at a moving boundary (dissociation front). The porous medium is initially at a uniform temperature T_i which occupies the semi-infinite region, $0 < x < \infty$. At time $t = 0$, the temperature at the boundary $x = 0$ rises to the fuel cell exit gases temperature, since the formation and fuel cell exit gases are in thermal equilibrium. The temperature at $x = 0$ will be kept constant during the dissociation, since the fuel cell operates steadily. Temperature of fuel cell exit gases is at a higher temperature than the hydrate dissociation temperature (T_D) and the hydrate initial temperature (T_i), thus, the moving

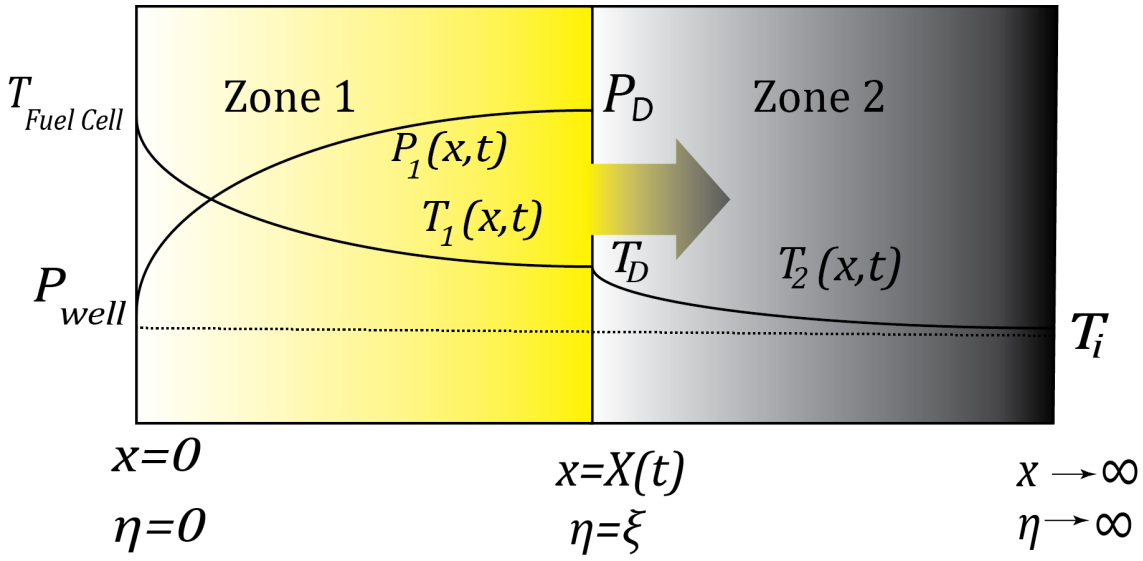

Figure 9.5: One dimensional model of hydrate dissociation due to temperature rise ore pressure drop

boundary (dissociation front) starts moving at time $t = 0$. Therefore, at any time t the hydrate formation is separated into two distinct zones. Zone I: Contains dissociated water and methane gas. Zone II: Contains undissociated hydrate formation.

Thus, in mathematical terms, at any specific time t, in the 1-D physical model, the Zone I fills the $0 < x < X(t)$ and the Zone II fills $X(t) < x < \infty$. Where, $X(t)$ is the moving boundary position. The assumptions associated with this model are:

1) Water that is dissociated from the hydrate formation is stationary

2) Thermophysical properties of each phase are uniform and in equilibrium

3) Viscous dissipation and Inertial forces are negligible

4) External energy transmission is neglected

5) Undissociated zone is completely saturated with hydrate

6) The dissociation front is at equilibrium and dissociation occurs immediately

Figure 9.6: One dimensional model of hydrate dissociation due to temperature rise or pressure drop

7) The gas phase is in thermal equilibrium with sediment temperature

The purpose of this work is to use the semi analytical model developed for permafrost, by [65] for hydrate dissociation under chemical equilibrium stimulated by the SOFC generated heat.

9.6 Thermal Stimulation Mathematical Model Formulation

In this section the one dimensional model of hydrate dissociation under thermal stimulation in porous media developed by [65] is summarized. Continuity equation throughout the dissociated zone (water and gas zone) is in form of Eq. (9.9).

$$\epsilon \frac{\partial \rho_g}{\partial t} + \frac{\partial (\rho_g v_x)}{\partial x} = 0, \quad 0 < x < X(t) \tag{9.9}$$

Where, ϵ is the porosity of the hydrate reservoir. ρ_g is methane gas density. v_x is the gas velocity in Zone I. Momentum equation in gas phase and Darcy law for the dissociated gas in Zone I are in form of:

$$v_x = -\frac{\zeta}{\mu}\frac{\partial P}{\partial x} \quad , 0 < x < X(t) \quad , t > 0$$

(9.10)

Where, P is pressure in Zone I. μ is gas viscosity and ζ is sediment permeability. Energy balance in Zone I is in form of :

$$\rho_I C_{p,I}\frac{\partial T_I}{\partial t} + \frac{\partial(\rho_g C_{p_g} v_x T_I)}{\partial x} = k_I \frac{\partial^2 T_I}{\partial x^2} \qquad 0 < x < X(t), \quad t > 0$$

(9.11)

Where, T_I is temperature in Zone I. k_I is thermal conductivity of Zone I. $C_{p,g}$ is methane gas heat capacity. Energy balance in the undissociated zone (Zone II) is in form of:

$$\frac{\partial T_{II}}{\partial t} = \alpha_{II}\frac{\partial^2 T_{II}}{\partial x^2} \quad X(t) < x, \quad t > 0$$

(9.12)

Where, T_{II} is the temperature profile in the undissociated zone. α_{II} is the thermal diffusivity of Zone II. Boundary conditions for the initial value problem is in form of Eq. (9.13) to (9.15):

$$T = T_{HX} \quad x = 0, \quad t > 0$$

(9.13)

$$P = P_w \quad x = 0, \quad t > 0$$

(9.14)

Where, T_{HX} is the heat exchanger exit temperature. P_w is the production well pressure. Because of the continuity, temperatures of the two zones are equal at the dissociation front, thus:

$$T_I = T_{II} = T_D \quad x = X(t), \quad t > 0 \tag{9.15}$$

Mass balance at the moving boundary position is in form of:

$$\Omega \epsilon \rho_{Hydrate} \frac{dX}{dt} + \rho_g v_x = 0 \quad x = X(t), \quad t > 0 \tag{9.16}$$

Where, Ω is the mass of methane gas per unit mass of hydrate formation, the number is found in the literature to be 0.1265 kg methane per kg hydrate [65]. Energy balance at the dissociation front is in form of:

$$k_I \frac{\partial T_I}{\partial x} - k_{II} \frac{\partial T_{II}}{\partial x} = -\epsilon \rho_{Hydrate} \Delta H_D \frac{\partial X}{\partial t} \quad x = X(t), \quad t > 0 \tag{9.17}$$

Where, k_1 and k_2 are the thermal conductivities of the Zone I and Zone II. ΔH_D is the methane hydrate heat of dissociation which has a relation with temperature. The thermodynamic equilibrium relation between the hydrate dissociation temperature, T_D, and pressure P_D at the dissociation interface is expressed as:

$$P_D = exp(A_D - \frac{B_D}{T_D}) \quad x = X(t), \quad t > 0 \tag{9.18}$$

Boundary conditions for undissociated zone are shown in Eq. (9.19) to Eq. (9.21):

$$T_{II} = T_i \quad x \to \infty \quad t > 0 \tag{9.19}$$

$$T_{II} = T_i \quad 0 < x < \infty, \quad t = 0 \tag{9.20}$$

$$X(t) = 0 \quad t = 0 \tag{9.21}$$

Under above assumptions, the similarity solution to the system of equations is found to be:

$$\frac{T_I - T_0}{T_D - T_0} = \frac{erf(C_1\Pi + C_2) - erfC_2}{erf(C_1\Xi + C_2) - erfC_2} \tag{9.22}$$

$$\frac{T_{II} - T_i}{T_D - T_i} = \frac{erfc(\Pi)}{erfc(\Xi)} \tag{9.23}$$

The constant parameter, Ξ is the root of the Eq. (9.24):

$$C_1 \frac{k_I(T_0 - T_D)}{k_{II}(T_D - T_i)} \frac{exp[-(C_1\Xi + C_2)^2]}{erf(C_1\Xi + C_2) - erf(b)} - \frac{exp(-\Xi^2)}{erfc(\Xi)} = \sqrt{\pi}\epsilon \frac{\rho_{hydrate}}{\rho_{II}} St\Xi \tag{9.24}$$

Where, Π parameter (non_dimensionalized distance) can be found from Eq. (9.25):

$$x = \Pi\sqrt{4\alpha_{II}t} \tag{9.25}$$

Dissociation front location, is:

$$X(t) = \Xi\sqrt{4\alpha_{II}t} \tag{9.26}$$

Parameters, C_1 and C_2 can be found in Eq. (9.27) and Eq. (9.28):

$$C_1 = (\frac{\alpha_{II}}{\alpha_I})^{\frac{1}{2}} \tag{9.27}$$

$$C_2 = C_{p,g}\frac{\omega\epsilon\rho_{hydrate}\alpha_{II}}{C_1 k_1}\Xi \tag{9.28}$$

The Stefan number (ST) is derived to be:

$$St = \frac{\Delta H}{C_{p_{II}}(T_D - T_i)} \tag{9.29}$$

It should be noted that, the temperature of dissociation T_D and pressure of dissociation P_D are independent of time, so we can conclude that they are constant during the dissociation process. The properties of methane hydrate reservoir that is used is shown in Table 9.1.

Parameter	Value Used
Porosity,ϵ	0.3
Permeability,κ	$1.38 \times 10^{-13} m^2$
Thermal diffusivity of the dissociated zone,α_I	$2.89 \times 10^{-6} \frac{m^2}{s}$
Thermal diffusivity of hydrate zone,α_{II}	$6.97 \times 10^{-7} \frac{m^2}{s}$
Thermal conductivity of the dissociated zone, k_1	$5.57 \frac{W}{m.K}$
Thermal conductivity of the undissociated zone, k_2	$2.73 \frac{W}{m.K}$
Hydrate density, ρ_H	$913 \frac{kg}{m^3}$
Hydrate heat of dissociation,$\Delta H_D(\frac{J}{kg})$	
$248 < T < 273$	$215.59 \times 10^3 - 394.945T$
$273 < T < 298$	$446.12 \times 10^3 - 3132.638T$
Thermal equilibrium equation of hydrate (Phase diagram)	$P_D = \exp(49.3185 - \frac{9459}{T_D})Pa$
Gas heat capacity $\frac{J}{kg.K}$	$C_{pg} = 1.23879 \times 10^3 + 3.1303T + 7.905 \times 10^{-4}T^2 - 6.858 \times 10^{-7}T^3$
Gas viscosity $(Pa.s)$	$\mu = [2.4504 \times 10^{-3} + 2.8764 \times 10^{-5}T + 3.279 \times 10^{-9}T^2 - 3.7838 \times 10^{-12}T^3] + [2.0891 \times 10^{-5}\rho_g + 2.5127 \times 10^{-7}{\rho_g}^2 - 5.822 \times 10^{-10}{\rho_g}^3 + 1.8387 \times 10^{-13}{\rho_g}^4]$

Table 9.1: Methane hydrate properties used in one dimensional thermal stimulation modeling [65]

9.7 Depressurization Modeling

In this section the mathematical formulation and classical Stefans problem for hydrate decomposition suggested by [2] are summarized. Distribution of pressure in the layer is described by Stefan's one dimensional melting problem in Eq. (9.30):

$$\frac{2\epsilon_n \mu}{k_n}\frac{\partial P_n}{\partial t} = \frac{\partial {P_n}^2}{\partial x^2} \tag{9.30}$$

Where,

$$\epsilon_1 = (1-\tau)\epsilon \tag{9.31}$$

$$\epsilon_2 = (1-\beta)\epsilon \tag{9.32}$$

ϵ is porosity of the one dimensional hydrate layer. ϵ_1 and ϵ_2 are the amount of free gas and hydrate layer. μ is viscosity of gas in zones 1 or 2. k_1 ans k_2 are phase permeability of gas in zone 1 or 2. P_1 and P_2 are pressures in zones 1 and 2 respectively. τ is water content of the porous media. β is methane hydrate saturation in one dimensional hydrate layer.

Index n=1 is associated with the region $0 < x < X(t)$, and the index n=2 is associated to the region $X(t) < x < \infty$. $X(t)$ is the position of dissociation front which

separates zones 1 and 2. The boundary conditions are described in Eq. (9.33) to Eq. (9.37):

$$P_1(0,t) = P_w \tag{9.33}$$

$$P_2(x,0) = P(\infty,t) = P_i \tag{9.34}$$

$$P_1(X(t),t) = P_2(X(t),t) = P_D(T_D) \tag{9.35}$$

$$T_2(\infty,t) = T(x,0) = T_i \tag{9.36}$$

$$T_1(X(t),t) = T_2(X(t),t) \tag{9.37}$$

Where, P_w is well pressure at position $x = 0$. P_i and T_i are initial pressure and temperature of the hydrate layer at $t = 0$. P_D and T_D are the pressure and temperature at the dissociation front respectively. T_1 and T_2 are the temperatures in zone 1 and 2 respectively. $P_D(T_D)$, expresses the equilibrium relation between the pressure and the temperature of hydrate decomposition T_D at dissociation front. This relation is derived from thermodynamic equilibrium between methane gas and methane hydrate and is described in form of equation:

$$\log P_D = a(T_D - T_0) + b(T_D - T_0)^2 + c$$

(9.38)

a,b,c are the experimental constants depending on hydrate structure and pressure and temperature variation. a , b and c are found to be [94]:

$$a = 0.0342\frac{1}{K}, b = 0.0005\frac{1}{K^2}, c = 6.4804$$

(9.39)

P_D is in Pa. At the surface $X(t)$ the conditions of gas and water mass balance should be considered. The term mass fraction of gas in a hydrate is introduced by [95].

$$\theta = \frac{M_{gas}}{G.M_{water} + M_{gas}}$$

(9.40)

M_{gas} and M_{water} are the molecular weight of methane and water. G is the number of water molecules per one molecule of gas in a hydrate structure. Mass balance for gas at dissociation front location $X(t)$ is derived from the work of [96]:

$$\rho_1 v_1 - \rho_2 v_2 = -[\beta\theta\rho_3(1-\tau)\rho_1 + (1-\beta)\rho_2]\epsilon\frac{dX(t)}{dt}$$

(9.41)

Where, ρ_1 and ρ_2 are the densities of methane gas in dissociated and undissociated zones. v_1 and v_2 are velocities of methane gas in dissociated and undissociated zones. Using equation of state for gas and continuity at $X(t)$:

$$\rho_1(X(t),t) = \rho_2(X(t),t) = \rho_0 \frac{P_D T_0}{Z P_0 T_D} \tag{9.42}$$

Where, Z is the compressibility of gas. ρ_0 is the density of gas at atmospheric pressure P_0 and temperature T_0. Hence, the equation of gas balance at the decomposition front is as follows:

$$v_1(X(t),t) - v_2(X(t),t) = -[\theta\beta \frac{\rho_3 P_0 T_D}{\rho_0 P_D T_0} z - (\beta - \tau)]\epsilon \frac{dX(t)}{dt} \tag{9.43}$$

Eq. (9.44) describes the balance of water released from hydrate sediment during dissociation.

$$\rho_W \epsilon \tau = (1-\theta)\rho_3 \epsilon \beta \tag{9.44}$$

It is assumed water is stationary, and the pressure and temperature are low enough in a gas hydrate layer. Thus, we can assume ρ_W and τ_W is also a constant. Temperature field of a gas-saturated layer could be expressed by Eq. (9.45):

$$a_n \frac{\partial^2 T_n}{\partial x^2} = \frac{\partial T_n}{\partial t} - \frac{c_v k_n}{c_n \mu} \frac{\partial P_n}{\partial x} (\frac{\partial T_n}{\partial x} - \delta \frac{\partial P_n}{\partial x}) - \eta \frac{\epsilon_n c_v}{c_n} \frac{\partial P_n}{\partial t} \tag{9.45}$$

Where, a_n, c_n is the thermal conductivity and heat capacity of the zones. c_v is the volumetric heat capacity of methane gas. δ, η is the throttling and adiabatic coefficients

of gas. Using Linearization [94]:

$$\frac{\partial {P_1}^2}{\partial t} \approx 2P_w \frac{\partial P_1}{\partial t}, \ \frac{\partial {P_2}^2}{\partial t^2} \approx 2P_i \frac{\partial P_2}{\partial t} \tag{9.46}$$

Eq. (9.45) can be approximated without substantial error.

$$\frac{\partial {P_n}^2}{\partial t^2} \approx \Lambda_n \frac{\partial^2 P_n}{\partial x^2} \ \ n = 1, 2 \tag{9.47}$$

$$\Lambda_1 = \frac{k_1 P_g}{\epsilon(1-\tau)\mu}, \Lambda_2 = \frac{k_2 P_i}{\epsilon(1-\beta)\mu} \tag{9.48}$$

Self-similar solutions of linearized equation with the boundary conditions in Eq. (9.33) to Eq. (9.37) is written in form of:

$${P_1}^2 = {P_w}^2 - ({P_w}^2 - {P_D}^2)\frac{erf\xi_1}{erf\kappa_1} \tag{9.49}$$

$${P_2}^2 = {P_i}^2 - ({P_i}^2 - {P_D}^2)\frac{erf\xi_2}{erf\kappa_2} \tag{9.50}$$

Where,

$$\xi_n = \frac{x}{2\sqrt{\Lambda_n t}}, \kappa_n = \sqrt{\frac{\sigma}{4\Lambda_n}} \tag{9.51}$$

$$erf\xi = \frac{2}{\sqrt{\pi}\int_0^{\xi} e^{-\eta^2}\, d\eta} \tag{9.52}$$

$$X(t) = \sqrt{\sigma t} \tag{9.53}$$

Assuming the conductive heat transfer is much smaller than convective heat transfer, Eq. (9.45) can be written in the form of:

$$\frac{\partial T_n}{\partial t} - \frac{c_v k_n}{c_n \mu}\frac{\partial P_n}{\partial x}\left(\frac{\partial T_n}{\partial x} - \delta\frac{\partial P_n}{\partial x}\right) - \eta\frac{\epsilon_n c_v}{c_n}\frac{\partial P_n}{\partial t} = 0 \tag{9.54}$$

Solutions of equations is derived as:

$$T_1 = T_D + A_1\delta[erf\,\xi_1 - erf\kappa_1 - (\frac{\eta}{\delta}B_1 - 1)(\Phi_1(\kappa_1) - \Phi_1(\xi_1)) \tag{9.55}$$

$$T_2 = T_i + A_2\delta[erfc\,\xi_2 - \Phi_2(\xi_2) - \frac{\eta}{\delta}B_2\Phi_2(\xi_2)] \tag{9.56}$$

Where,

$$\Phi_1(\tau_0) = \frac{2}{\sqrt{\pi}}\int_0^{\tau_0} \frac{\nu e^{-\nu^2}}{\nu + C_1 e^{-\nu^2}}\, d\nu \tag{9.57}$$

$$\Phi_2(\tau_0) = \frac{2}{\sqrt{\pi}}\int_{\tau_0}^{\infty} \frac{\nu e^{-\nu^2}}{\nu + C_2 e^{-\nu^2}}\, d\nu \tag{9.58}$$

$$A_1 = \frac{2}{erf\xi_1}\frac{{P_D}^2 - {P_w}^2}{P_w} \tag{9.59}$$

$$A_2 = \frac{2}{erfc\xi_2}\frac{{P_i}^2 - {P_D}^2}{P_i} \tag{9.60}$$

$$B_1 = \frac{{P_w}^2\epsilon_1 c_{0,v}}{4P_0 c_1}, B_2 = \frac{{P_i}^2\epsilon_2 c_{0,v}}{4P_0 c_2} \tag{9.61}$$

$$C_1 = \frac{{P_D}^2 - {P_w}^2}{P_w}\frac{c_v}{c_1}\frac{1}{2\sqrt{\pi}erf\xi_1}\frac{k_1}{\mu\Lambda_1} \tag{9.62}$$

$$C_2 = \frac{{P_i}^2 - {P_D}^2}{P_i}\frac{c_v}{c_2}\frac{1}{2\sqrt{\pi}erf\xi_2}\frac{k_2}{\mu\Lambda_2} \tag{9.63}$$

P_D, T_D and σ, which detremines the rate of front movement, are determined as follows:

$$T_D = T_i - A_2\delta[erfc\,\kappa_2 - \Phi_2(\kappa_2) - \frac{\eta}{\delta}B_2\Phi_2(\kappa_2)] \tag{9.64}$$

The pressure at the dissociation front is found from Eq. (9.38), Substituting Eq. (9.49) and (9.45) into Eq. (9.43), we can reach the equation to determine σ:

$$k_1\frac{{P_D}^2 - {P_w}^2}{\sqrt{\pi\Lambda_1}}\frac{e^{-{\kappa_1}^2}}{erf\kappa_1} - k_2\frac{{P_i}^2 - {P_D}^2}{\sqrt{\pi\Lambda_2}}\frac{e^{-{\kappa_2}^2}}{erf\kappa_2} = A\sqrt{\sigma} \tag{9.65}$$

Where,

$$A = [\theta\beta\frac{\rho_3 P_0 T_D}{\rho_0 T_0} z - (\beta - \tau)P_D]\epsilon\mu \tag{9.66}$$

It should be noted that the temperature and pressure at the dissociation front are fixed values and dependent on well pressure P_w. The production rate of gas per unit length of well can be derived in form of equation:

$$Q = -\frac{k_1}{\mu}\frac{\partial P(0,t)}{\partial x} = \frac{k_1}{\mu}\frac{({P_D}^2 - {P_w}^2)}{P_w}\frac{1}{erf\kappa_1}\frac{1}{2\sqrt{\pi\Lambda_1 t}} \tag{9.67}$$

The production rate of gas decreases inversely with time. Eq. (9.64) and Eq. (9.65) can be used to determine all the characteristics of the process of gas hydrates dissociation during depressurization.

9.8 Solubility

Thermodynamic potential equations are developed by ([40],[41]). Methane solubility in sea water is specified by balancing the chemical potential of vapor methane and liquid methane at the specific temperature and pressure. In terms of fugacity in vapor

phase and activity in liquid phase, we have:

$$\mu^{v}{}_{CH_4}(T,P,x) = \mu^{v(0)}_{CH_4}(T) + RT\ln f_{CH_4}(T,P,x) \tag{9.68}$$

$$= \mu^{v(0)}_{CH_4}(T) + RT\ln x_{CH_4}P + RT\ln\phi_{CH_4}(T,P,x) \tag{9.69}$$

$$\mu^{l}{}_{CH_4}(T,P,m) = \mu^{l(0)}_{CH_4}(T,P) + RT\ln a_{CH_4}(T,P,m) \tag{9.70}$$

$$= \mu^{l(0)}_{CH_4}(T,P) + RT\ln m_{CH_4}P + RT\ln\gamma_{CH_4}(T,P,m) \tag{9.71}$$

In equilibrium, these chemical potentials are equal, so we obtain:

$$\ln\frac{x_{CH_4}P}{m_{CH_4}} = \frac{\mu^{l(0)}{}_{CH_4}(T,P) - \mu^{v(0)}{}_{CH_4}(T)}{RT} - \ln\phi_{CH_4}(T,P,x) + n\gamma_{CH_4}(T,P,m) \tag{9.72}$$

With the assumption that water vapor pressure is not affected by the existence of $NaCL$ and CH_4, the molar concentration of methane is:

$$x_{CH_4} = \frac{P - P_{H_2O}}{P} \tag{9.73}$$

Where P is the total pressure and P_{H_2O} is the pure water pressure.

The water activity is calculated from the virial expansion of excess Gibbs free energy:

$$\ln\gamma_{CH_4} = \sum 2\lambda_{CH_4-c}.m_c + \sum 2\lambda_{CH_4-a}.m_a + \sum_c\sum_a \xi_{CH_4}m_c m_a \tag{9.74}$$

Substituting Equation (9.74) in Equation (9.72) gives us :

$$\ln \frac{x_{CH_4} P}{m_{CH_4}} = \frac{\mu^{l(0)}{}_{CH_4}}{RT} - \ln \phi_{CH_4} + \sum_c 2\lambda_{CH_4-c} m_c + \sum 2\lambda_{CH_4-a} m_a + \sum_c \sum_a \xi_{CH_4} m_c m_a \tag{9.75}$$

From [97] the equations is selected for the parameters:

$$par(T,P) = c_1 + c_2 T + \frac{c_3}{T} + c_4 T^2 + \frac{c_5}{680 - T} + c_6 P + c_7 P \ln T + \frac{c_8 P}{T} + \frac{c_9 P}{680 - T} + \frac{c_{10} P^2}{T} \tag{9.76}$$

Where the constants are in Table 9.2.

T-P coefficients	$\mu^{l(0)}{}_{CH_4}(T,P)$	$\lambda_{CH_4,Na}$	$\lambda_{CH_4,Cl}$	$\xi_{CH_4,Na,Cl}$
C_1	4.30210345D+01	9.92230792D-02	5.64278808D+00	6.23943799D-03
C_2	6.83277221D-02	2.57906811D-05	8.51392725D-03	
C_3	5.68718730D+03	1.00057752D+03		
C_4	3.56636281D-5			
C_5	5.79133791D+01			
C_6	6.11616662D-03	5.27816886D-05		
C_7	7.85528103D-04			
C_8	9.42540759D-02	1.83451402D-02		
C_9	1.92132040D-02			
C_{10}	9.17186899D-06			

Table 9.2: Solubility coefficients

Finally, the solubility is expressed as:

$$\ln m_{CH_4} = \ln x_{CH_4} \phi_{CH_4} P - \frac{\mu^{01}{}_{CH_4}}{RT} - 2\lambda_{CH_4,Na}(m_{Na} + m_K + 2m_{Ca} + 2m_{Mg}) - 0.06 m_{SO_4} + 0.00624 m_{Na} mCl \tag{9.77}$$

Fig. 9.7 Shows the calculated solubility based on the solubility equation in different

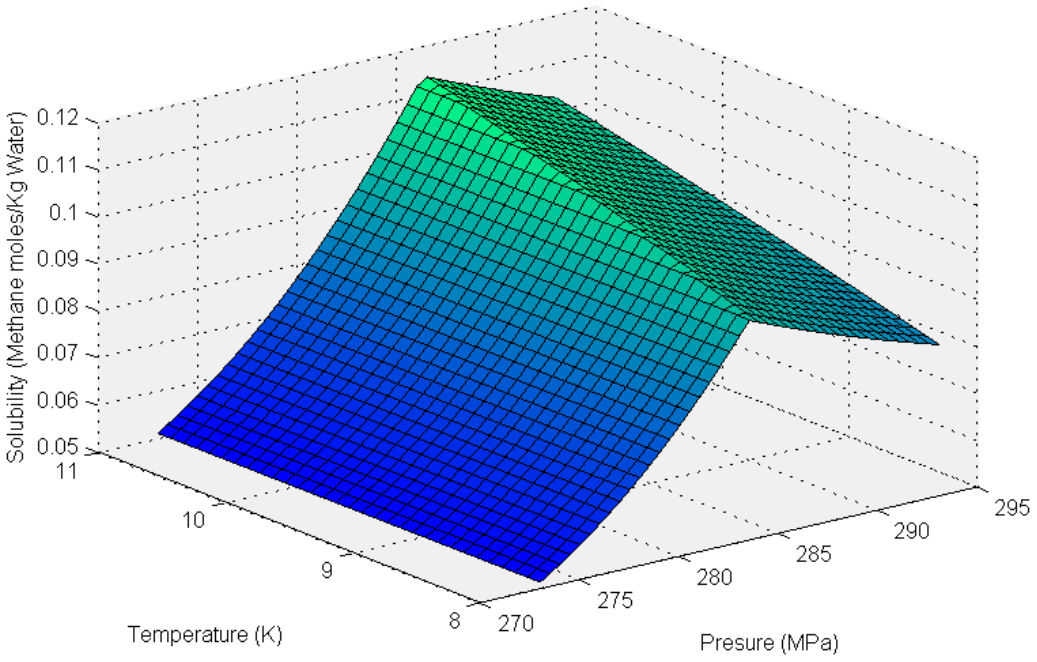

Figure 9.7: Methane solubility in sea water versus temperature and pressure

temperature [273-300]K and pressure range 80-110 bar.

CO_2 hydrate formation equations have been formulated by[98]:

These assumptions have been considered for the CO_2 hydrate formation theory:

i) The change of density considered to be small, since the density of CO_2 hydrate is reported to be, $1.112 \times 10^3 \frac{kg}{m^3}$. The density of liquid CO_2 is same as water.

ii) The reaction rate of hydrate formation is considered to be of $\alpha - th$ order of the kinetic of dissolved concentration of water in the liquid CO_2.

iii) Because of being in the crystalline state, the diffusion of CO_2 is considered to be small.

iv) Condensation of CO_2 hydrate is neglected.

The following equations are derived based on the above assumptions:

$$\frac{\partial c_w}{\partial t} = D\frac{\partial^2 C_w}{\partial x^2} - nkC_w{}^{\alpha} \tag{9.78}$$

$$\frac{\partial C_h}{\partial t} = kC_w{}^{\alpha} \tag{9.79}$$

$$C_w = (1 - \frac{C_h}{\rho M^{-1}})C_r \tag{9.80}$$

The initial conditions are:

$$C_r = 0,\ \ C_h = 0,\ \ t \leq 0,\ \ 0 < x < \infty \tag{9.81}$$

Boundary conditions are as follows:

$$C_r = S,\ \ t > 0,\ \ x = 0 \tag{9.82}$$

$$\frac{\partial C_r}{\partial x} = 0,\ \ t > 0,\ \ x \to \infty \tag{9.83}$$

$$\frac{\partial C_h}{\partial x} = 0,\ \ t > 0,\ \ x \to \infty \tag{9.84}$$

Where, C_w and C_r are the apparent and real concentration of water in liquid CO_2. t is time, x is the distance of in liquid CO_2 from the interface, C_h is the concentration of CO_2 hydrate, D is the diffusion constant of water in liquid CO_2. α is the order of reaction, ρ is the density of CO_2 hydrate, M is the molar mass of CO_2 hydrate, s is the solubility of water in liquid CO_2. The actual hydrate formation time is defined as t_f. The thickness of CO_2 hydrate is calculated to be:

$$\sigma = \frac{\int_0^\infty C_h}{\rho M^{-1}}, \;\; t = t_f \tag{9.85}$$

The hydrate concentration rate is:

$$\frac{dC_h}{dt} = k(1 - \frac{C_h}{\rho M^{-1}})s^\alpha, \;\; x = 0 \tag{9.86}$$

By integrating abobe equation, from C_h=0 to C_h=0.99, the formation time:

$$t_f = \frac{6.91\rho}{Mks^\alpha} \tag{9.87}$$

9.9 Fuel Cell Modeling

Operating the fuel cell at high pressures has beneficial effects on the fuel cell system. Since the behavior of gases is different from the ideal behavior, the fugacity coefficients should be computed. The compressibility of real gases is estimated based on second virial coefficients of the Van der Waals equation of state in Eq. (9.88):

$$Z = \frac{P\bar{V}}{RT} = (1 + \frac{B_{2V}(T)}{\bar{V}} + \frac{B_{3V}(T)}{\bar{V}^2} + ...) = 1 + (b - \frac{a}{RT})\frac{1}{\bar{V}} + \frac{b^2}{\bar{V}^2} + ... \tag{9.88}$$

Where, Z is the compressibility factor of real gas. a, b are parameters of Van der Waals equation of state. The fugacity coefficient relation with real partial pressure of gases is expressed as:

$$\ln \gamma = \ln \frac{f}{P} = \int_0^P \frac{Z-1}{P'}\, dP' \tag{9.89}$$

Or:

$$\gamma = \frac{f}{P} = exp[(b - \frac{a}{RT})\frac{P}{RT}] \tag{9.90}$$

The entropy of reactant and product gases of the fuel cell at specific pressure of 100 bar are calculated as Eq. (9.91):

$$s - s^\circ = \bar{s_2}^\circ - \bar{s_1}^\circ - R_u \ln \frac{P_2}{P_1} \tag{9.91}$$

Where, s° is the entropy at standard temperature and pressure. $\bar{s}^\circ$ are the entropy independent of pressure. Pressurizing fuel cell in order to increase reactant partial pressure will increase the reversible voltage. However, because the logarithmic nature of the voltage, improvement will be slight. Total electrochemical reaction that is considered in SOFC is the reaction between fuel (hydrogen) and oxygen:

$$H_2 + O_2 \rightarrow \frac{1}{2} H_2O \tag{9.92}$$

The Nernst potential which is the maximum voltage is calculated as a function of entropy difference between reactants and products of the electrochemical reaction,

the fugacity of gases and the operating temperature of SOFC which is assumed to be $700°C$.

$$E_{Nernst} = E^{\circ} + \frac{\Delta s}{nF}(T - T_0) - \frac{RT}{nF} \ln \frac{f_{H_2O}}{f_{H_2} f_{O_2}} \tag{9.93}$$

Where, n is the number of electrons transferred in the equation. F is Faraday constant. f_{H_2O}, f_{H_2} and f_{O_2} are fugacities of gases involved in the electrochemical reaction. The activation polarization of the SOFC is modeled by Butler-Volmer equation, Eq. (9.94):

$$j = j_0(e^{\frac{\alpha n F \eta}{RT}} - e^{\frac{-(1-\alpha) n F \eta}{RT}}) \tag{9.94}$$

Where, j_0 is the exchange current density. α is electron transfer coefficient. η is the activation polarization. The ohmic polarization of the fuel cell is in form of:

$$\eta_{ohmic} = i(R_{electrode} + R_{ionic}) \tag{9.95}$$

Where $R_{electrode}$ and R_{ionic} are the resistance of electrode and electrolyte respectively. Electrode resistance is negligible comparing to ionic resistance and it is neglected in this study. Eq. (9.96) describes the mass concentration polarization:

$$\eta_{conc} = \frac{RT}{nF} \ln \frac{j_L}{j_L - j} \tag{9.96}$$

j_L is the limiting current density and j is the current density of the cell. Hence, total voltage of the cell could be described in the equation, which is the sum of the different types of the polarizations of the fuel cell and the thermodynamic voltage (Nernst potential) in Eq. (9.97) and Eq. (9.98):

$$V = E_{thermo} - \eta_{act,anode} - \eta_{act,cathode} - \eta_{ohm} - \eta_{conc} \tag{9.97}$$

Or:

$$V = E_{thermo} - (Y_1 + Y_2 \ln j) - (Y_3 + Y_4 \ln j) - jASR_{ohmic} - Y_5 \ln \frac{j_L}{j_L - j} \tag{9.98}$$

Y_1, Y_2 are activation polarization constants of anode compartment and Y_3, Y_4 are activation polarization constants of cathode compartment, determined from Butler-Volmer equation. Y_5 is the mass concentration polarization constant.

Enthalpies of reaction at high pressures for the steam methane reformer has been developed and expresses the enthalpy of real gas based on pressure, temperature and second virial coefficients in Eq. (9.99) and Eq. (9.100).

$$\left(\frac{\partial h}{\partial P}\right)_T = v - T\left(\frac{\partial v}{\partial T}\right)_P \tag{9.99}$$

$$H = H^\circ + B(T)P - T\frac{\partial B(T)}{\partial T} \tag{9.100}$$

Eq. (9.101) and (9.102) determines the partial pressure of hydrogen entering the SOFC anode compartment and water in fuel cell exit, assuming the ideal gas law :

$$P_{H_2} = P \times \frac{(1 - U_{f,H_2}) \times \dot{N}_{H_{2,SMR}}}{\dot{N}_{H_2O_{SMR}} + (1 - U_{f,H_2}) \times \dot{N}_{H_{2,SMR}} + \dot{N}_{CO_{2,SMR}} + \dot{N}_{CO_{SMR}} + \dot{N}_{CH_{4,SMR}} + \dot{N}_{H_2O_{prod}}} \tag{9.101}$$

$$P_{H_2O} = P \times \frac{\dot{N}_{H_2O_{SMR}} + \dot{N}_{H_2O_{prod}}}{\dot{N}_{H_2O_{SMR}} + (1 - U_{f,H_2}) \times \dot{N}_{H_{2,SMR}} + \dot{N}_{CO_{2,SMR}} + \dot{N}_{CO_{SMR}} + \dot{N}_{CH_{4,SMR}} + \dot{N}_{H_2O_{prod}}} \tag{9.102}$$

Where P is the total operating pressure, $\dot{N}_{H_{2,SMR}}, \dot{N}_{CO_{2,SMR}}, \dot{N}_{CO_{SMR}}, \dot{N}_{CH_{4,SMR}}, \dot{N}_{H_2O_{SMR}}$ are the molar flows of hydrogen, carbon dioxide, carbon monoxide, methane and water in reformer exit that enters the anode component of fuel cell. $\dot{N}_{H_2O_{SMR}}$ is the water produced in anode part of the SOFC. $U_{f,H_2}$is hydrogen utilization in anode compartment. The partial pressure of oxygen in the cathode component is in the form of Eq. (9.103):

$$P_{O_2} = P \times (1 - U_{f,O_2})\dot{N}_{O_2} \tag{9.103}$$

Where U_{f,O_2} is oxygen utilization in the cathode component. Eq.(9.104) to (9.106)

Parameter	Value Used
Temperature	$700°C$
Anode exchange current density ($j_{0,anode}$)	$10\frac{A}{cm^2}$
Cathode exchange current density ($j_{0,cathode}$)	$0.1\frac{A}{cm^2}$
α_{O_2}	0.5
α_{H_2}	0.5
ASR_{ohmic}	0.04
Limiting current density (j_L)	$2\frac{A}{cm^2}$
$S_(H_2O)$	$193.71\frac{j}{mol.K}$
$S_(H_2)$	$128.25\frac{j}{mol.K}$
$S_(O_2)$	$205.18\frac{j}{mol.K}$

Table 9.3: Solid Oxide Fuel Cell properties used in modeling

express the fugacity of the reactants and products in the SOFC, derived from second virial coefficients from Van der Waals equation of state:

$$f_{H_2} = P_{H_2} \times e^{(0.02665-\frac{0.2464}{RT})\times\frac{P_{H_2}}{RT}} \tag{9.104}$$

$$f_{O_2} = P_{H_2} \times e^{(0.03186-\frac{1.382}{RT})\times\frac{P_{O_2}}{RT}} \tag{9.105}$$

$$f_{H_2} = P_{H_2O} \times e^{(0.03049-\frac{5.537}{RT})\times\frac{P_{H_2O}}{RT}} \tag{9.106}$$

The properties of Solid oxide fuel cell that is used in the model are shown in Table 9.3.

9.9.1 Steam Methane Reformer Modeling

Steam methane reforming (SMR) has been studied as an external reformer and their synergetic effects has been included in the calculations. SMR has been modeled at 100 bar total pressure and various temperatures. The total equilibrium reaction of steam methane reformer and water-gas shift are the following:

Steam methane reforming (SMR):

$$CH_4 + H_2O \rightleftharpoons CO + H_2 \tag{9.107}$$

Water-Gas shift reaction (WGS):

$$CO + H_2O \rightleftharpoons CO_2 + H_2 \tag{9.108}$$

Chapter 10

Results

Solid Oxide Fuel Cell at high pressures has been modeled using the equations of the section 9.9. Fig. 10.1 shows the fuel cell power for one cell at different oxygen and hydrogen utilizations. The cell operates for an area of 50 cm^2. Also the cell operates at simulated deep ocean environments which is at a pressure of 100 bar, at which the conditions for hydrate formation are stable. The cell power decreases by increasing hydrogen utilization which is also the case for fuel cell operating at standard conditions (1 atm). Increasing hydrogen utilization will cause a reduction in the voltage of the fuel cell because of the less leftover gases at the outlet of the cell. Increase in hydrogen and oxygen utilization will both decrease the concentration of the hydrogen and oxygen at anode and cathode of the fuel cell at this will have an effect on the thermodynamic maximum voltage (Nernst potential) and the exchange current density of the fuel cell. This shows that for obtaining larger powers (close to the target power of 1000W), we

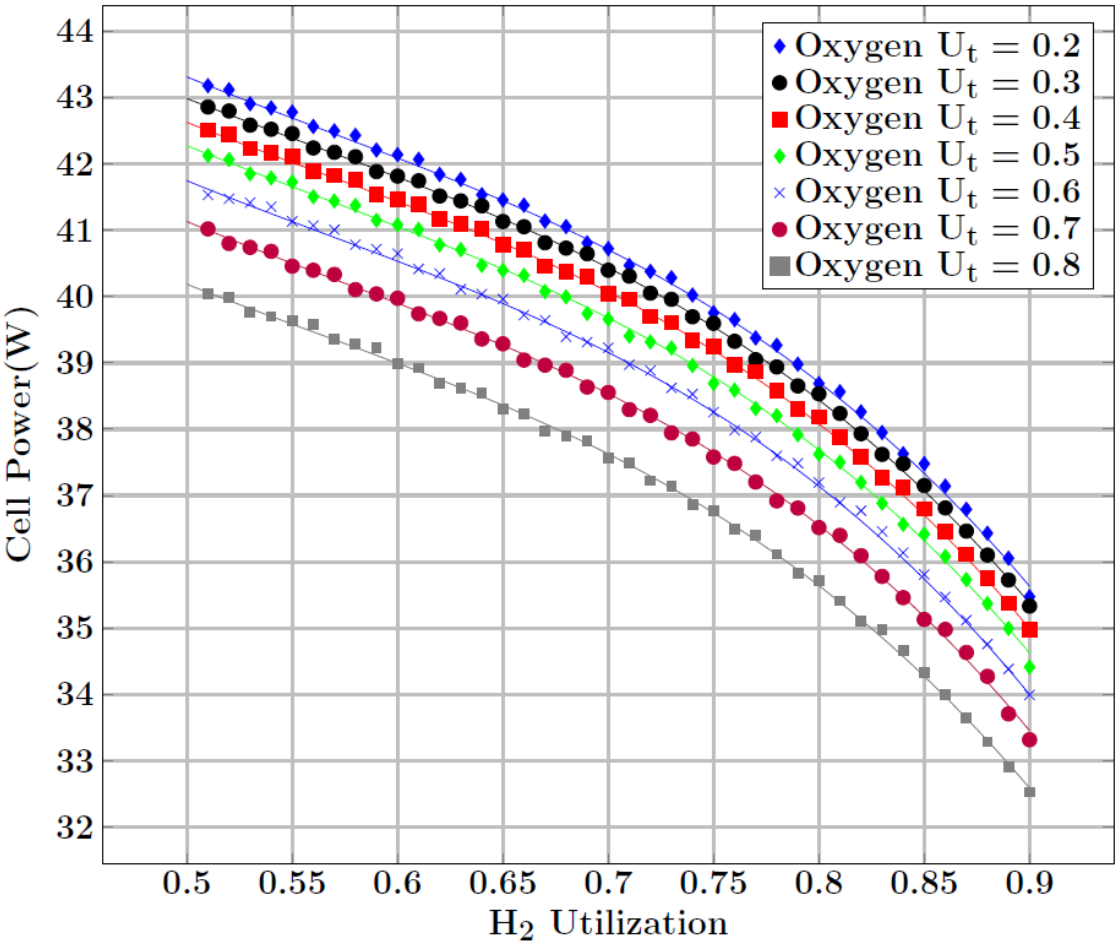

Figure 10.1: SOFC power at different levels hydrogen and oxygen utilizations.

have to choose a fuel cell with lower fuel utilization. However, this decision will affect the net efficiency of the system, since in that case the reformer requires more hydrogen.

Fig. 10.2. shows the current density of cell varying with hydrogen and oxygen utilization at high pressure (100bar). The operation of the system requires us to keep the cell voltage constant at 0.7 (V), since by varying the reactant stream (Hydrogen and Oxygen), we can change the operating voltage of the cell. If we want to obtain the same amount of power, with different fuel utilization at constant operating voltage (In

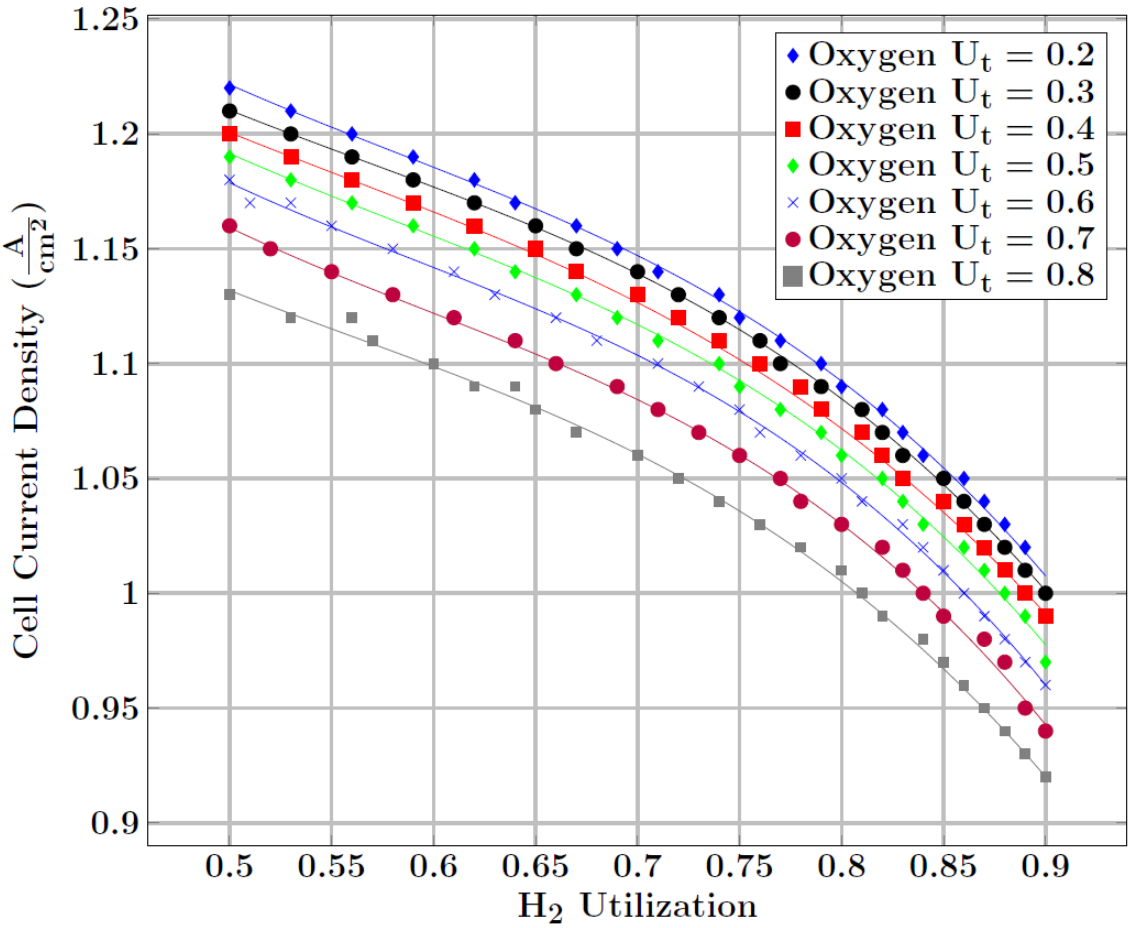

Figure 10.2: SOFC current density at different levels hydrogen and oxygen utilizations

this case 0.7 (V)), the current density should be changed accordingly. Since the target power is same, the current density variation has the same trend as the power varies with the hydrogen and oxygen utilization.

Fig. 10.3 shows the variation of the Nenst potential of the cell with operating pressure of the fuel cell which is determined by the methane hydrate stable condition pressure. As we could see increasing pressure from 50 bar to 140 bar, has a slight improvement in Nernst potential. However it does not seem to be significant. Variation of hydrogen utilization has much greater effect on the fuel cell performance than the

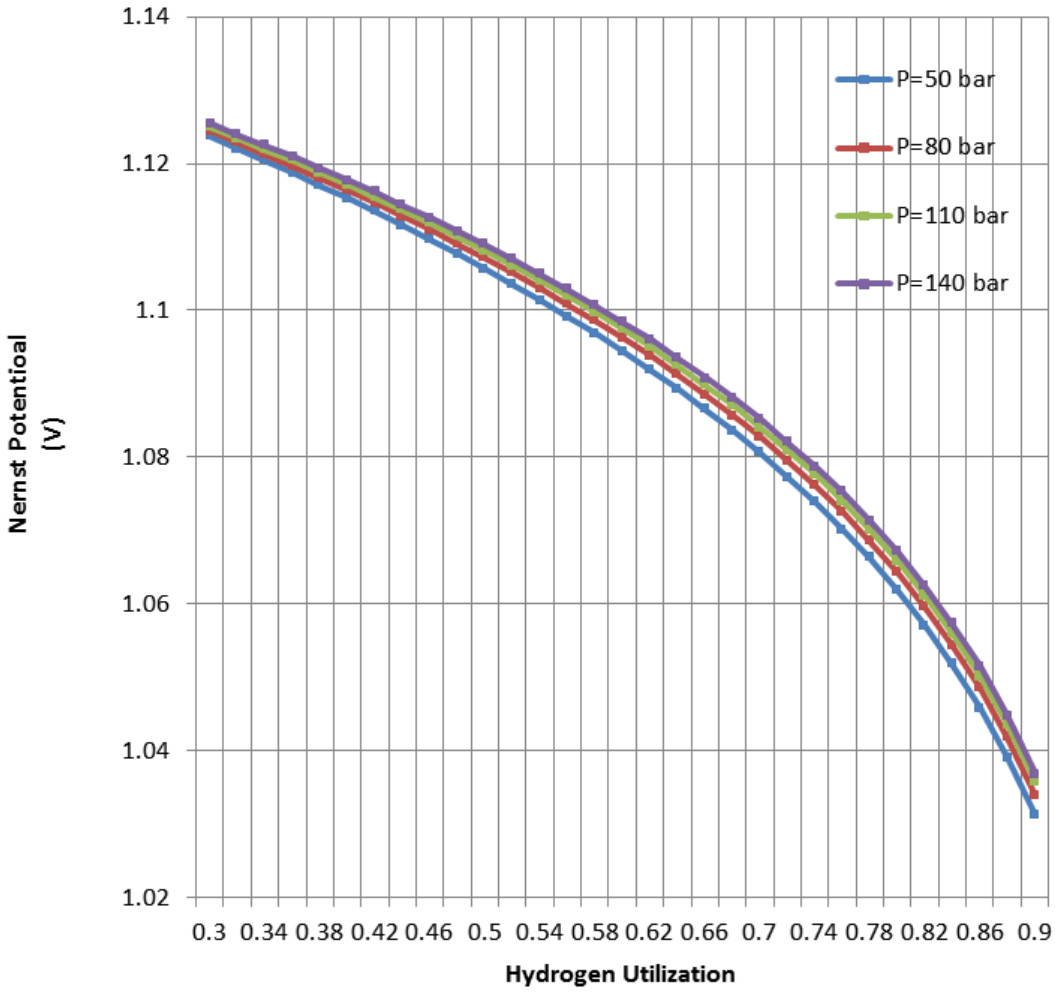

Figure 10.3: Variation of Nernst potential with operating pressure of the fuel cell (Oxygen utilization = 0.5)

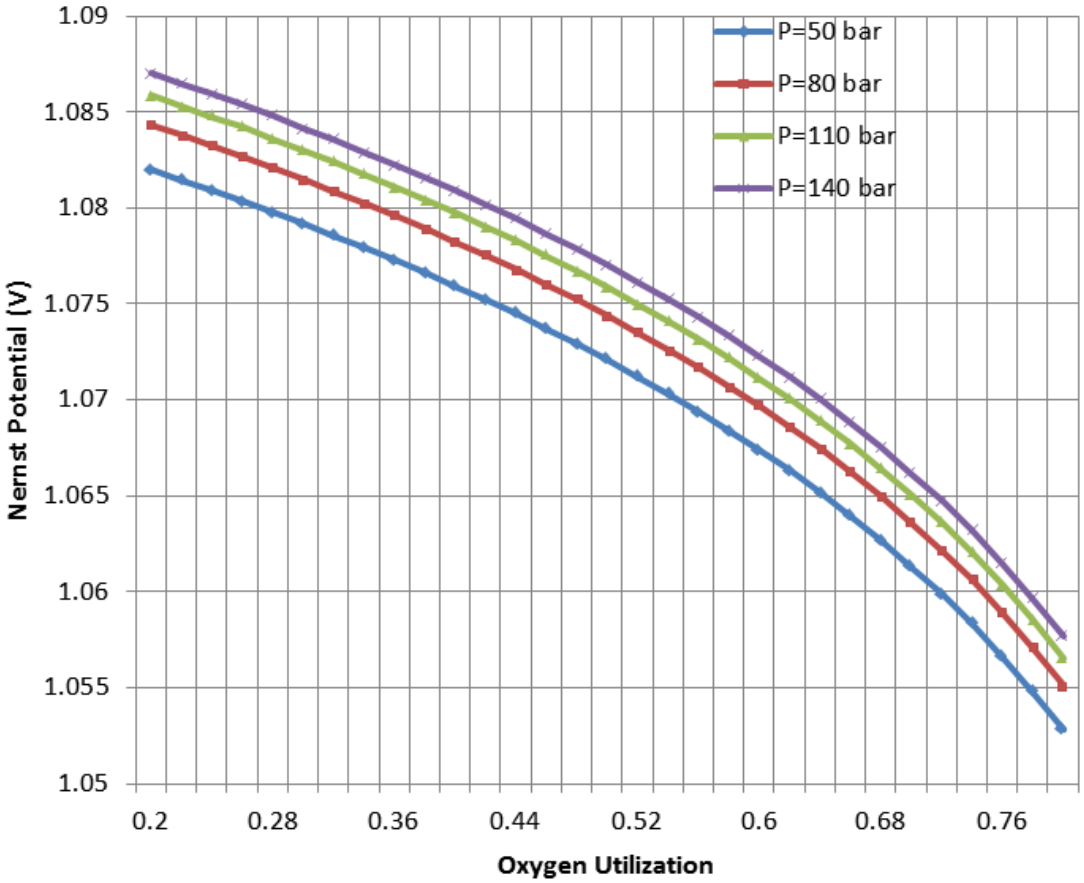

Figure 10.4: Variation of Nernst potential with oxygen utilization (hydrogen utilization=0.7)

pressure.

Fig. 10.4. shows the variation of the thermodynamic Nernst potential with oxygen utilization in fuel cell cathode in the range of 0.2 to 0.8 and the pressure range of P=50 bar to P=140 bar side of the fuel cell.

Fig.10.5. shows the effect of high pressure on the stoichiometric concentrations of the effluent gases in the steam methane reformer temperature range of [750 to 990] K and in the pressure range of [50 bar to 130 bar]. As we can observe, the concentration of the produced hydrogen is decreased from 1.5 to 1 which shows the negative effect of

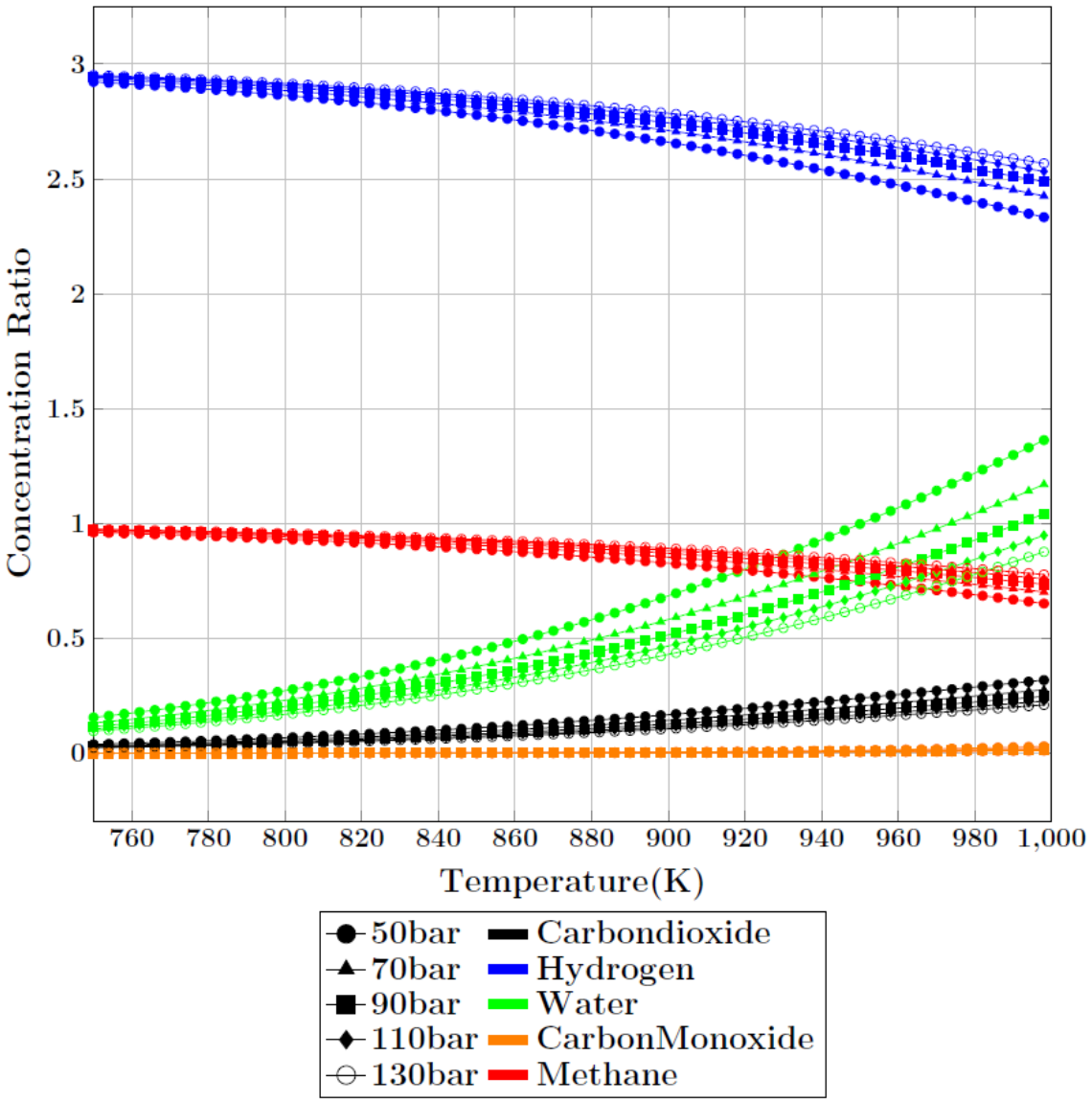

Figure 10.5: Variation of SMR equilibrium concentration in temperature range of [750-1000]K

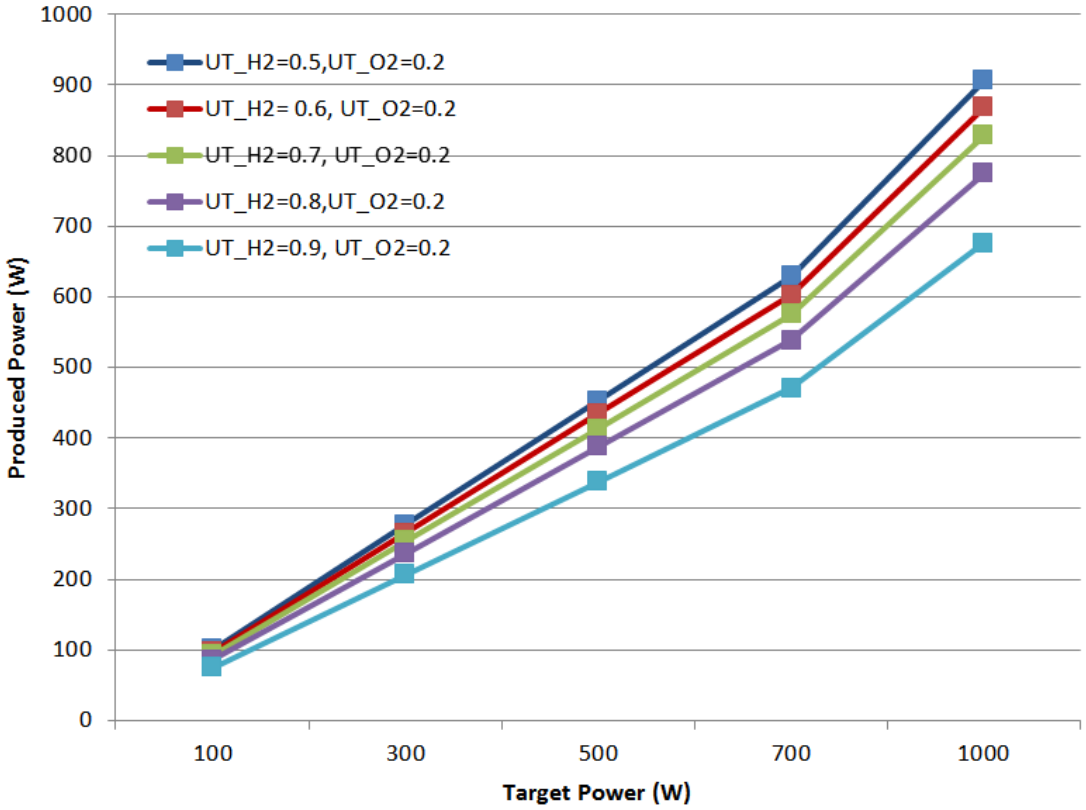

Figure 10.6: Produced power versus target power change with hydrogen utilization

high pressure on the H_2 production. High pressure might slightly improve the Nernst potential in cell, however it will negatively affect the performance of the stem methane reformer which is greater than the positive effect of pressure on the Nernst potential.

Fig. 10.6 and Fig.10.7 describe the physical performance of the high pressure fuel cell which are dependent on the reactants utilization in the anode and cathode. As we observed in Fig. 10.1., by increasing the reactant utilization in the cell, the power decreases, since we have lower concentration of leftover reactants at the outlet of the fuel cell. This will have an effect on the produced power. Fig. 10.6. shows that by increasing H_2 utilization the reduction in the produced power is not uniform and it

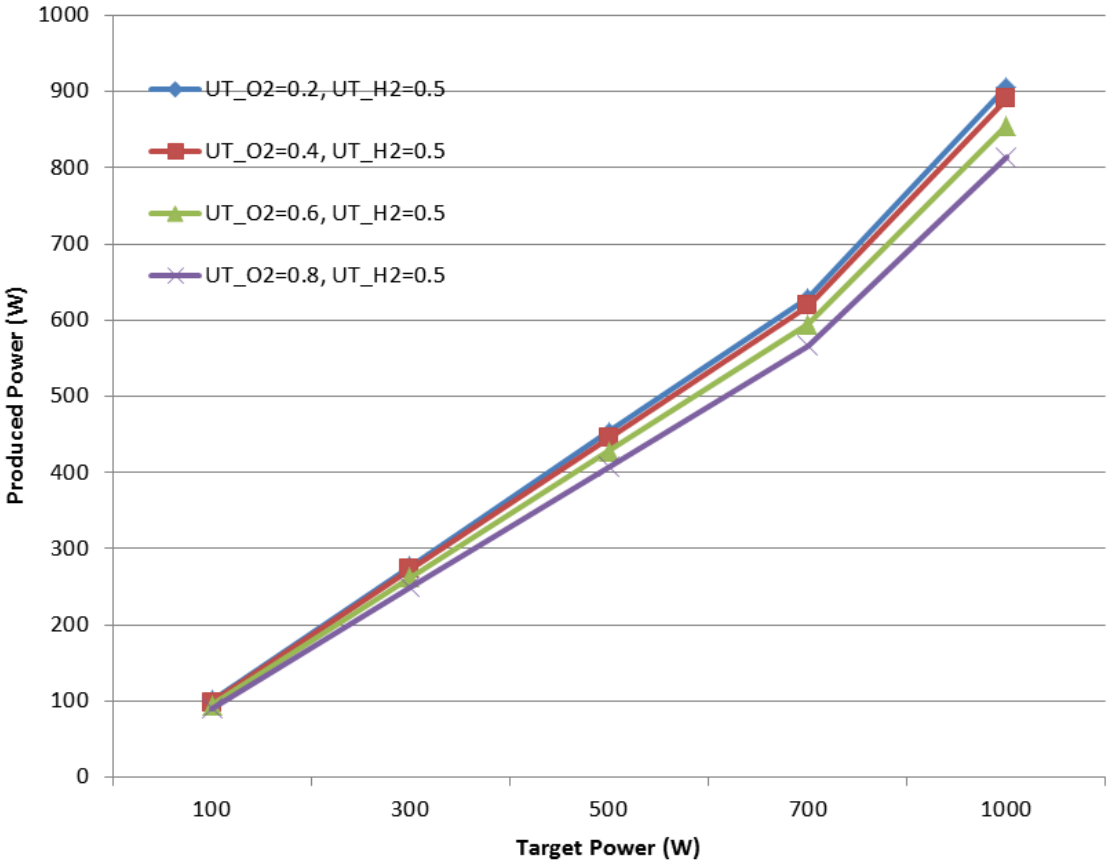

Figure 10.7: Produced power versus target power change with oxygen utilization

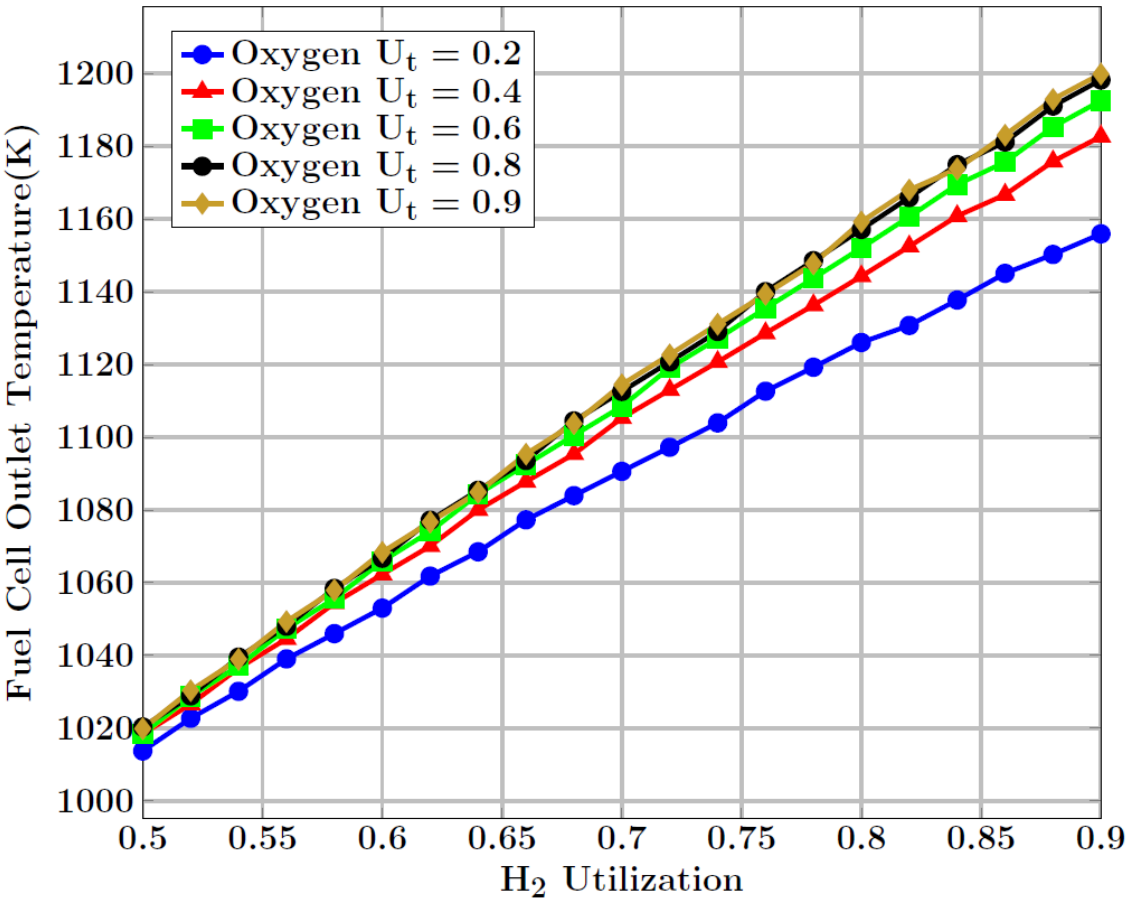

Figure 10.8: SOFC exit temperature change as a function of hydrogen utilization.

will drop sharply as hydrogen utilization gets close to 0.9. This case is less significant in Fig. 10.7., which has the same trend as the Fig. 10.7., but the variation of oxygen utilization does not have that much effect on the produced power reduction. It should be mentioned that all of these parameters are dependent on the parameters of the SOFC which are shown in the Table 9.3.

Fig. 10.8., shows that the outlet temperature of the fuel cell effluent gases variation in the range of hydrogen utilization from [0.5 to 0.9] and oxygen utilization from [0.2 to 0.9]. The fuel cell effluent gas temperature increases when hydrogen utilization

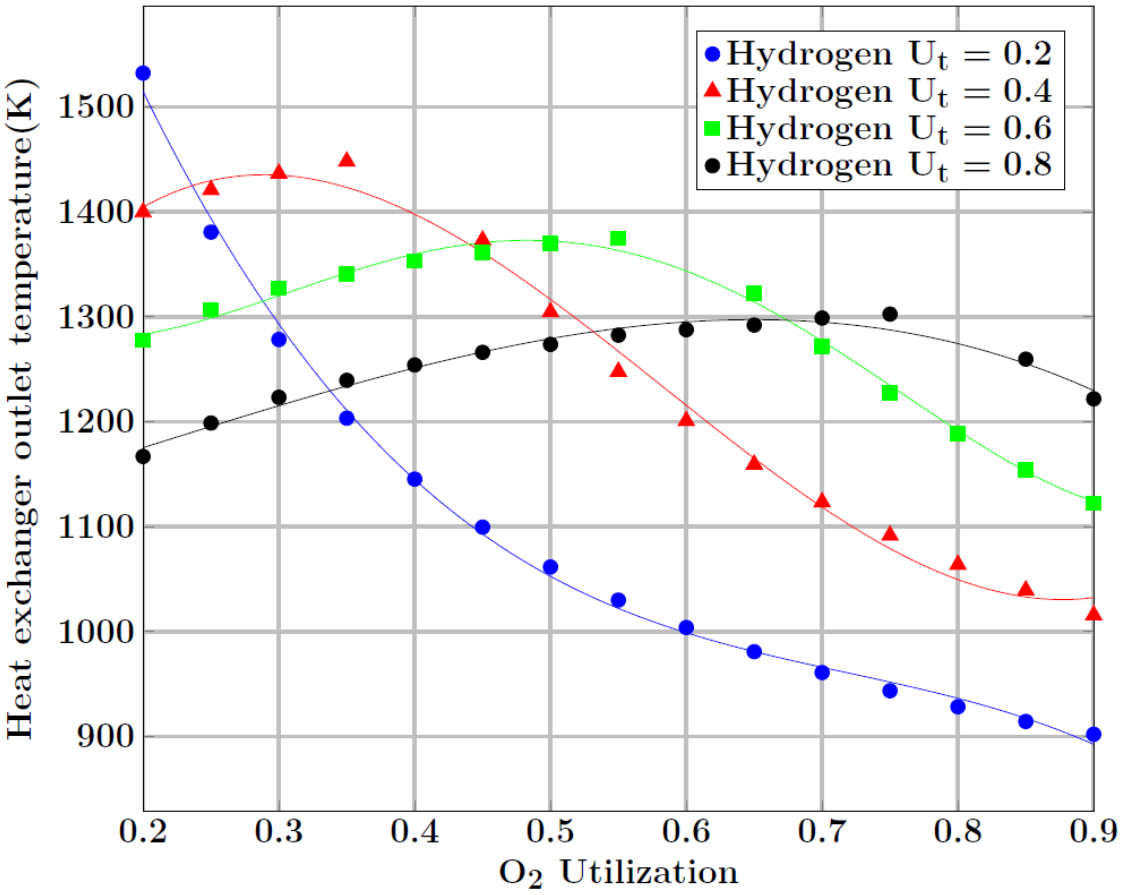

Figure 10.9: Heat exchanger outlet temperature change as a function of oxygen and hydrogen utilization.

increases mainly because of the high electrochemical reaction rate, and lower leftover hydrogen gas at the outlet of the fuel cell. At lower oxygen utilizations, the temperature drops significantly because of the higher concentration of oxygen at the outlet and its cooling effect. However, at higher utilizations of oxygen the, temperature of the fuel cell effluent gases will not change significantly because of the low concentrations of oxygen the negligible cooling effect.

Fig. 10.9 shows the temperature of the effluent gases of the heat exchanger in

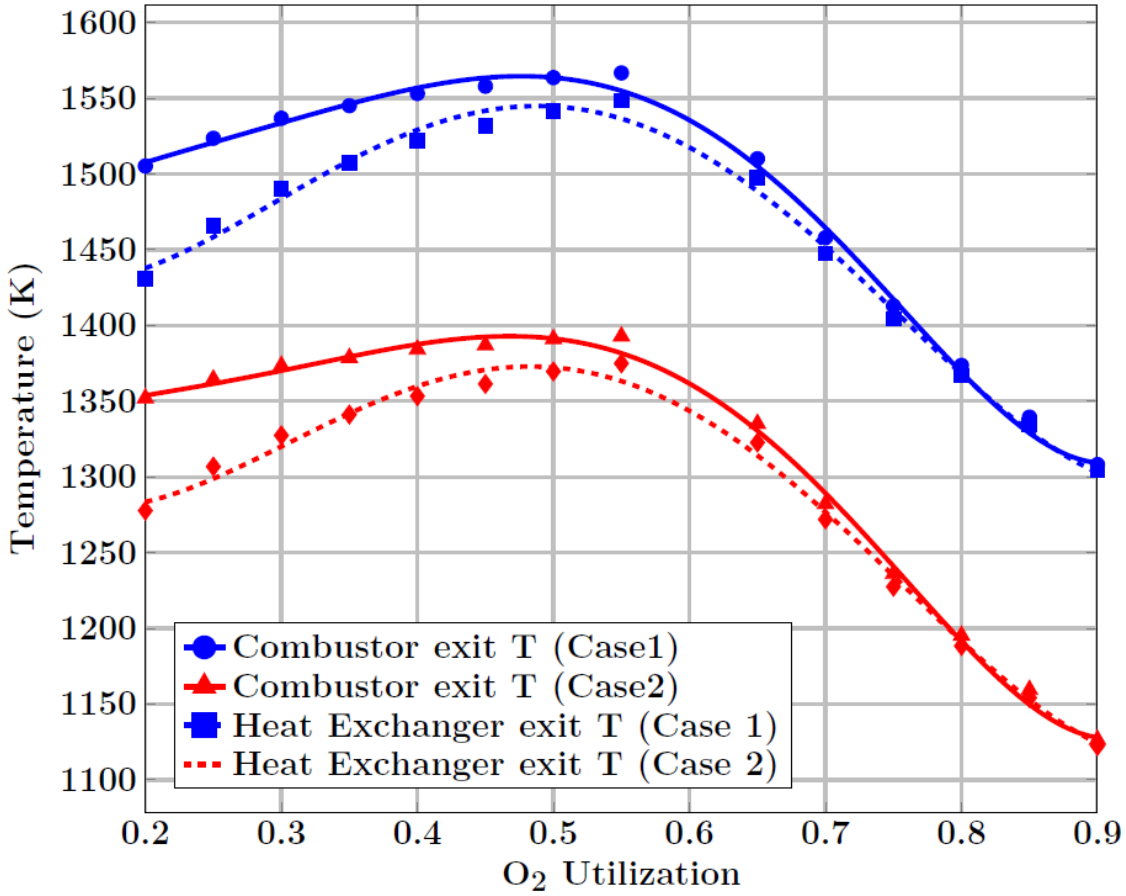

Figure 10.10: Combustor and heat exchanger exit temperature change as a function of hydrogen and oxygen utilization for case 1 and case 2 at hydrogen utilization of 0.6

variation with oxygen utilization and hydrogen utilization. At low hydrogen utilization, the temperature of the heat exchanger (Heat exchanger, which provides heat to preheat the oxygen) decreases with the oxygen utilization. At high hydrogen utilization, the temperature of the effluent gases of the heat exchanger, has increasing and decreasing trends.

Fig. 10.10 shows the variation of the temperature with oxygen utilization for two different cases: Case 1: Heat of the steam methane reformer is provided by burning the part of the dissociated methane from the hydrate sediment Case 2: Heat of the

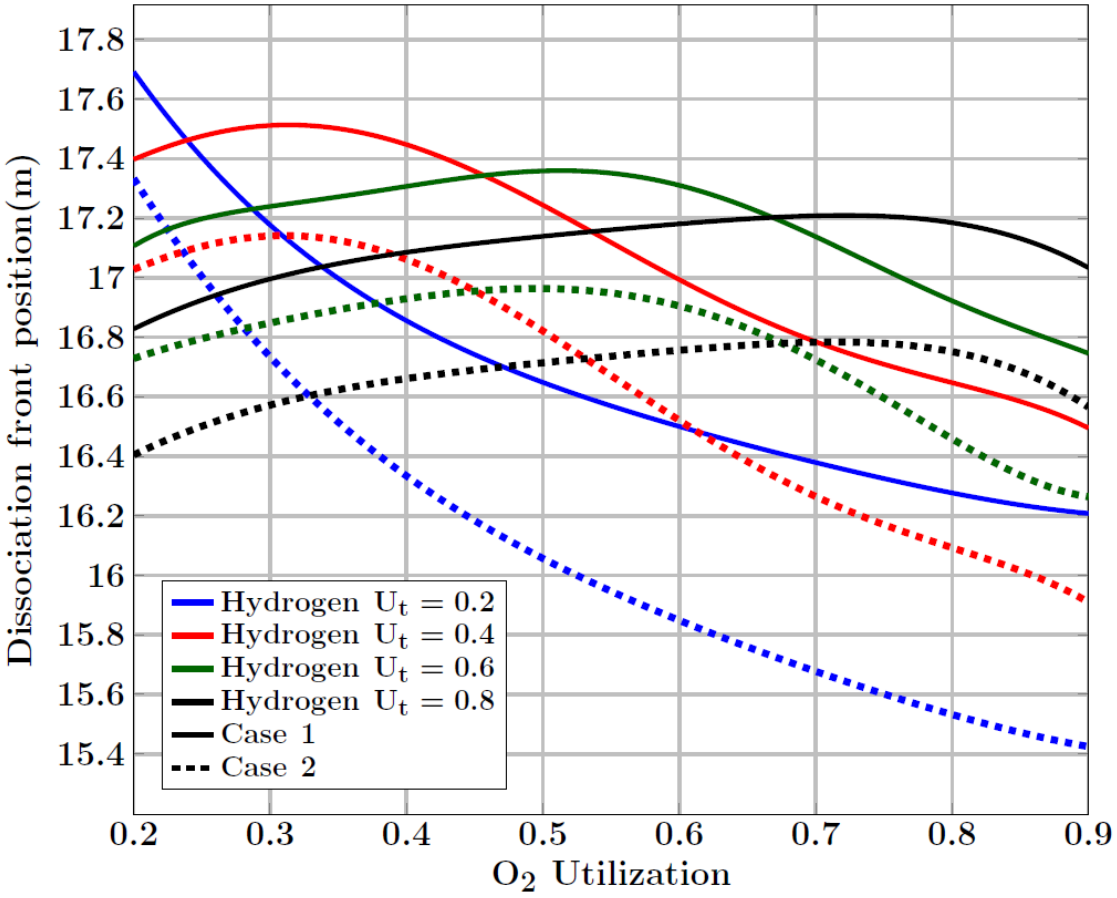

Figure 10.11: Dissociation front location as a function of hydrogen and oxygen utilization.

steam methane reformer is provided by the fuel cell effluent gases.

Fig. 10.12 shows the temperature rise development in the hydrate sediment for two specific fuel cell operational parameter (H_2 utilization=0.62, O_2 utilization= 0.4) and (H_2 utilization=0.62, O_2 utilization= 0.4) . The temperature profile depends on several parameters of hydrate layer including, permeability, temperature of dissociation, pressure of dissociation, thermal conductivity of both zones, etc. These values are shown in the Table 9.1..

Fig. 10.13 shows that the dissociation front location does not change significantly

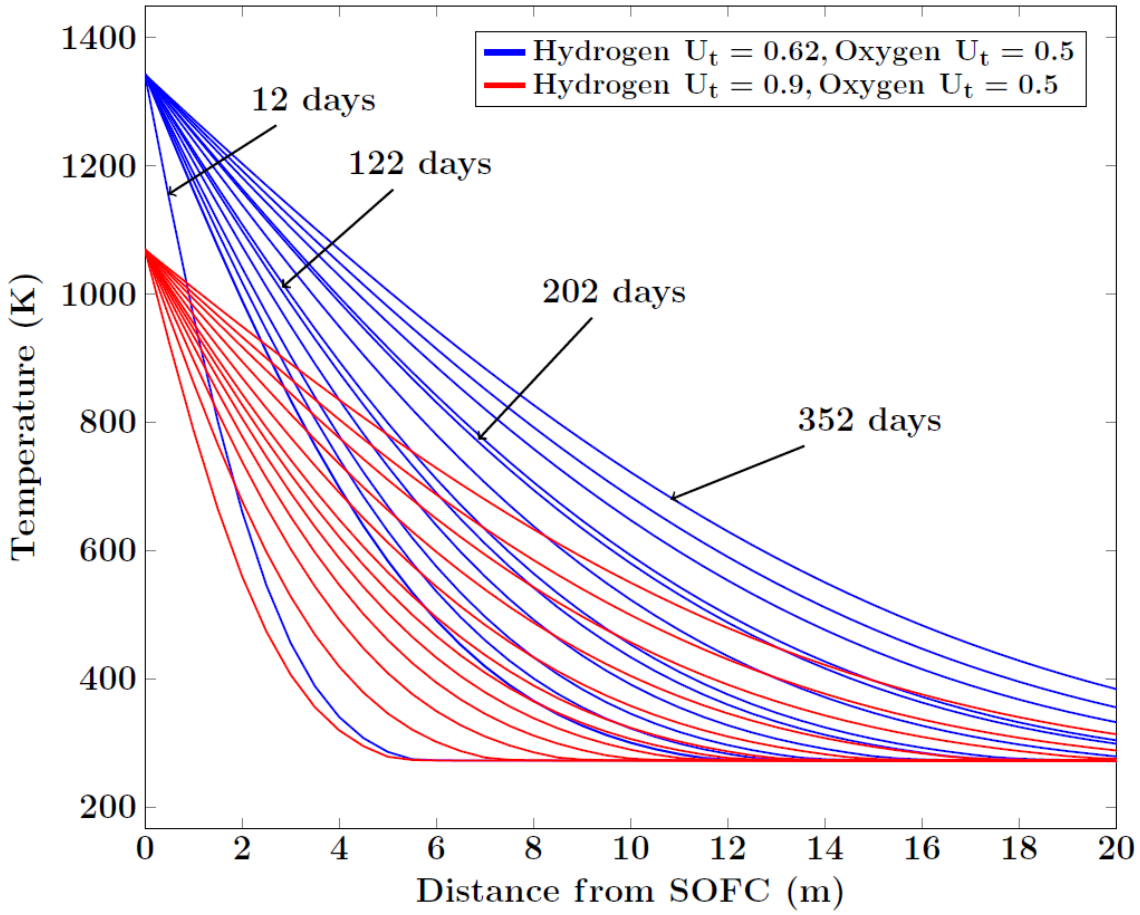

Figure 10.12: Temperature development in the hydrate layer varying with distance from the fuel cell system for H_2 utilization=0.62, O_2 utilization= 0.5 and H_2 utilization=0.9, O_2 utilization= 0.5

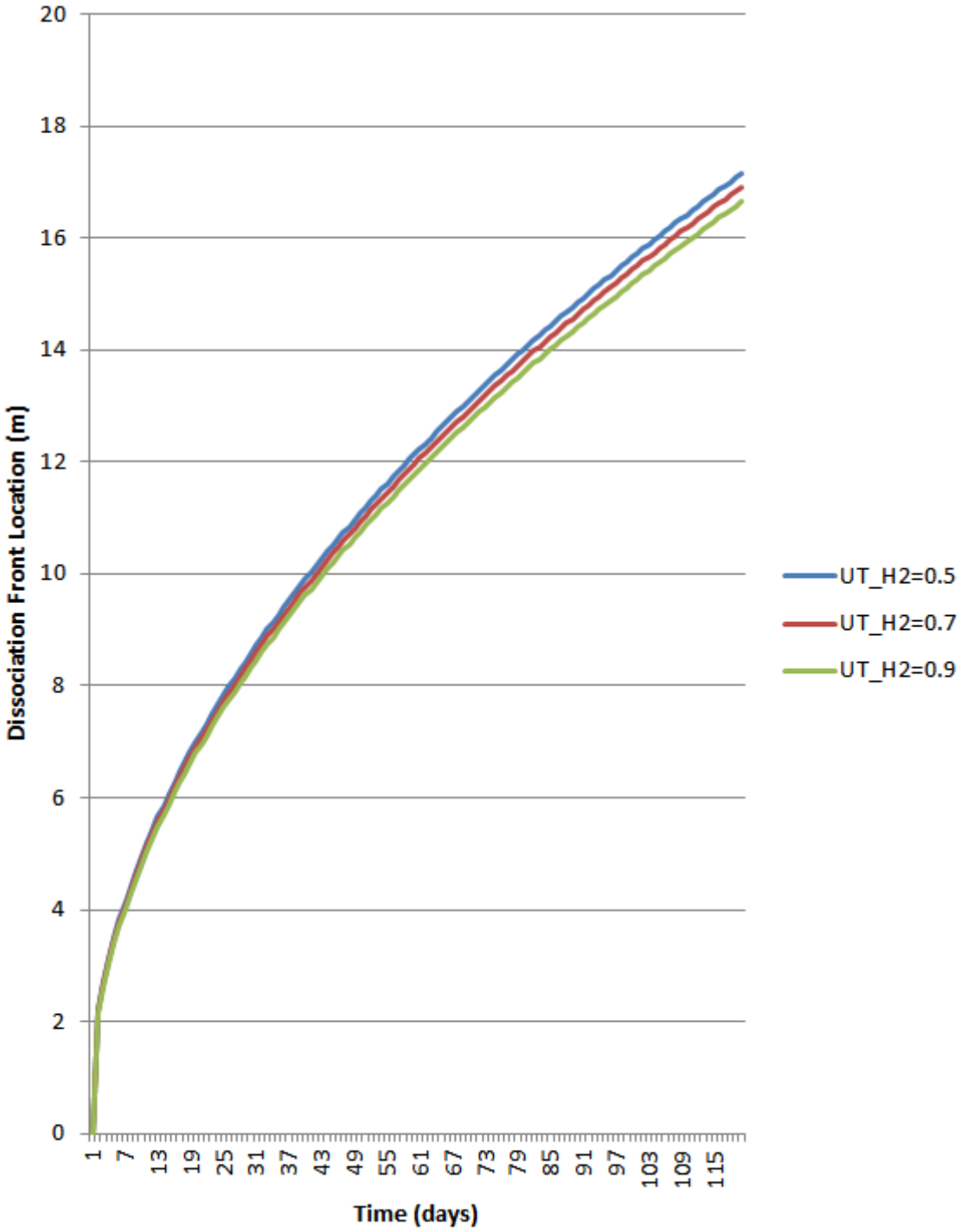

Figure 10.13: Dissociation front location in the hydrate layer varying with time at different hydrogen utilization (Oxygen utilization=0.2)

with hydrogen utilization at the beginning of the initiation of the dissociation process. We can see the significant dissociation location difference after 100 days. This is mainly because of the fact that the heat exchanger outlet temperature decreases continuously with rising H_2 utilization at low oxygen utilizations, but it has increasing and decreasing trend at higher oxygen utilization.

Fig. 10.15 shows the dissociation front location varying with time, and different porosities of hydrate layer. Increased porosity will increase the chance of higher hydrate saturation. So the dissociation front moves slower than in the layer with less porosity because there is more needed heat of dissociation to decompose the layer.

Fig. 10.16 and Fig 10.17, demonstrate the Non - dimensioned dissociation front location in the hydrate layer varying with temperature of dissociation at different operating conditions of the hydrogen and oxygen (utilization). The value of Ξ decreases as the temperature of dissociation increases. Because of the higher temperature of dissociation, there is less temperature difference between the thermal stimulator source and the cold dissociation front, So, the heat flux is less effective and the hydrate front moves slower than the case with lower temperature of dissociation. Also, at oxygen utilization of 0.2, we have decreasing trend of heat exchanger temperature with increasing hydrogen utilization. So, the dissociation front moves slower than the case of less hydrogen utilization.

Fig. 10.18, shows that the dissociation front moves extremely fast in the beginning of the dissociation process and then there is a reduction in the speed of the dissociation front movement. Fig. 10.19 , shows the variation of Non - dimensioned dissociation

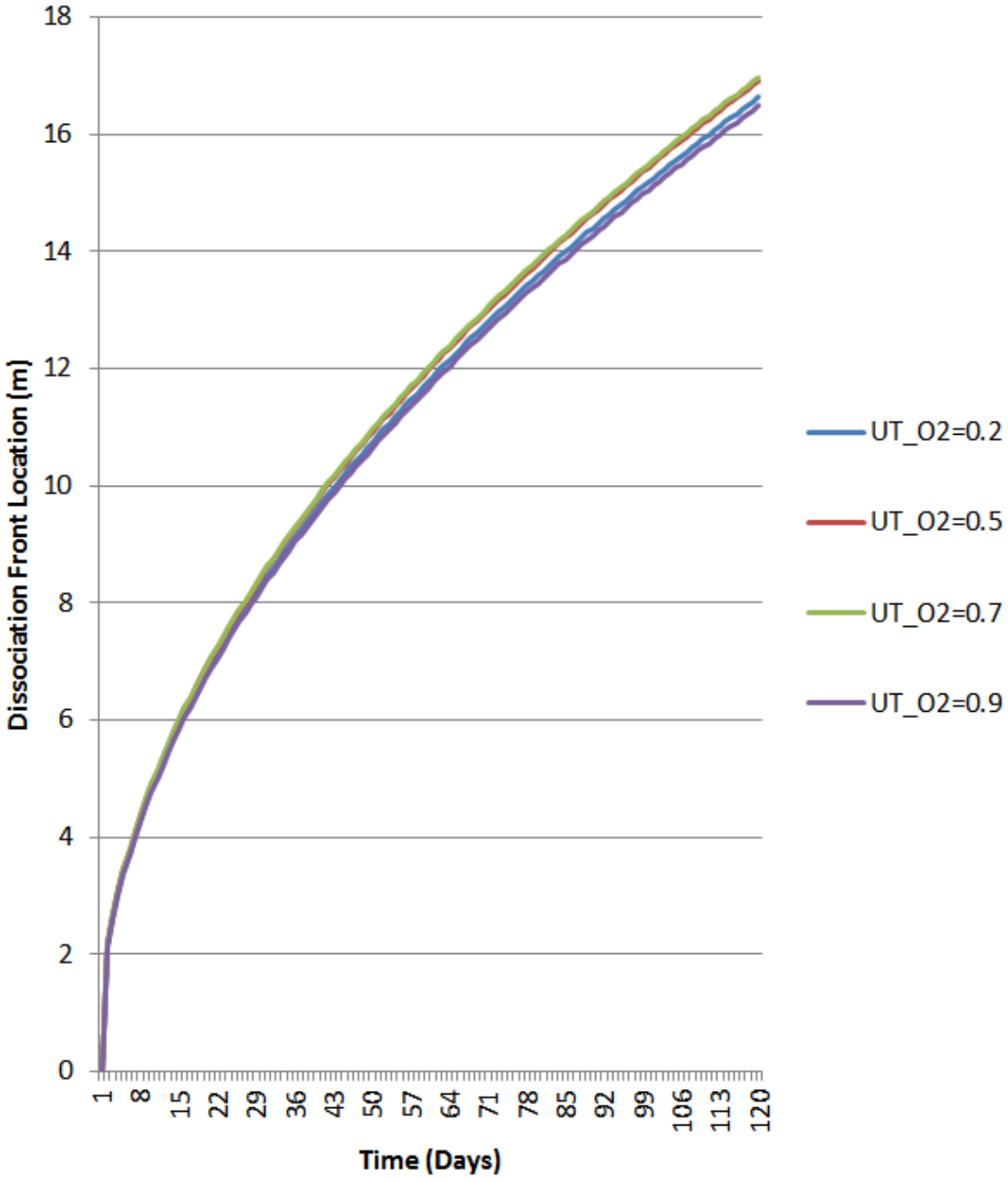

Figure 10.14: Dissociation front location in the hydrate layer varying with time at different oxygen utilization (Hydrogen uutilization =0.7)

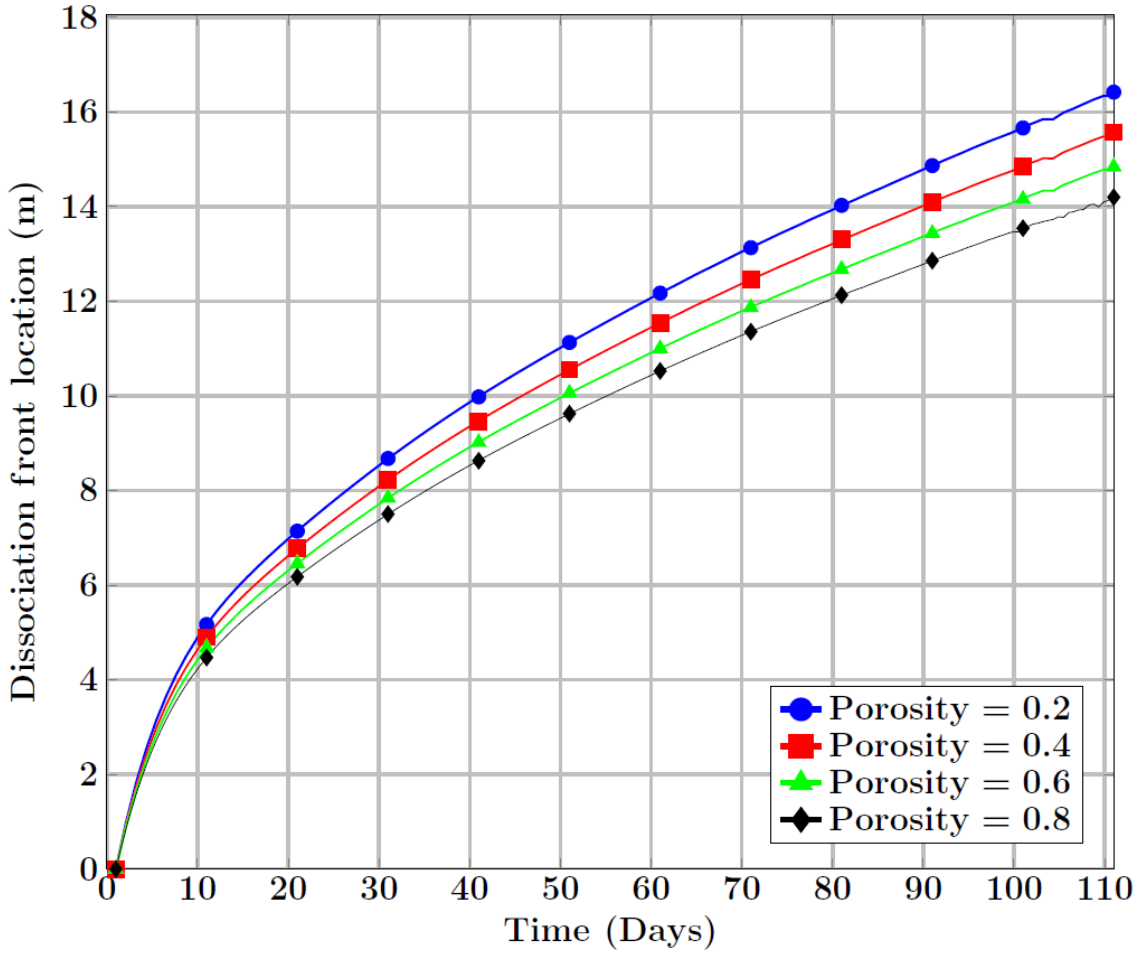

Figure 10.15: Dissociation front location in hydrate layer during time at different porosities (Hydrogen utilization=0.6, Oxygen Utilization=0.5)

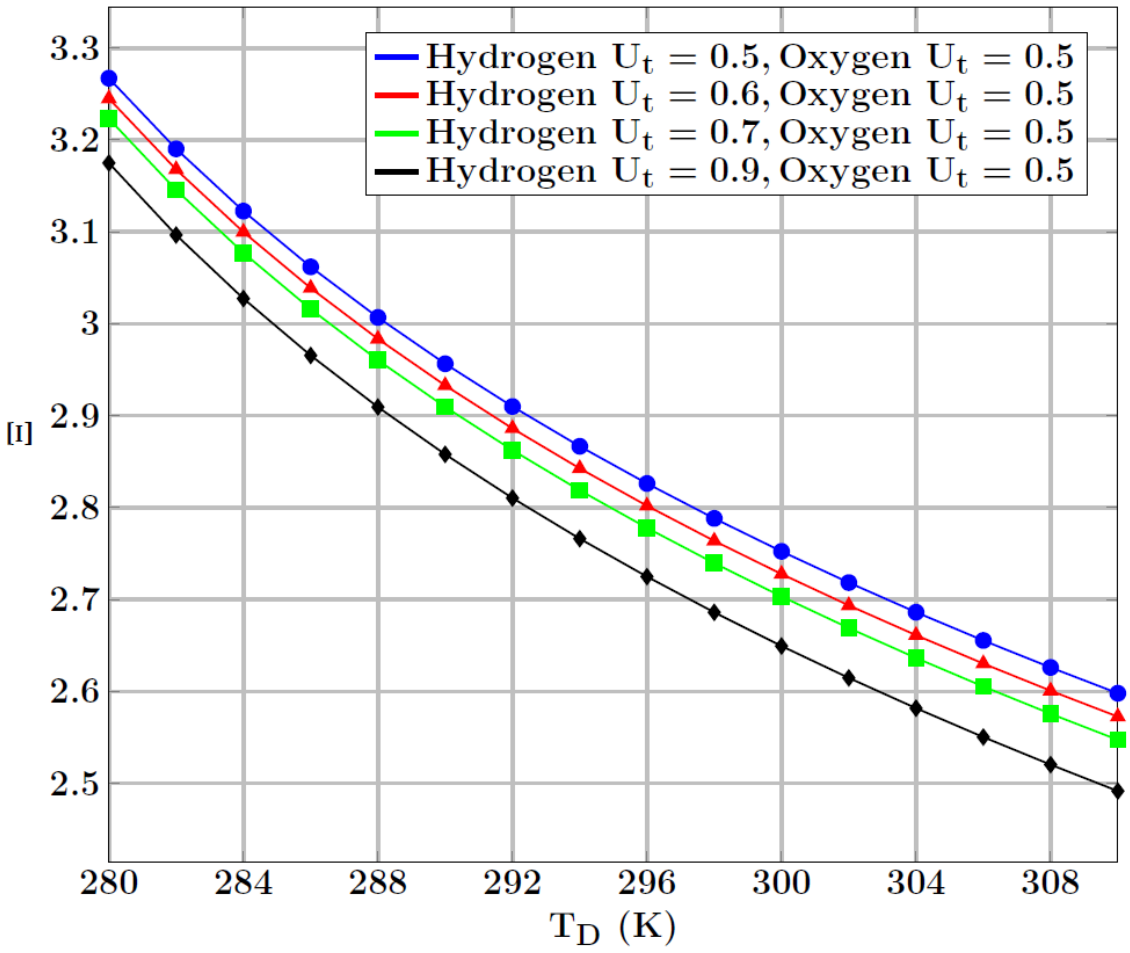

Figure 10.16: Non-dimensionalized dissociation front location in the hydrate layer varying with temperature of dissociation at different operating conditions of the hydrogen (Oxygen utilization=0.5, Case 1).

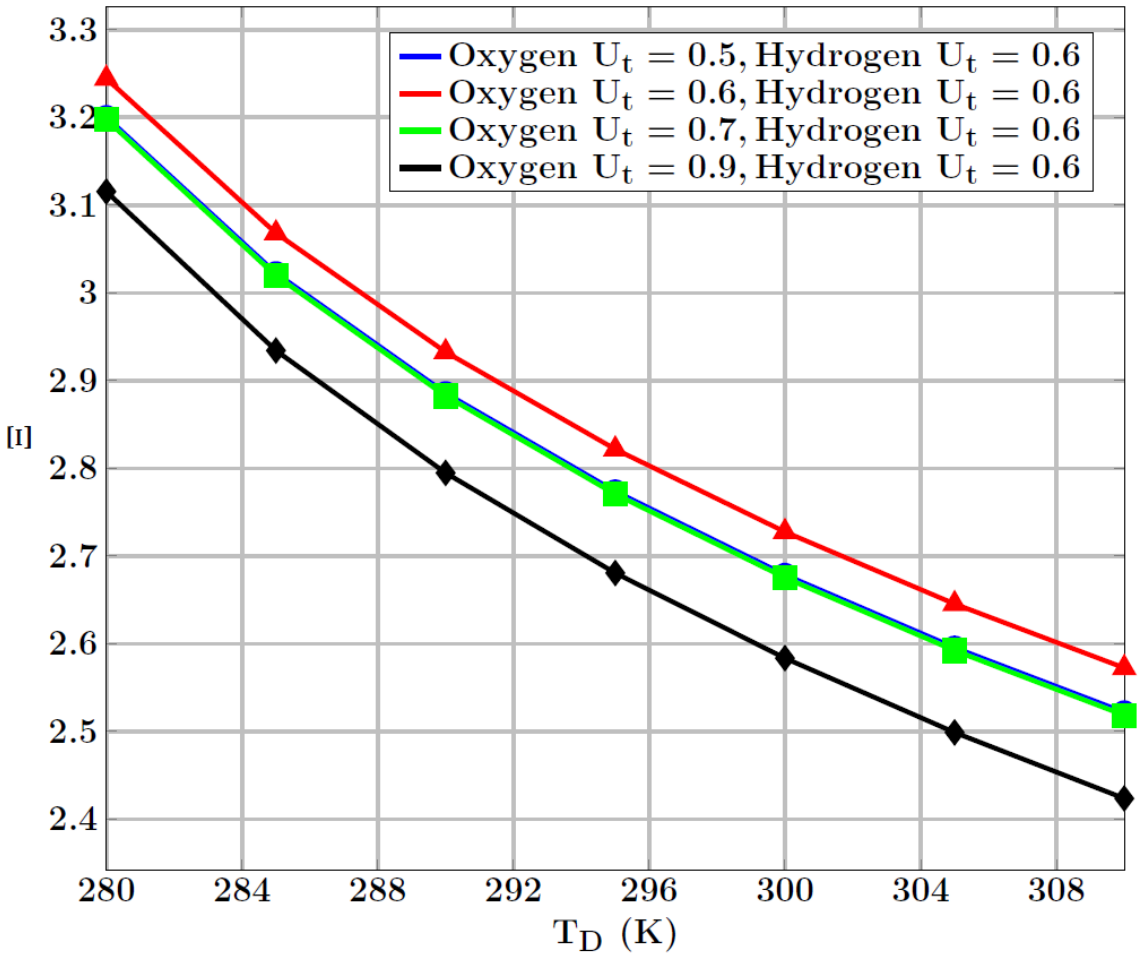

Figure 10.17: Non-dimensionalized dissociation front location in the hydrate layer varying with temperature of dissociation at different operating conditions of the oxygen (Hydrogen utilization=0.6, Case 2)

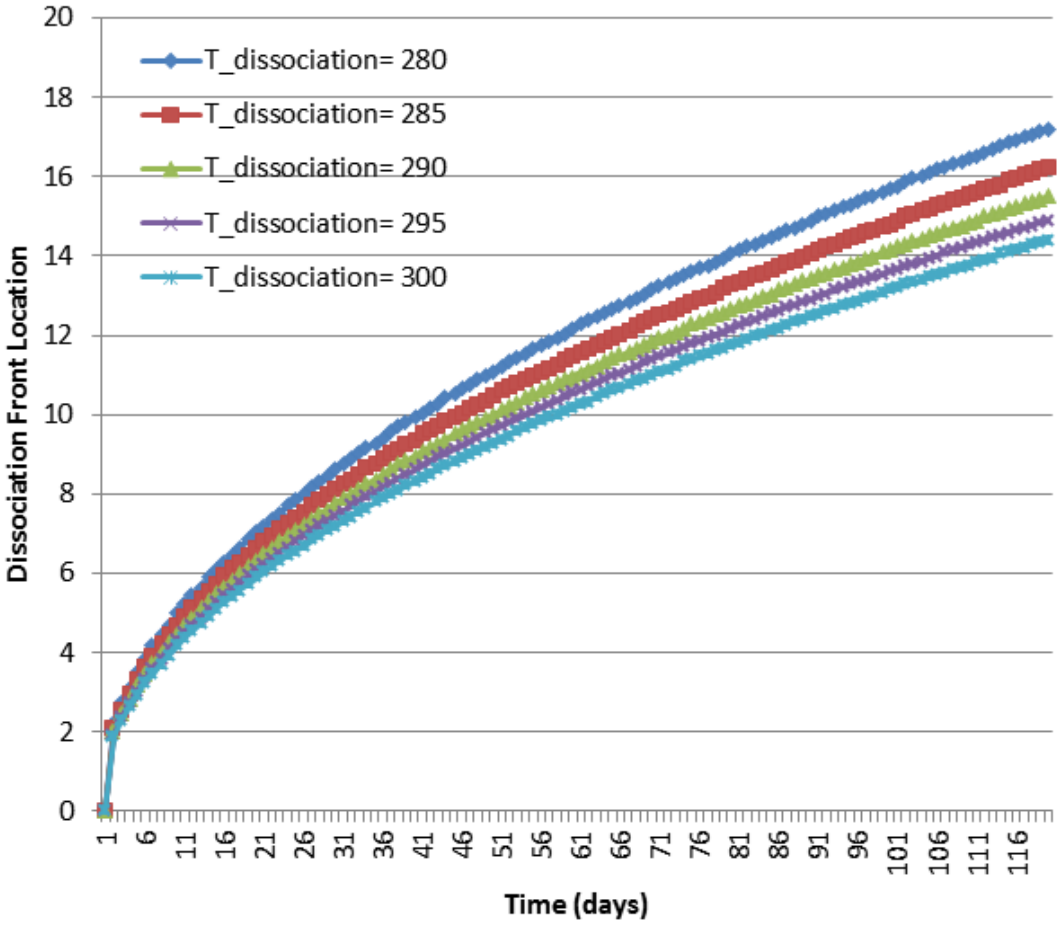

Figure 10.18: Dissociation front location in the hydrate layer varying with temperature of dissociation during the time (hydrogen utilization=0.6)

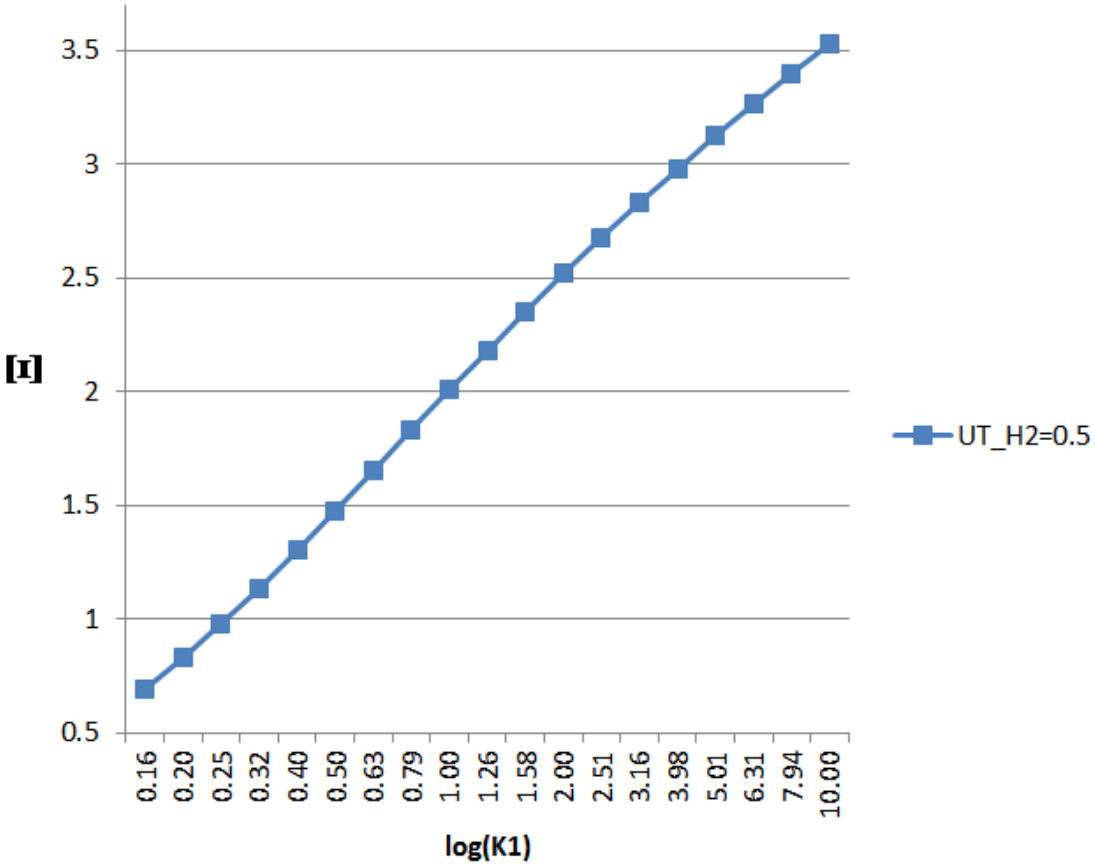

Figure 10.19: Non - dimensionalized dissociation front location in the hydrate layer as a function of thermal conductivity of zone 1(Hydrogen utilization=0.6, Oxygen Utilization= 0.5)

front location in the hydrate layer as a function of thermal conductivity. It should be noted in all these cases the temperature of the hydrate layer is kept at T_i=273 K.

Fig. 10.19 and Fig. 10.20 show the non-dimensioned dissociation front location as a function of the thermal conductivity of the both zones. In Fig. 10.19 the thermal conductivity of the second zone is constant. In Fig. 10.20 the thermal conductivity of the first zone is constant. Increasing k_2 means that the resistance to heat flow is decreased at the hydrate occupied zone (II); therefore, the heat diffusion process is

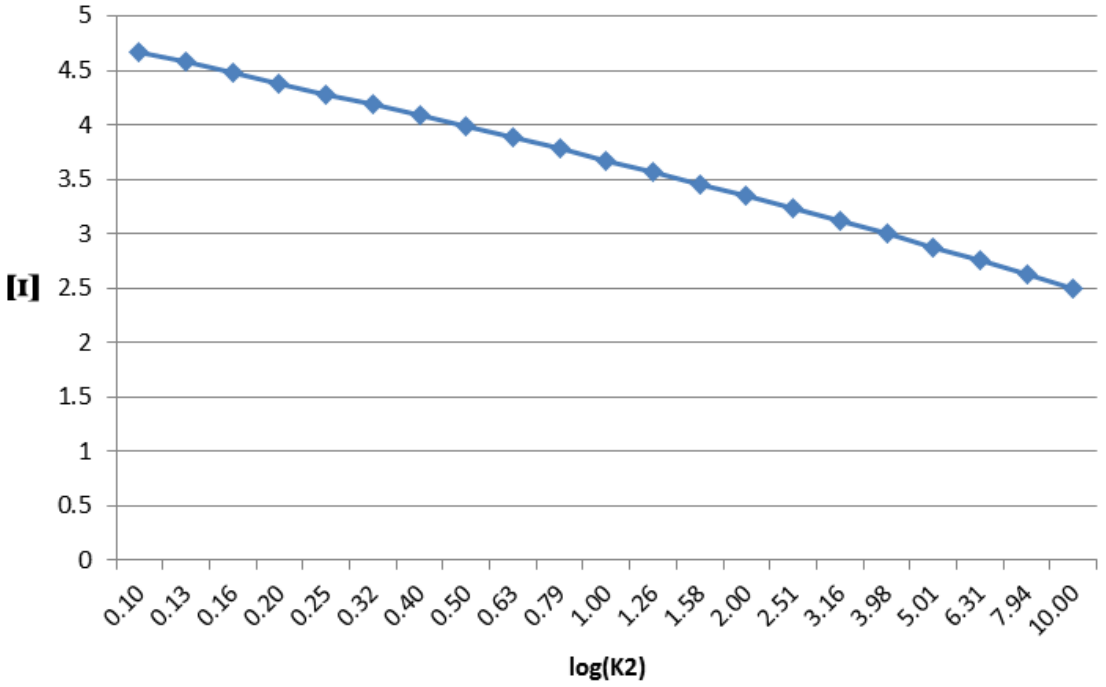

Figure 10.20: Non - dimensionalized dissociation front location in the hydrate layer as a function of thermal conductivity of zone 2 (Hydrogen utilization=0.6, Oxygen Utilization= 0.5)

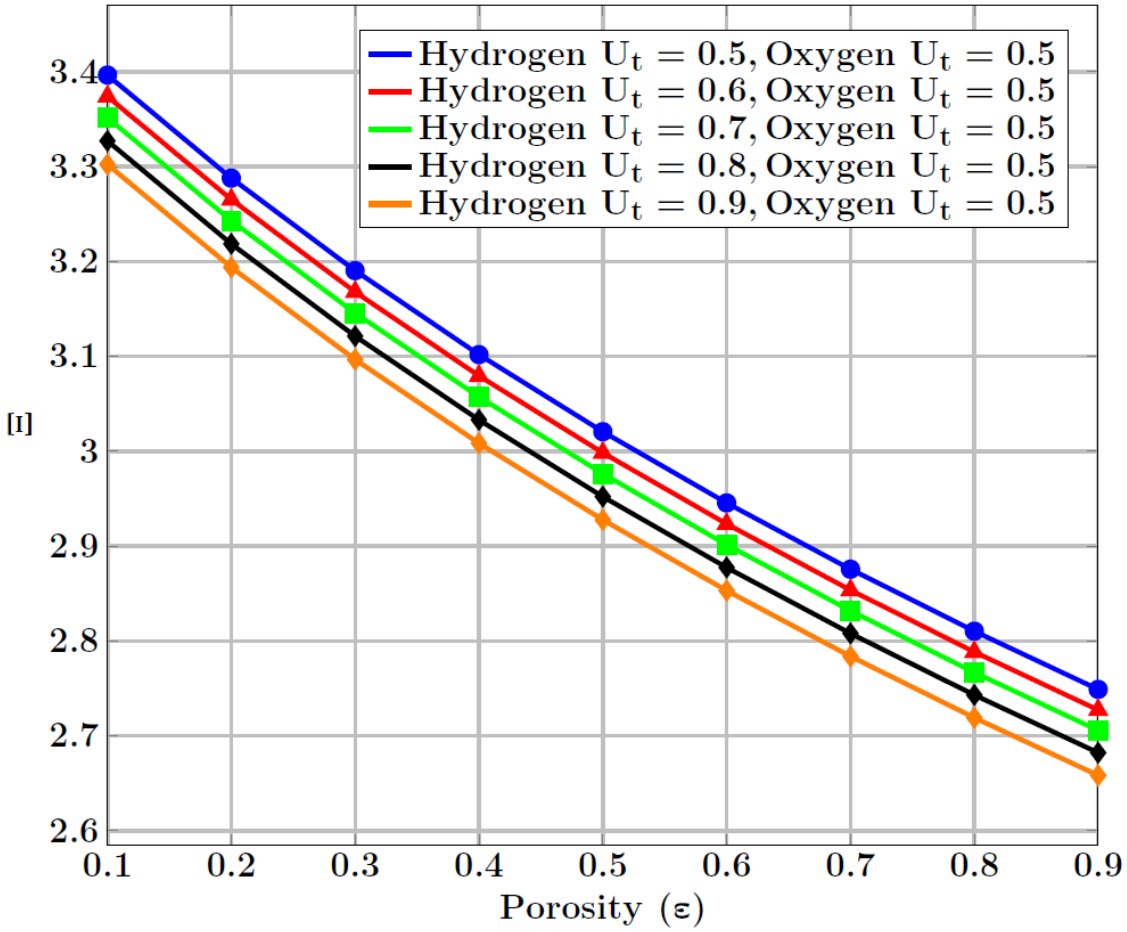

Figure 10.21: Non-dimensionalized dissociation front location in the hydrate layer as a function of thermal conductivity of porosity and hydrogen utilization (Oxygen Utilization= 0.5, Case 1).

easier from the dissociation front so reduces the amount of heat flow that is available for dissociation. As a result, we have lower dissociation rate.

This is different in the case of Fig. 10.18. By increasing the thermal conductivity in the dissociated zone, the heat transfer is faster so the temperature rises faster and reaches the dissociation front. As a result we have a higher dissociation rate.

Fig. 10.21and Fig. 10.22 show the Non - dimensioned dissociation front location in the hydrate layer as a function of porosity and the fuel cell performance. It can

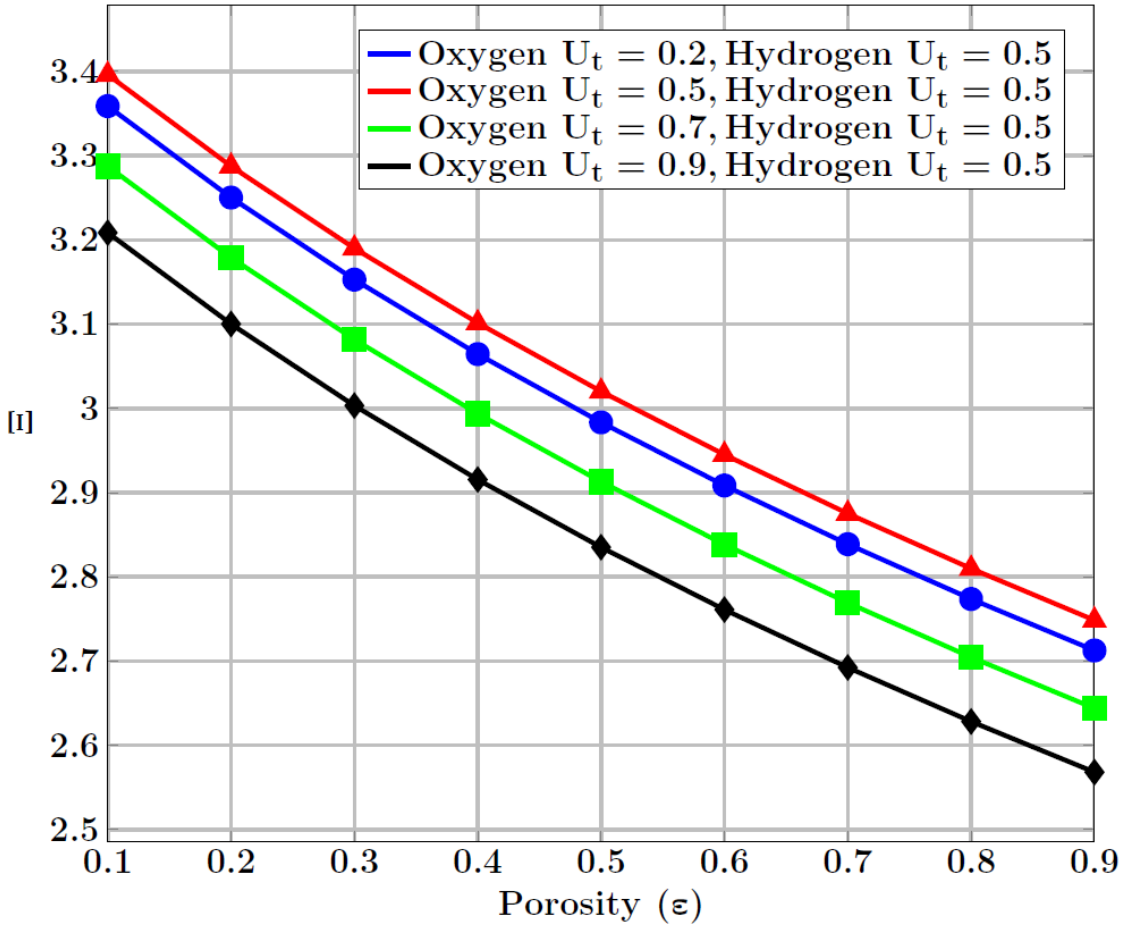

Figure 10.22: Non-dimensionalized dissociation front location in the hydrate layer as a function of thermal conductivity of porosity and hydrogen utilization (Hydrogen Utilization= 0.5, Case 1)

be seen that the hydrogen utilization change has less effect on the ξ parameter, than oxygen utilization does. Increasing the oxygen utilization from 0.2 to 0.9 will reduce the ξ parameter about 0.2. However, Increasing the hydrogen utilization from 0.5 to 0.9 will decrease the parameter by about 0.1.

Fig. 10.23, shows the heat flux to the hydrate layer during the time as a function of hydrogen utilization. Since increasing hydrogen utilization will decrease the temperature of the heat exchanger, it will also reduce the heat flux to the hydrate sediment.

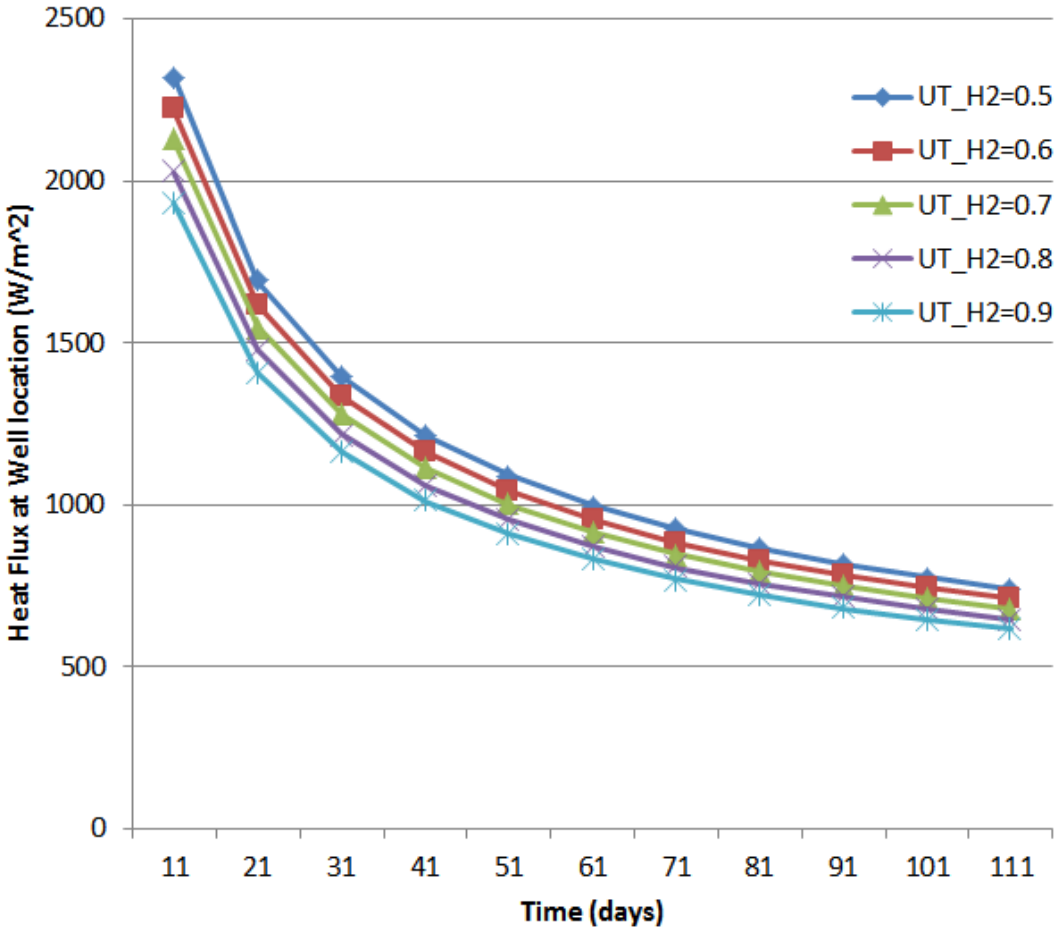

Figure 10.23: The heat flux to the hydrate layer during the time as a function of hydrogen utilization (Oxygen Utilization= 0.5)

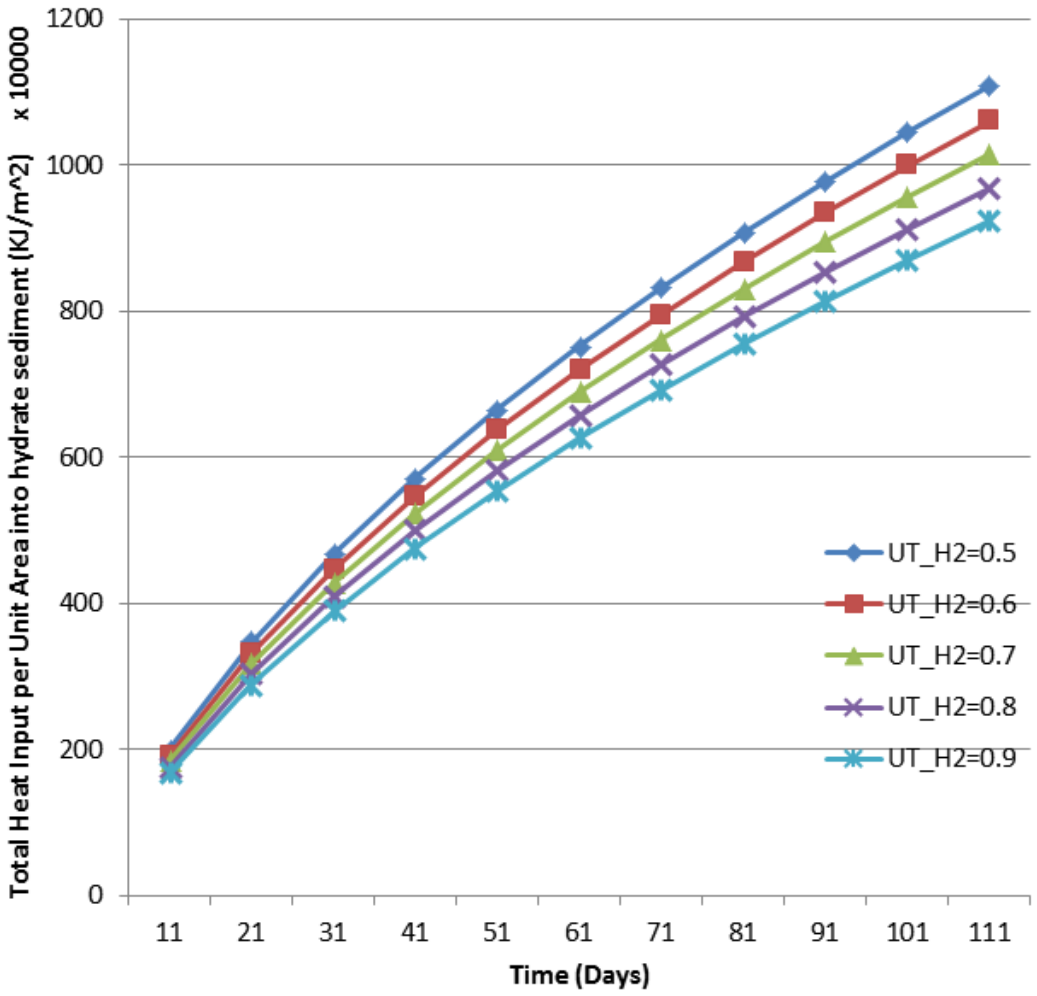

Figure 10.24: The accumulated heat input to the hydrate layer during the time as a function of hydrogen utilization (Oxygen Utilization= 0.5)

Also, it can be observed that the heat flux to the hydrate sediment decreases during the time, and this is because of the fact that as the distance between the un-dissociated hydrate formation and the thermal source will increase as the time passes. Figure 10.24 shows the accumulated total heat input into the hydrate layer.

Fig. 10.27 to 10.31 demonstrate the molar flow of the gases in the steam methane reformer. Lower utilization of hydrogen requires more methane to be converted into

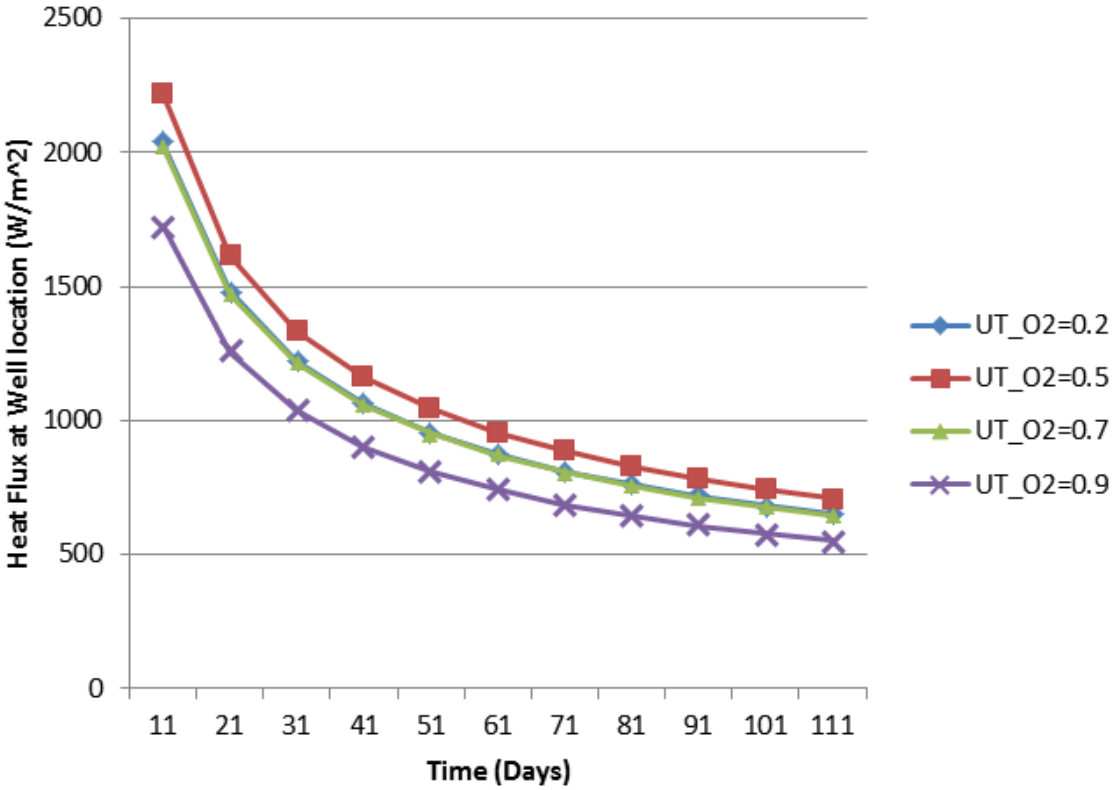

Figure 10.25: The heat flux to the hydrate layer during the time as a function of oxygen utilization (Oxygen Utilization= 0.5)

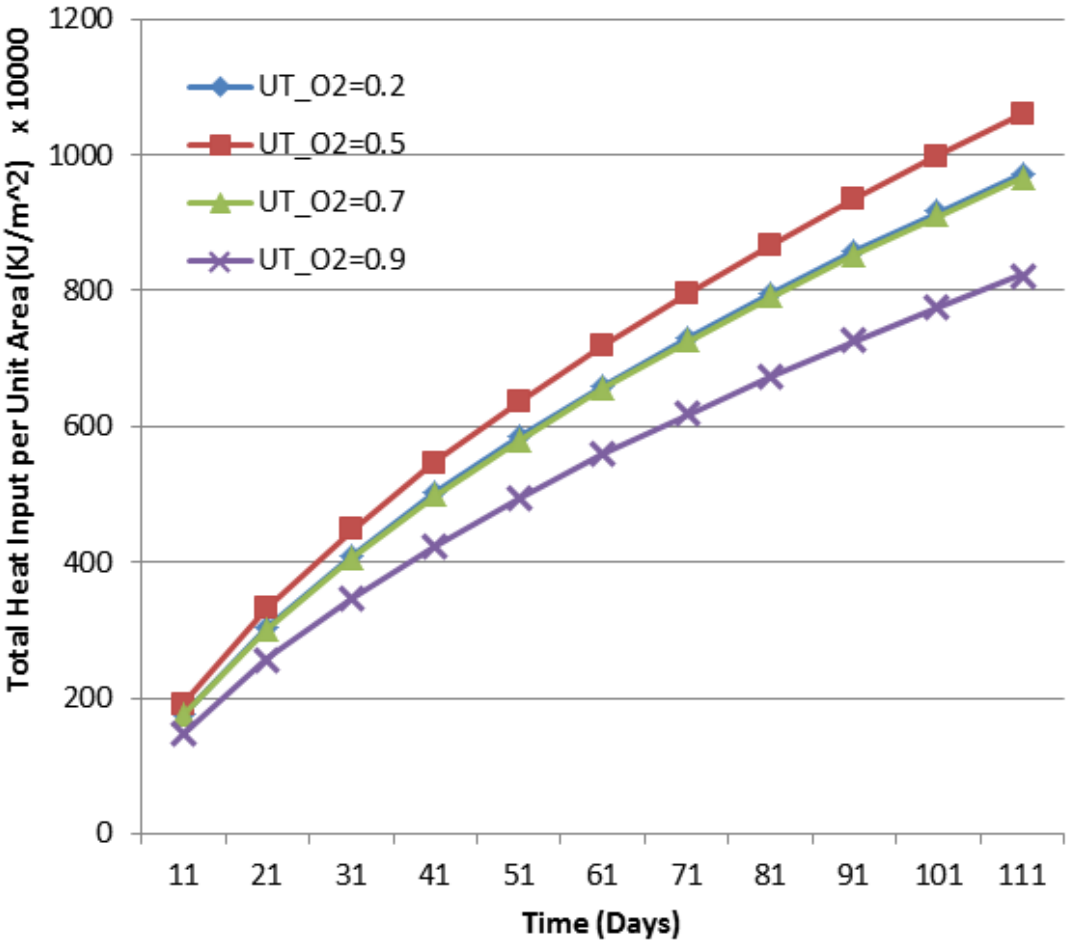

Figure 10.26: The accumulated heat input to the hydrate layer during the time as a function of oxygen utilization (hydrogen Utilization= 0.6)

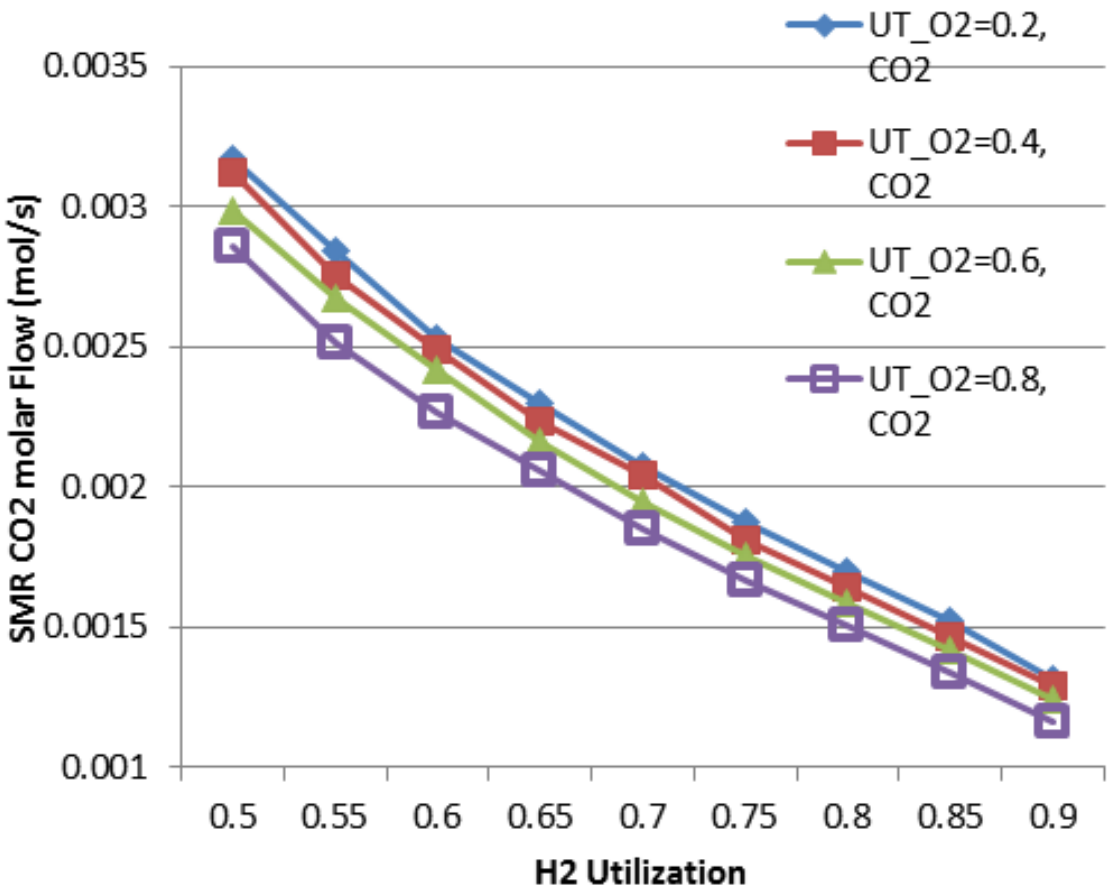

Figure 10.27: Carbon dioxide molar flow in SMR as a function of the hydrogen utilization and oxygen utilization(Target Power=1000W)

hydrogen.

Fig. 10.32 shows the methane mass flow production over time for different power generations of the fuel cell for two different cases: Case 1: Heat of the steam methane reformer is provided by burning the part of the dissociated methane from the hydrate sediment Case 2: Heat of the steam methane reformer is provided by the fuel cell effluent gases In case 1, it is obvious the temperature of the fuel cell effluent gases are higher than case 2, so the mass production of methane is higher in this case because

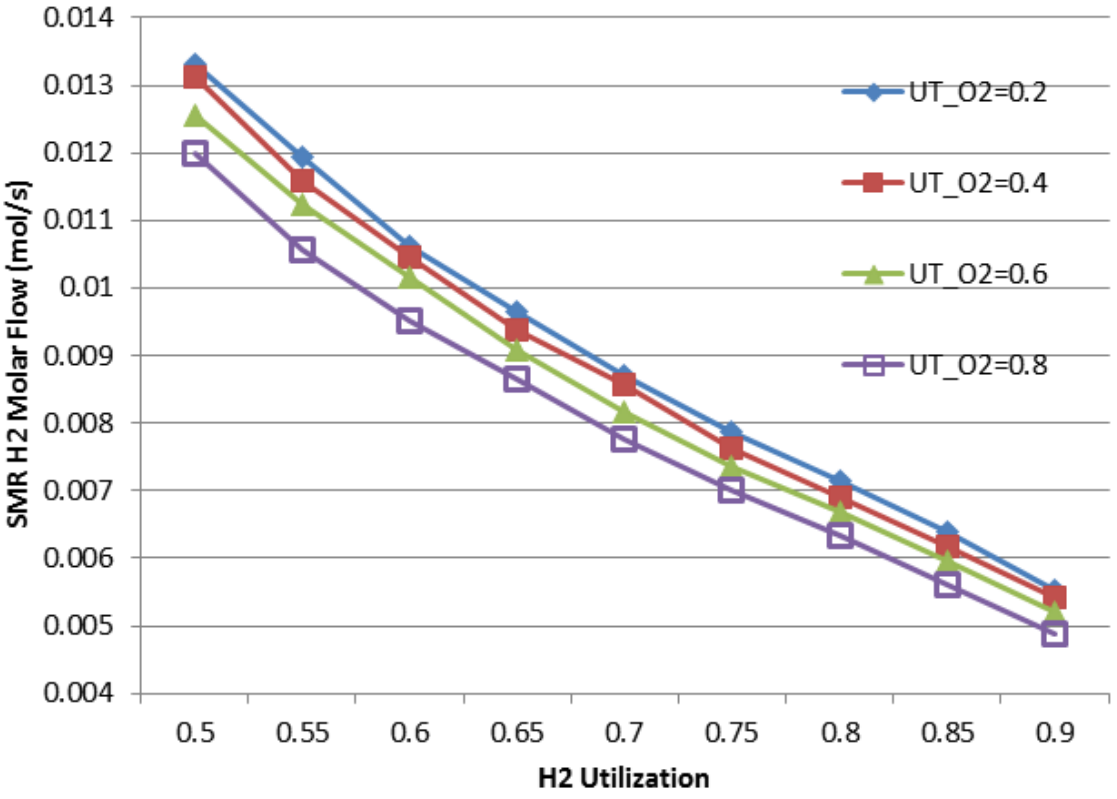

Figure 10.28: Hydrogen molar flow in SMR as a function of the hydrogen utilization and oxygen utilization (Target Power=1000W)

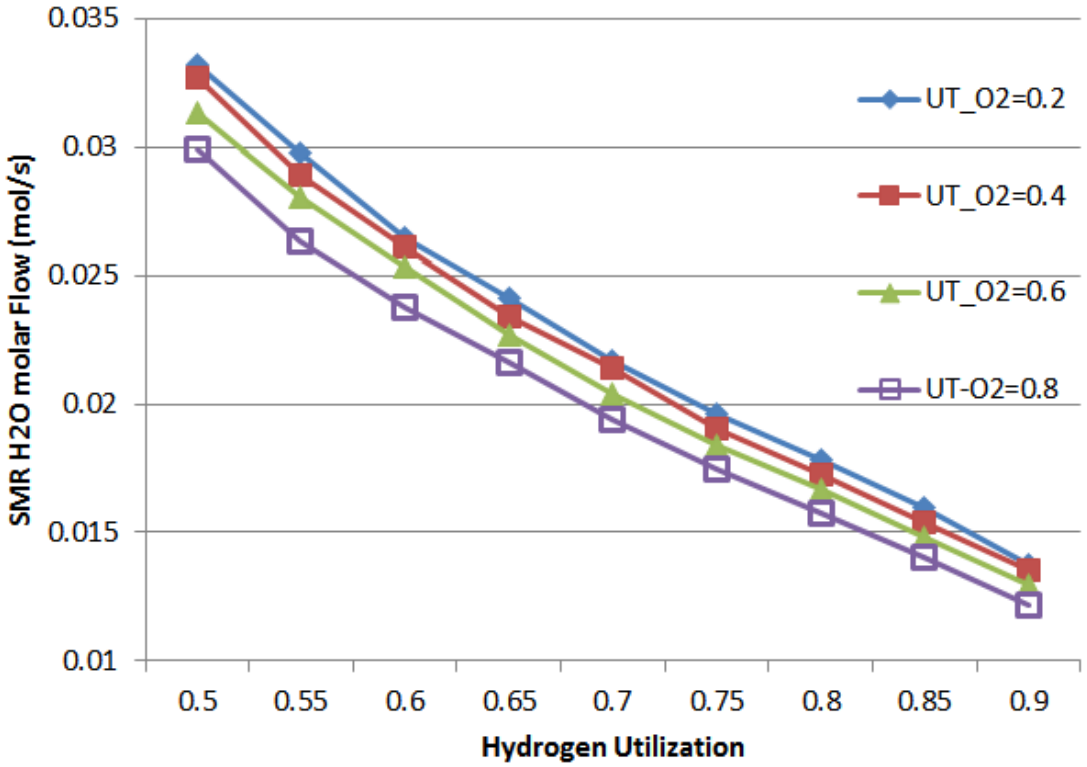

Figure 10.29: H2O molar flow in SMR as a function of the hydrogen utilization and oxygen utilization (Target Power=1000W)

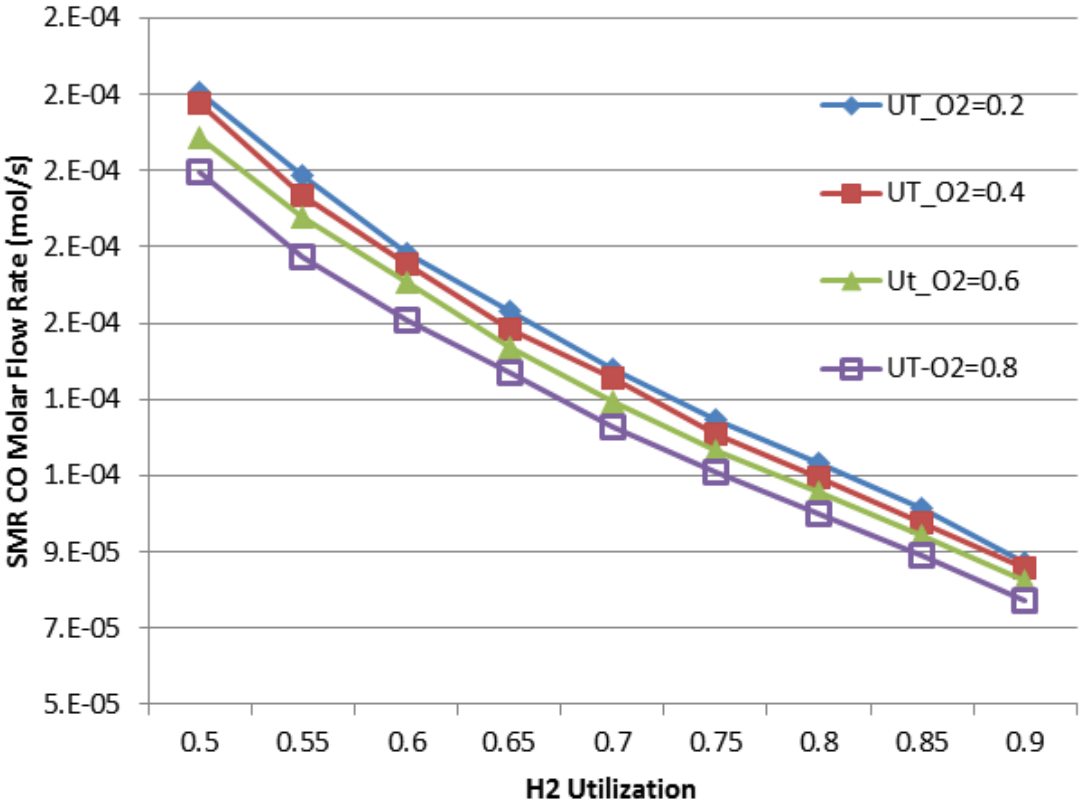

Figure 10.30: Carbon monoxide molar flow in SMR as a function of the hydrogen utilization and oxygen utilization (Target Power=1000W)

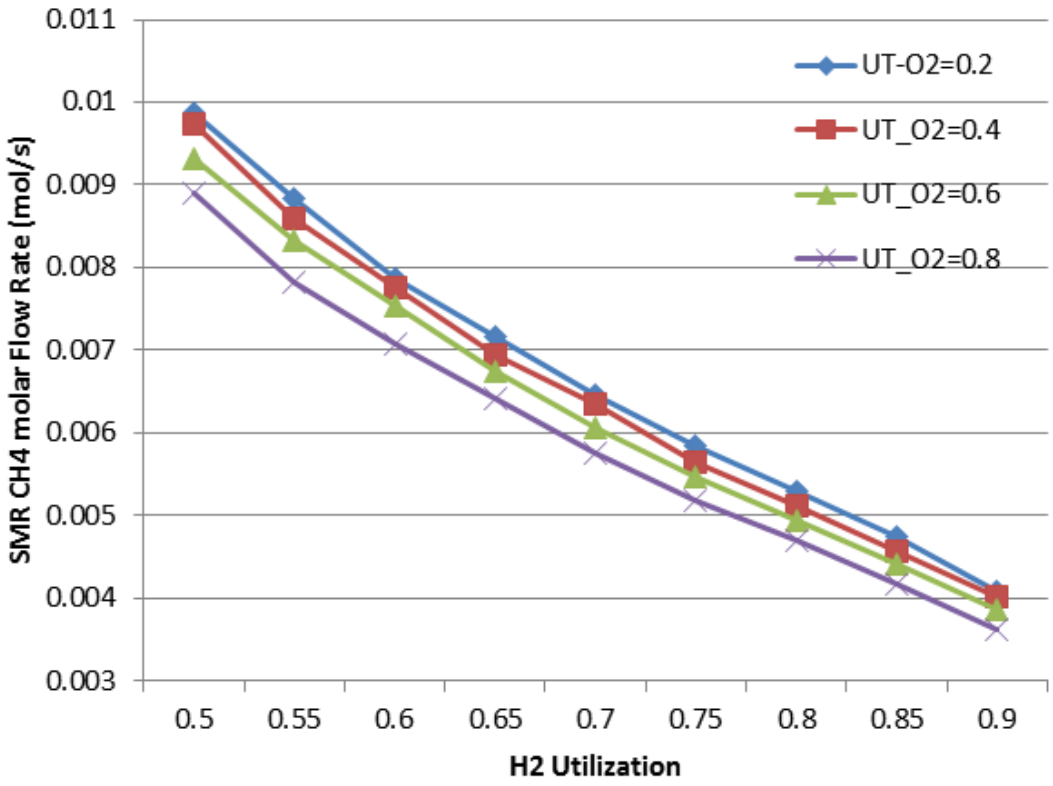

Figure 10.31: Methane molar flow in SMR as a function of the hydrogen utilization and oxygen utilization (Target Power=1000W)

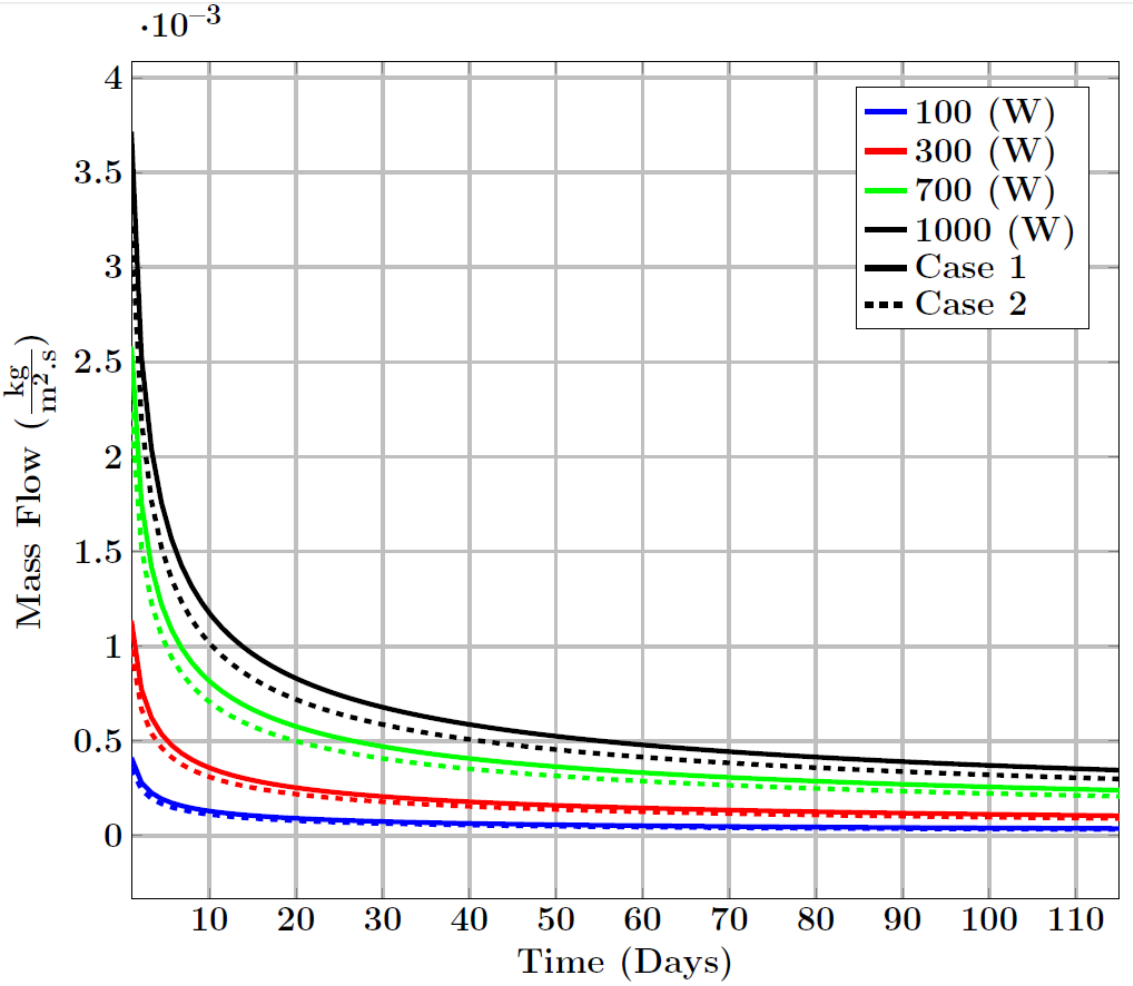

Figure 10.32: Methane gas mass flow production over time (O_2 utilization=0.5, H_2 utilization=0.7).

of higher rate of dissociation.

Fig. 10.33 shows that, the net mass production for case 1 is also higher despite the fact that some of the produced methane are burned to provide the heat for the reformer. This shows that burning methane would be a better choice regarding the net mass production of methane.

Figure 10.34 shows the accumulated mass production of the methane during time. The mass production rate decreases because of the velocity of the dissociation front

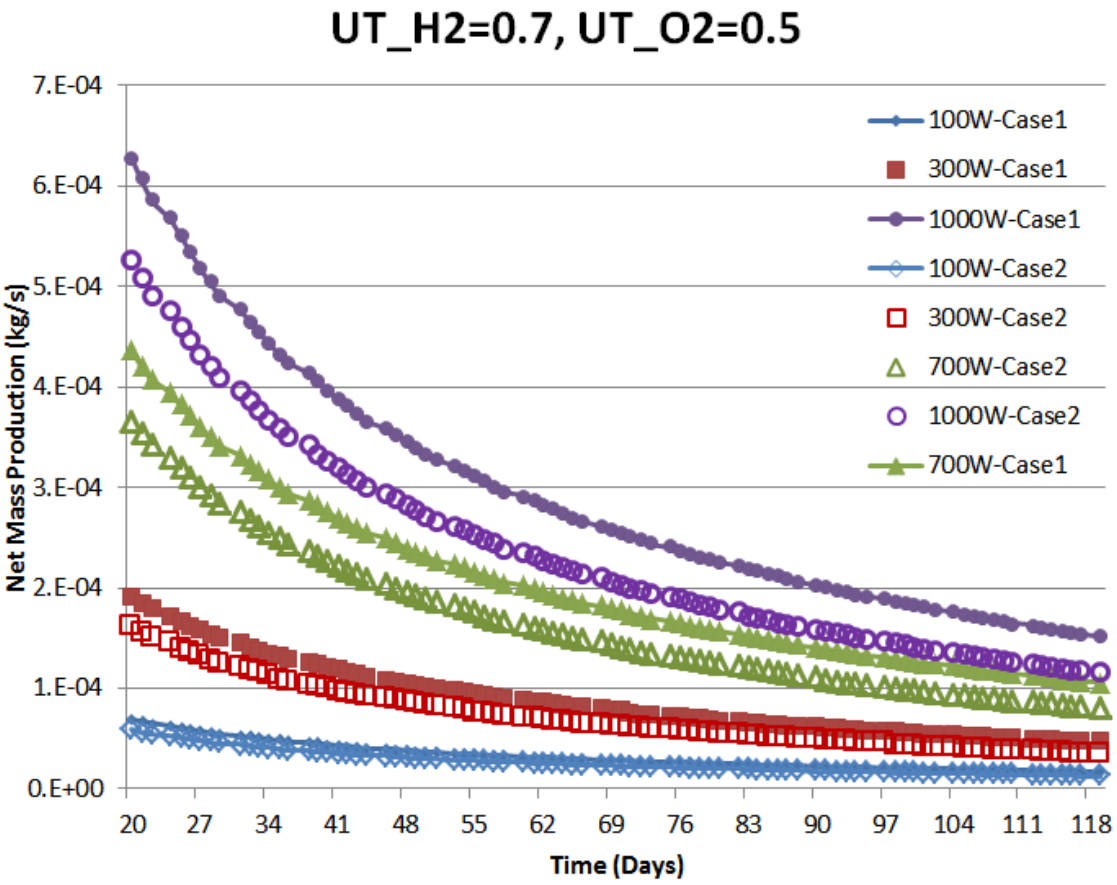

Figure 10.33: Net methane Mass flow production over time (O_2 utilzation=0.5, H_2 utilization=0.7)

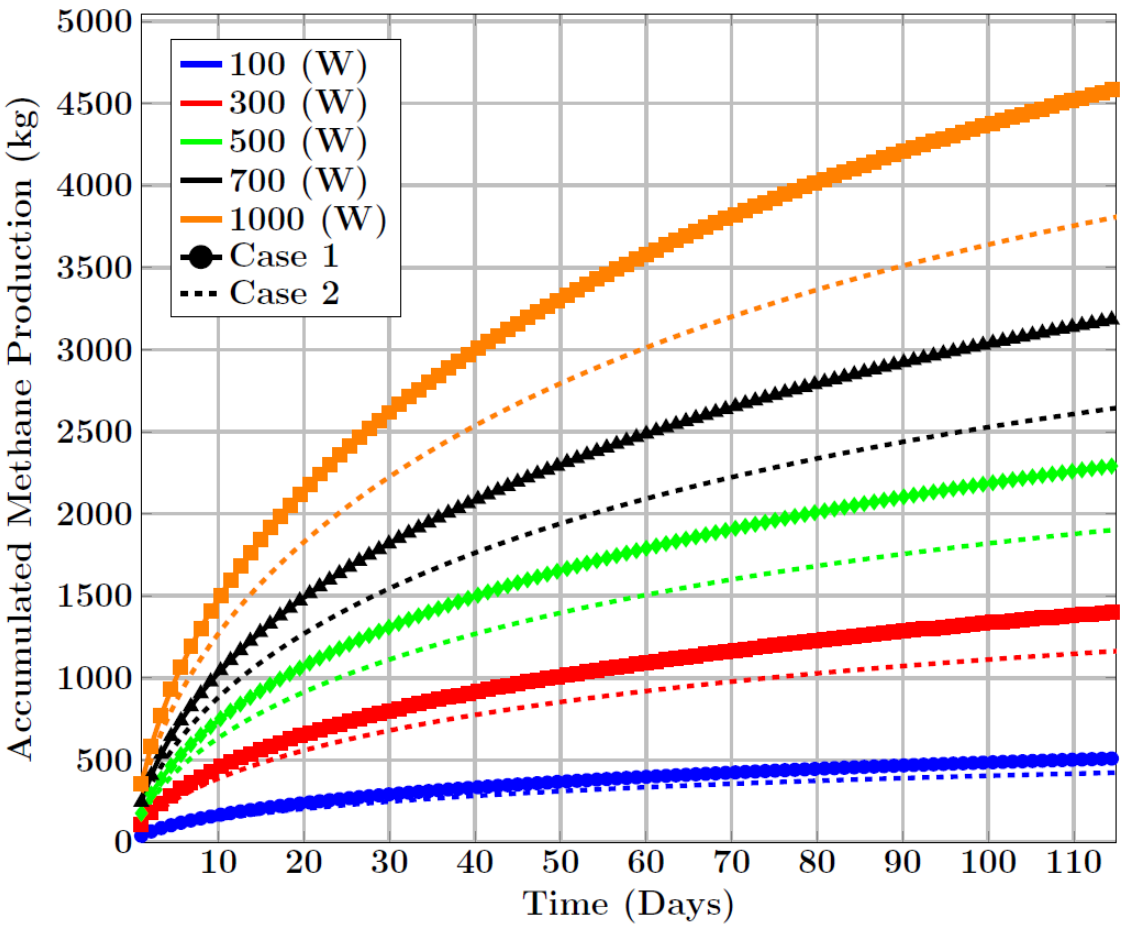

Figure 10.34: Accumulated gas production during time (O_2 utilzation=0.5, H_2 utilization=0.7)

decreases over the long period of time.

Fig. 10.39 shows the maximum amount of power that can be produced by using the depressurization method for different values of hydrogen utilization. If the fuel cell has high hydrogen utilization it generates less power, however, it also consumes less methane to be converted to hydrogen. Fig. 10.39 shows that the net efficiency of fuel cell with higher fuel utilization is bigger than the fuel cell with low utilization, since it consumes less methane in the reformer.

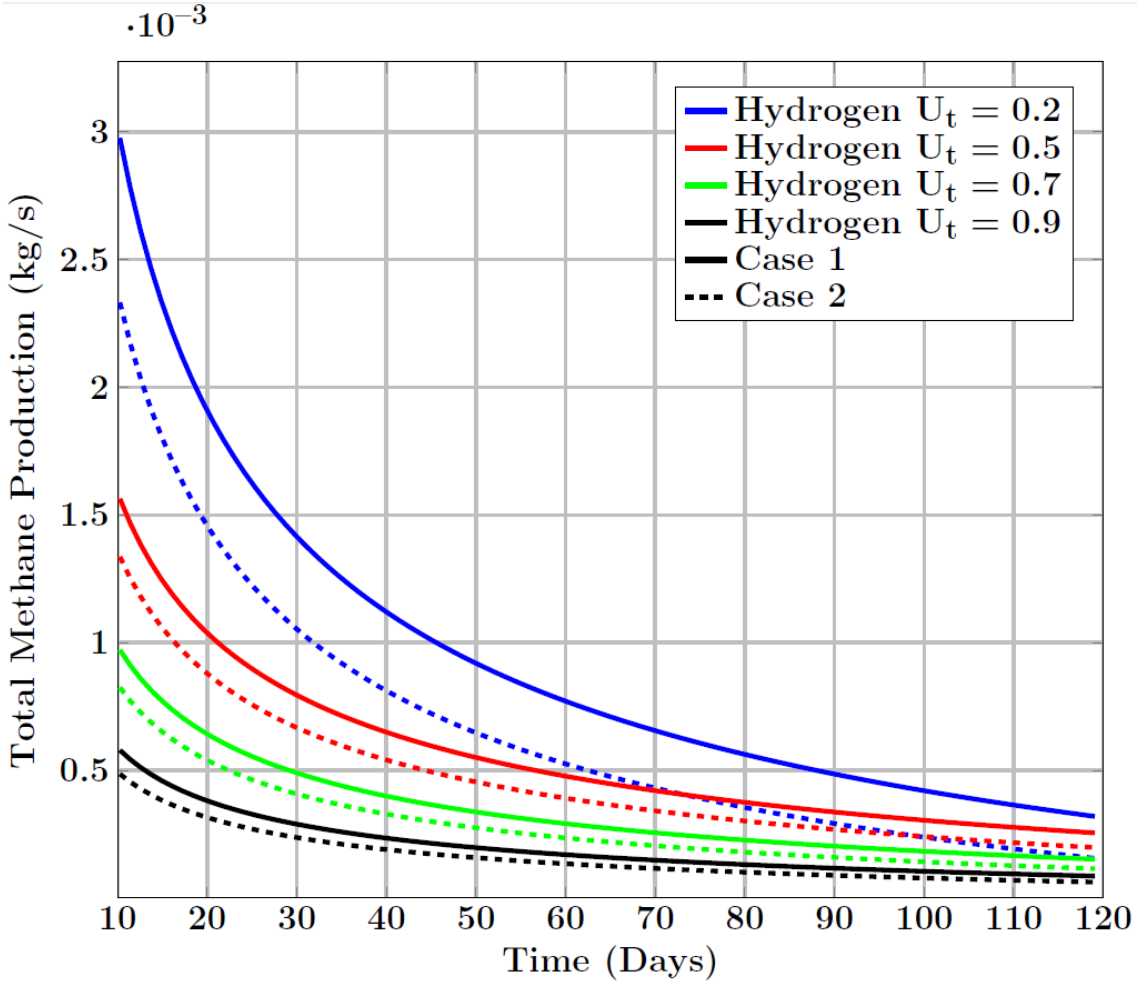

Figure 10.35: Total methane production for different operations of fuel cell (H_2 utilizations), Oxygen utilization=0.5, Produced power=1000W.

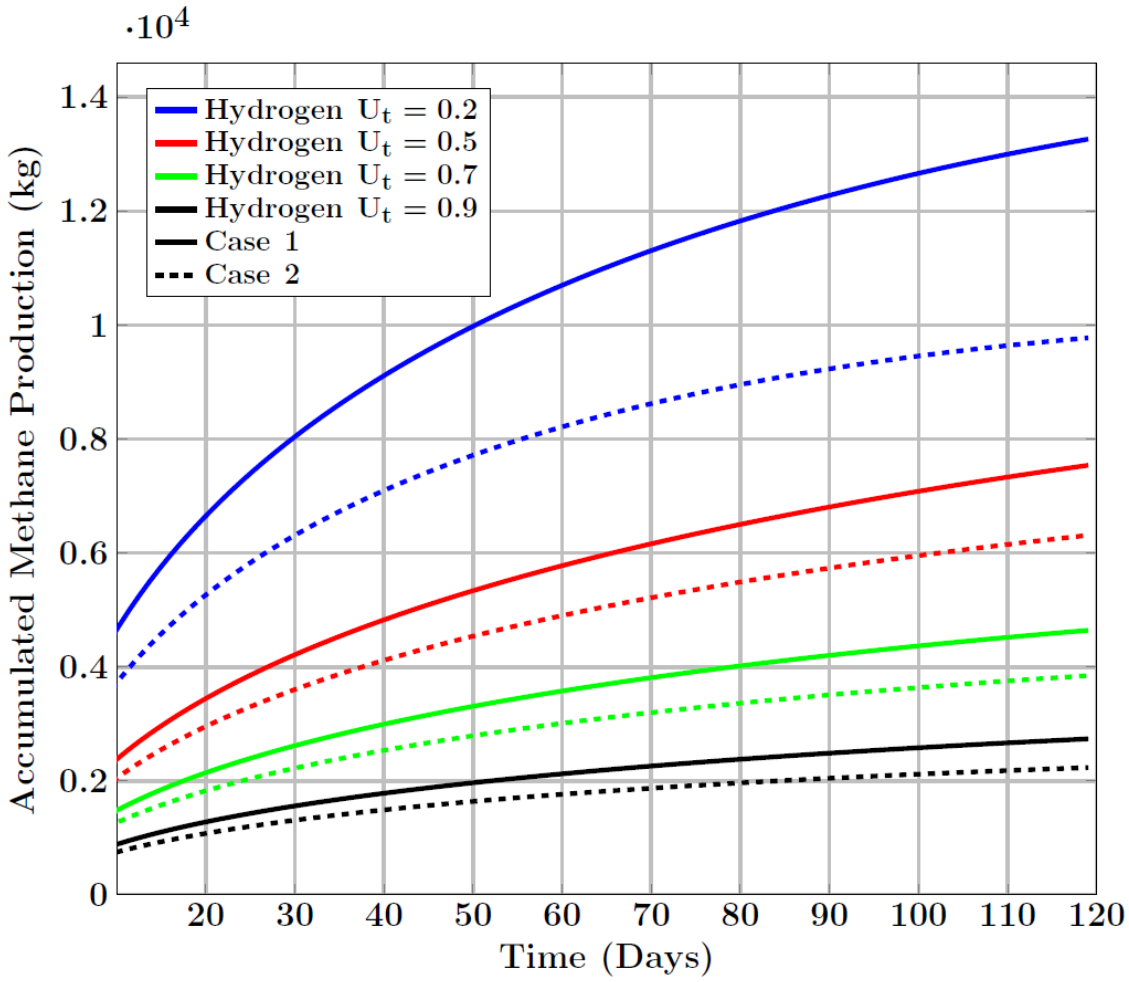

Figure 10.36: Accumulated methane produced over a period of time for different operations of fuel cell (O_2 utilization =0.5), Produced power=1000W

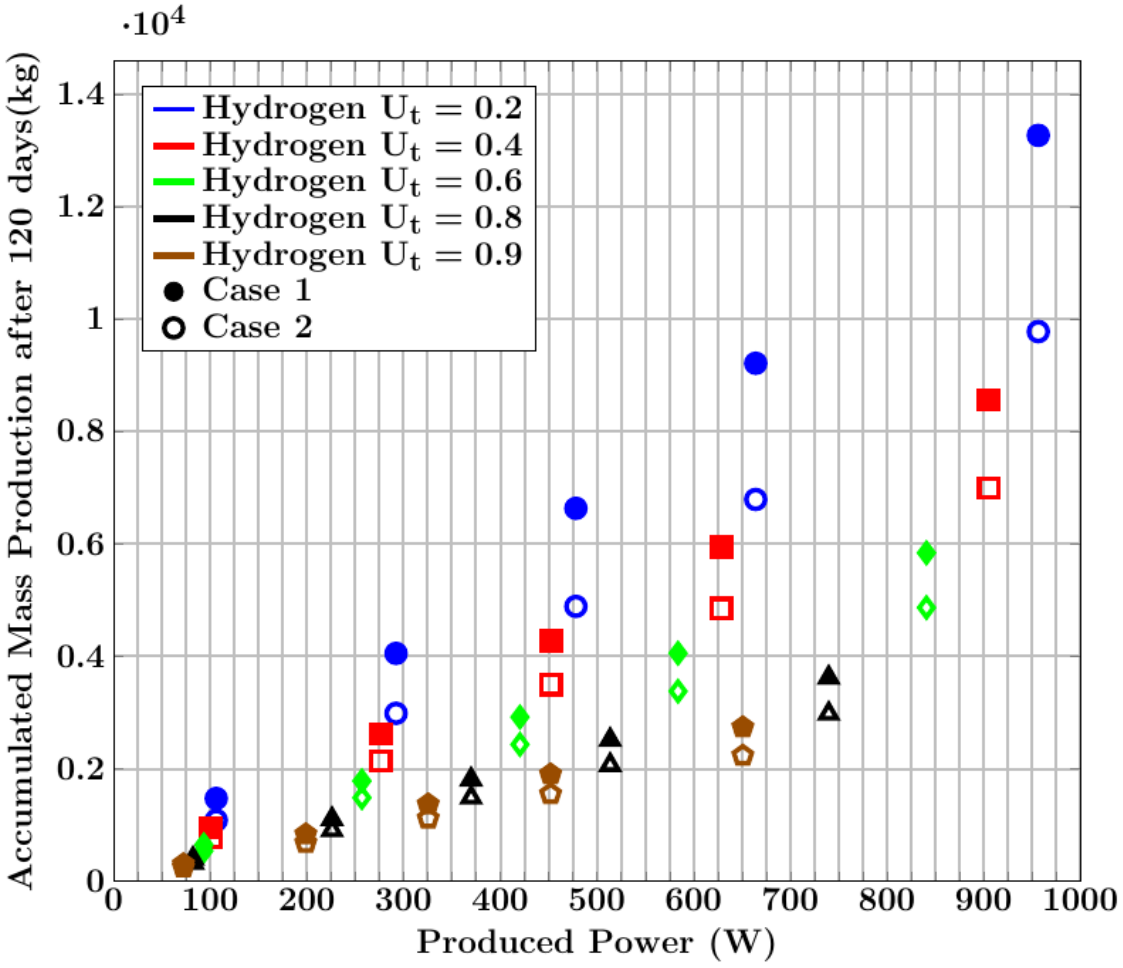

Figure 10.37: Accumulated production of methane after 120 days versus the produced power of fuel cell for different operating conditions of the fuel cell (Constant O_2 utilization= 0.5).

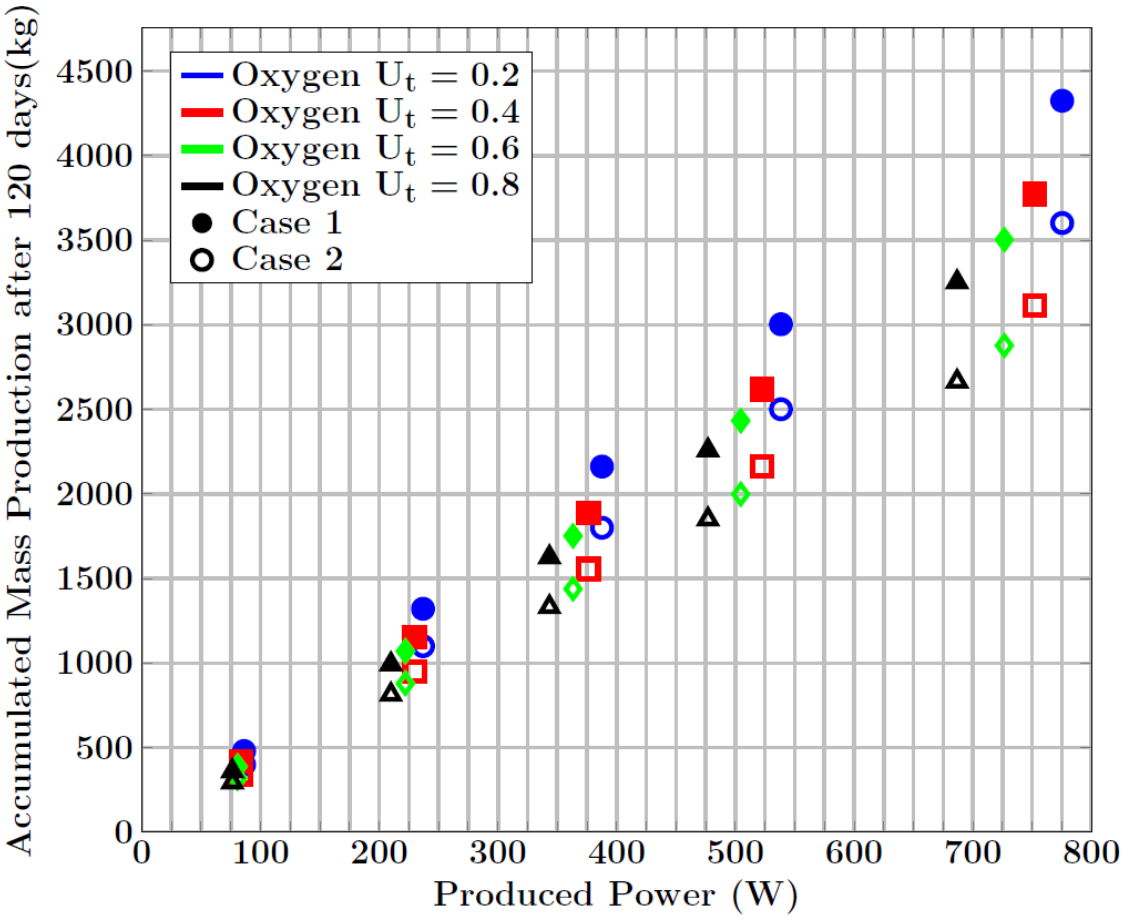

Figure 10.38: Accumulated production of methane after 120 days versus the produced power of fuel cell for different operations of fuel cell (Constant H_2 utilization= 0.8)

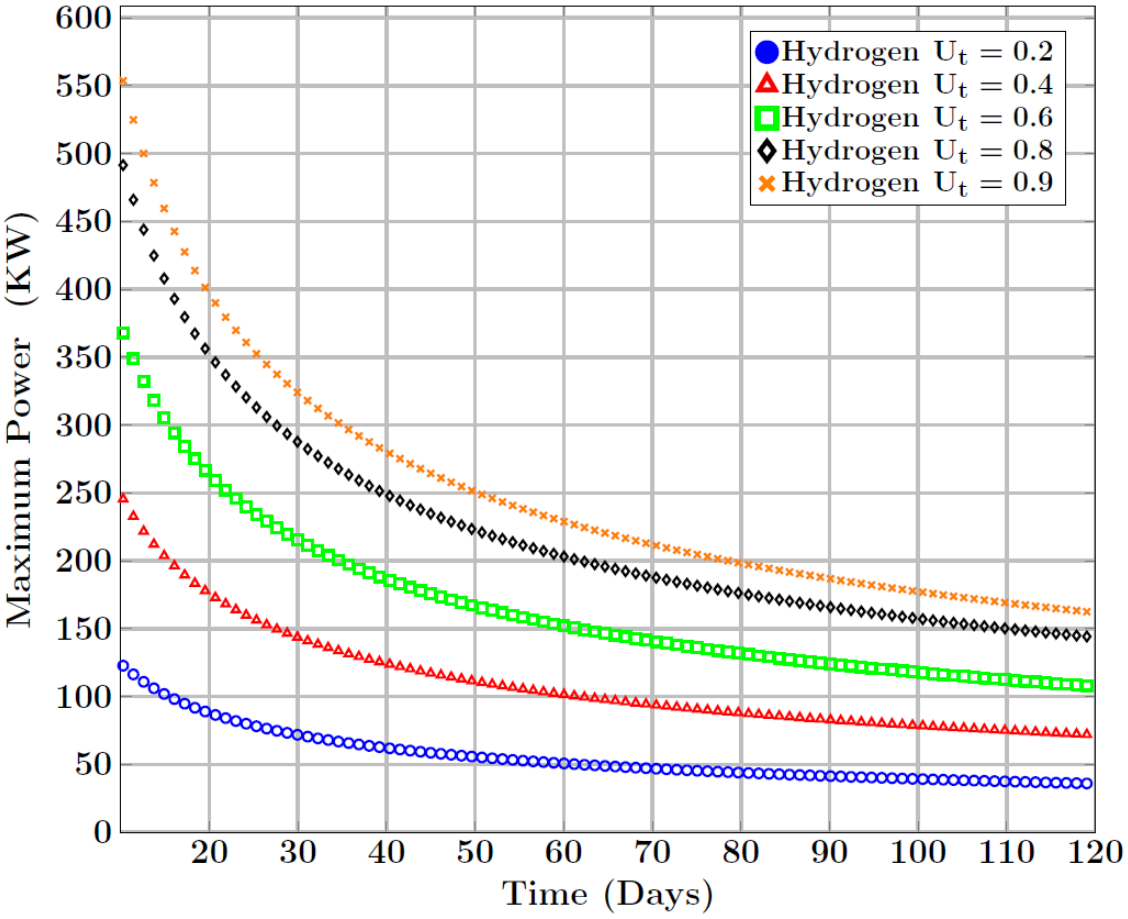

Figure 10.39: Maximum power generation by SOFC based on depressurized hydrate reservoir at constant hydrogen utilization=0.6 and P_W= 4 MPa

10.1 Summary and Conclusions

In this study it is shown that the fuel cell can operate steadily for at least 120 days at the deep ocean environment (e.g., high pressure) regarding the thermodynamics, energy balance, and mass balance principles. The study calculates the accessible net amount of methane production simulated at high pressure environment.

Two different scenarios are compared in this study regarding the heat provision of the steam methane reformer. The first scenario is: providing the heat from burning the part of the dissociated methane from hydrate sediment. The second scenario is to provide the heat from effluent gases of the fuel cell. These two scenarios were compared regarding the net amount of methane production and it is found that the case in which heat is provided by burning some of the dissociated methane produces a larger amount of natural gas. Also, the study evaluated different operational parameters of Solid oxide fuel cell (e.g., reactants utilization), produce methane from hydrate layer.

The other aspect of the study is the maximum power that could be generated by using depressurization. This study showed that despite the fact that low utilization fuel cell produces more power than the fuel cell with higher utilizatio, its net efficiency is less than high utilization SOFC, which is because of the fact that it needs less methane in the reformer.

10.2 Recommendations

The outcome of this research indicates that using high temperature fuel cell (e.g, SOFC) is technically feasible to recover methane gas from methane hydrate sediments. This study also evaluates the synergetic effects of high temperature fuel cell and steam methane reformer at simulated high pressure environment of the deep ocean. Future work could be done on investigation of other types of reformer (e.g Auto thermal reformer (ATR), Parial oxidation (POX) and internal reforming). SOFC was choice of study in this study because of better compatibility with other components of the system regarding the balance of plant. However, It would be useful to evaluate the technical operation of other types of fuel cell such as (Proton Exchange Memberane (PEMFC), Alkaline (AFC)) or other high temperature fuel cells such as Molten Carbonate (MCFC).

Although, this study assumes that there is an abundant amount of oxygen in downhole, there is no feasible and verified technology to provide this amount of oxygen yet. Future research could be an investigation of different methods of oxygen delivery to downhole. Furthermore, the study is using oxygen as an oxidant in SOFC components. Future work could investigate the effects of using Nitrogen on the components of the system. Although, this study proposes the utilization of electrolyzer as a method of oxygen production, it is not thoroughly investigated. Electrolyzers have unique features which makes them feasible to operate in the deep ocean environment.

In addition, this study only verifies that fuel cell operation is feasible from the theoretical point of view. To obtain a valid analysis, experimental studies should be done on the high pressure fuel cells or other components of the system.

Bibliography

[1] Larionova, A. (2014, January 20). BP predicts slowdown in global energy demand. Rerieved from http://www.mrcplast.com/news-news_open-275312.html

[2] Makogon, I. F. (1997). Hydrates of hydrocarbons. Pennwell Books.

[3] Davy, Humphry. "The Bakerian Lecture: On some of the combinations of oxy-muriatic gas and oxygene, and on the chemical relations of these principles, to inflammable bodies." Philosophical Transactions of the Royal Society of London 101 (1811): 1-35.

[4] Wroblewski, S.V. 1882 . Compt. Ren. 94(212):1355.

[5] Villard, P. 1890. Compt. Rend. 111:302

[6] Deaton, W. M., and E. M. Frost Jr. Gas hydrates and their relation to the operation of natural-gas pipe lines. No. BM-Mon-8. Bureau of Mines, Amarillo, TX (USA). Helium Research Center, 1946.

[7] Kobayashi, R., and D.L. Katz. 1949. Methane hydrate at high pressure. Petrol. Trans. AIME 186:66-70

[8] Nikitin, B.A. 1940. Izd. Akad. Nauk SSSR, Otd. Khim. Nauk. 1:39.

[9] von Stackelberg, M., and W. Jahns. 1954. Z. Electrochem. 58:162.

[10] Robinson, d.B., and H.J. Ng. Can. Petrol. Tech., 26, July-August.

[11] Makogon, Y.F., V.I. Tsarev, and N.V. Cherskiy, 1972a. Formation of large natural gas fields in zones of permanently low temperature. Doklady Academii Nauk SSSR. 205:700-703.

[12] Miller, S.L, 1969. Clathrate hydrates of air in Antractic ice, Science, 165:489.

[13] Strizhov, I.N., and I.E. Khodanivich. 1946. Gas production. Gostoptekhizdat. Moscow.

[14] Trofimuk, A. A., N. V. Cherskiy, and V. P. Tsarev. "The gas-hydrate sources of hydrocarbons." Priroda 1 (1979): 18-27.

[15] McIver, 1981 R.D. McIver, Gas hydrates,R.F. Meyer, J.C. Olson (Eds.), Long-Term Energy Resources, Vol. 1Pitman, Boston, Mass (1981), pp. 713726

[16] Makogon,Y.F. 1984. "Perspectives for the oil and gas industry in the world. Gazovaya Promishlennost (Gas Industry)",n.8. Moscow

[17] Makogon, Y. F. "Razrabotka gazogidratnoy zalezhi (Production from natural gas hydrate deposits): Gazovaya Promishlennost, v. 10." (1984): 24-26.

[18] Williams MC, Strakey J, Sudoval W. U.S. DOE fossil energy fuel cells program. Journal of Power Sources. 2006;159:1241-7.

[19] Makogon, Y.F. 1965 Hydrate formation in gas-bearing layer in permafrost conditions. Gazovaya Promyshelennost (Gas Industry) 5:14-15. Moscow.

[20] NETL. Energy Resource Potential of Methane Hydrate, An Introduction to the Science and Energy Potential of a Unique Resource. National Energy Technolgoy Laboratory; 2011.

[21] Dunn-Rankin D. W.M. Keck Foundation Deep Ocean Power Science Laboratory. University of California, Irvine; 2011.

[22] Schoderbek D. ConocoPhillips Gas Hydrate Production Test, Semi-Annual Progress Report, First Half, 2012. DOE Award No: DE-NT00065532012.

[23] Santamarina. Hydrate-Bearing Clayey Sediments: Morphology, Physical Properties, Production and Engineering/Geological Implications. Quarterly Research Performance Progress Report (Period ending 3/31/2013) DOE Award No: DE-FE0009897: Georgia Institute of Technology; 2013.

[24] Santamarina. Hydrate-Bearing Clayey Sediments: Morphology, Physical Properties, Production and Engineering/Geological Implications. Quarterly Research Performance Progress Report (Period ending 12/31/2012)). DOE Award No: DE-FE0009897: Georgia Institute of Technology; 2013.

[25] Kang SP, Lee H, Lee CS, Sung WM. Hydrate phase equilibria of the guest mixtures containing CO_2, N_2 and tetrahydrofuran. Fluid Phase Equilibria. 2001;185:101-9.

[26] Vancleeff A, Diepen GAM. Gas Hydrates of Nitrogen and Oxygen. Recueil Des Travaux Chimiques Des Pays-Bas-Journal of the Royal Netherlands Chemical Society. 1960;79:582-6.

[27] Pfefferle WC. Method of natural gas production. US Patent No 6,973,968 13 2005.

[28] Freifeld B. The U-tube: A New Paradigm for Borehole Fluid Sampling. Scientific Drilling. 2009;8:41-5.

[29] Boswell R, Collett T, McConnell D, Frye M, Shedd B, Mrozewski S, et al. Joint Industry Project Leg II discovers rich gas hydrate accumulations in sand reservoirs in the Gulf of Mexico. Fire in the Ice, US Department of Energy, Office of Fossil Energy, National Energy Technology Laboratory. 2009;9:1-5.

[30] Alp D, Parlaktuna M, Moridis GJ. Gas production by depressurization from hypothetical Class 1G and Class 1W hydrate reservoirs. Energy Conversion and Management. 2007;48:1864-79.

[31] Gupta A, Kneafsey TJ, Moridis GJ, Seol Y, Kowalsky MB, Sloan ED. Composite thermal conductivity in a large heterogeneous porous methane hydrate sample. Journal of Physical Chemistry B. 2006;110:16384-92.

[32] Moridis, George J., et al. "Numerical studies of gas production from several CH4 hydrate zones at the Mallik site, Mackenzie Delta, Canada." Journal of Petroleum Science and Engineering 43.3 (2004): 219-238.

[33] Santamarina JC, Tsouris C. Methane Recovery from Hydrate-bearing Sediments, Final Scientific/Technical Report. DOE Award No:DE-FC26-06NT42963: Georgia Institute of Technology; 2011.

[34] Bhangale A, Zhu T, McGrail B, White M. A model to predict hydrate equilibrium and hydrate saturation inside porous media including mixed CH4-CO2 hydrates. Proceedings of the SPE-Improved Oil Recovery Symposium. 2006:paper SPE 99759.

[35] Phale H, Zhu T, White M, McGrail B. Simulation Study on Injection of CO2-microemulsion for Methane Recovery from Gas-Hydrate Reservoirs. Proceedings of the SPE-Improved Oil Recovery Symposium. 2006: paper SPE 100541.

[36] Chatterjee S, Dickens GR, Bhatnagar G, Chapman WG, Dugan B, Snyder GT, et al. Pore water sulfate, alkalinity, and carbon isotope profiles in shallow sediment above marine gas hydrate systems: A numerical modeling perspective. Journal of Geophysical Research-Solid Earth. 2011;116.

[37] Tishchenko, Pavel, et al. "Calculation of the stability and solubility of methane hydrate in seawater." Chemical geology 219.1 (2005): 37-52.

[38] Handa, Y. Paul. "Effect of hydrostatic pressure and salinity on the stability of gas hydrates." Journal of Physical Chemistry 94.6 (1990): 2652-2657.

[39] Sloan, E.D., 1998. Clathrate Hydrates of Natural Gases. Marcel Dekker, Inc., New York.

[40] Duan, Zhenhao, Nancy Mller, and John H. Weare. "An equation of state for the CH4-CO2-H2O system: I. Pure systems from 0 to 1000 C and 0 to 8000 bar." Geochimica et Cosmochimica Acta 56.7 (1992): 2605-2617.

[41] Duan, Zhenhao, et al. "The prediction of methane solubility in natural waters to high ionic strength from 0 to 250 C and from 0 to 1600 bar." Geochimica et Cosmochimica Acta 56.4 (1992): 1451-1460.

[42] Duan, Zhenhao, and Shide Mao. "A thermodynamic model for calculating methane solubility, density and gas phase composition of methane-bearing aqueous fluids from 273 to 523K and from 1 to 2000bar." Geochimica et Cosmochimica Acta 70.13 (2006): 3369-3386.

[43] Leifer, Ira, and Ian MacDonald. "Dynamics of the gas flux from shallow gas hydrate deposits: interaction between oily hydrate bubbles and the oceanic environment." Earth and Planetary Science Letters 210.3 (2003): 411-424.

[44] MacDonald, I. R., N. L. Guinasso, R. Sassen, J. M. Brooks, L. Lee, and K. T. Scott. "Gas hydrate that breaches the sea floor on the continental slope of the Gulf of Mexico." Geology 22, no. 8 (1994): 699-702.

[45] Torres, M. E., et al. "Fluid and chemical fluxes in and out of sediments hosting methane hydrate deposits on Hydrate Ridge, OR, I: Hydrological provinces." Earth and Planetary Science Letters 201.3 (2002): 525-540.

[46] Tsimpanogiannis, Ioannis N., and Peter C. Lichtner. "Parametric study of methane hydrate dissociation in oceanic sediments driven by thermal stimulation." Journal of Petroleum Science and Engineering 56.1 (2007): 165-175.

[47] Hyndman, R. D., et al. "Geophysical studies of marine gas hydrate in northern Cascadia." Natural gas hydrates (2001): 273-295.

[48] Makogan, Y.F., Holditch, S.A., Makogan, T.Y., 2005. Russian field illustrates gashydrate production. Oil Gas

[49] Collett, T. S., et al. "Detailed evaluation of gas hydrate reservoir properties using JAPEX/JNOC/GSC Mallik 2L-38 gas hydrate research well downhole well-log displays." BULLETIN-GEOLOGICAL SURVEY OF CANADA (1999): 295-312.

[50] Swinkels, Wim JAM, and Rik JJ Drenth. "Thermal reservoir simulation model of production from naturally occurring gas hydrate accumulations." SPE Reservoir Evaluation & Engineering 3.06 (2000): 559-566.

[51] Yousif, M.H., Sloan, E.D., 1991. Experimental investigation of hydrate formation and dissociation in consolidated porous media. SPE Reserv. Eng. 6, 452458.

[52] Yousif, M.H., Abass, H.H., Selim, M.S., Sloan, E.D., 1991. Experimental and theoretical investigation of methanegashydrate dissociation

[53] Goel, Naval, Michael Wiggins, and Subhash Shah. "Analytical modeling of gas recovery from in situ hydrates dissociation." Journal of Petroleum Science and Engineering 29.2 (2001): 115-127.

[54] Khataniar, Santanu, et al. "Modelling and economic analysis of gas production from hydrates by depressurization method." The Canadian Journal of Chemical Engineering 80.1 (2002): 135-143.

[55] Holder, G. D., et al. "A Thermodynamic Evaluation of Thermal Recovery of Gas From Hydrates in the Earth (includes associated papers 11863 and 11924)." Journal of Petroleum Technology 34.5 (1982): 1127-1132.

[56] Bayles, G. A., et al. "A steam cycling model for gas production from a hydrate reservoir." Chemical Engineering Communications 47.4-6 (1986): 225-245.

[57] Ullerich, J. W., M. S. Selim, and E. D. Sloan. "Theory and measurement of hydrate dissociation." AIChE journal 33.5 (1987): 747-752.

[58] Selim, M. S., and E. D. Sloan. "Hydrate dissociation in sediment." SPE Reservoir Engineering 5.2 (1990): 245-251.

[59] Tsypkin, G. G. "Gas hydrate dissociation regimes in highly permeable beds." Journal of Engineering Physics and Thermophysics 63.6 (1992): 1221-1227.

[60] Islam, M. R. "A new recovery technique for gas production from Alaskan gas hydrates." Journal of Petroleum Science and Engineering 11.4 (1994): 267-281.

[61] Castaldi, Marco J., Yue Zhou, and Tuncel M. Yegulalp. "Down-hole combustion method for gas production from methane hydrates." Journal of Petroleum Science and Engineering 56.1 (2007): 176-185.

[62] Van der Waals, J. H., and J. C. Platteeuw. "Clathrate solutions." Adv. Chem. Phys 2.1 (1959): 1-57.

[63] McGuire, Patrick L. Methane hydrate gas production by thermal stimulation. No. LA-UR-81-645; CONF-810317-1. Los Alamos Scientific Lab., NM (USA), 1981.

[64] Goodman, Theodore R. "The heat-balance integral and its application to problems involving a change of phase." Trans. ASME 80.2 (1958): 335-342.

[65] Selim, M. S., and E. D. Sloan. "Heat and mass transfer during the dissociation of hydrates in porous media." AIChE journal 35.6 (1989): 1049-1052.

[66] DiFiore , T. (2013, December 23rd). Eel River Basin Natural Gas and Fracking in Humboldt. Retrieved from: https://www.indybay.org/newsitems/2013/12/23/18748316.php

[67] Collett, Timothy S., and Vello A. Kuuskraa. "Hydrates contain vast store of world gas resources." Oil and Gas Journal 96.19 (1998): 90-94.

[68] Field, Michael E., and Keith A. Kvenvolden. "Gas hydrates on the northern California continental margin." Geology 13.7 (1985): 517-520.

[69] Hoskins, E. G., and J. R. Griffiths. "Hydrocarbon potential of northern and central California offshore." Mem. Am. Assoc. Pet. Geol 15 (1971): 212-228.

[70] Clarke Jr, Samuel H. "Geology of the California continental margin north of Cape Mendocino." (1987).

[71] Krason, J., and M. Ciesnik. "Geological evolution and analysis of confirmed or suspected gas hydrate localities." Basin Analysis, Formation and Stability of Gas Hydrates in the Western Gulf of Mexico.(eds.), US Department of Energy, Washington (1985).

[72] Parker, J.D., 1987. Geology of the Tompkins Hill gas field, Humboldt County, California. In: Schymiczek, H., Suchsland, R. (Eds.), Tectonics, Sedimentation, and Evolution of the Eel River Basin and Other Coastal Basins of Northern California. San Joaquin Geol. Soc. Misc. Publ. 37, 8388.

[73] Kvenvolden, Keith A. "Methane hydratea major reservoir of carbon in the shallow geosphere?." Chemical Geology 71.1 (1988): 41-51.

[74] Field, Michael E., Samuel H. Clarke, and Michael E. White. Geology and geologic hazards of offshore Eel River Basin, northern California continental margin. Vol. 80. No. 1080. US Department of the Interior, Geological Survey, 1980.

[75] Silver, Eli A. "Transitional tectonics and late Cenozoic structure of the continental margin off northernmost California." Geological Society of America Bulletin 82.1 (1971): 1-22.

[76] Oppenheimer, D., et al. "The Cape Mendocino." California, earthquakes of April(1992): 433-438.

[77] Moridis GJ, Collett TS, Dallimore SR, Satoh T, Hancock S, Weatherill B. Numerical studies of gas production from several CH4 hydrate zones at the Mallik

site, Mackenzie Delta, Canada. Journal of Petroleum Science and Engineering. 2004;43:219-38.

[78] Masutani, S.M., Subsea power generation systems utilizing seafloor methane, Final technical report, August 19th 2006.

[79] Milkov, A.V., G.E. Claypool, Y J. Lee, and R. Sassen, Gas hydrate systems at Hydrate Ridge offshore Oregon inferred from molecular and isotopic properties of hydrate-bound and void gases, Geochim. Cosmochim. Acta, 69, 1007-1026, 2005

[80] Milkov, A.V., Molecular and stable isotope compositions of natural gas hydrates: a revised global dataset and basic interpretations in the context of geological settings, Org. Geochem., 36, 681-702, 2005.

[81] Kastner M., K.A. Kvenvolden, and T.D. Lorenson, Chemistry, isotopic composition, and origin of methane-hydrogen sulfide hydrate at the Cascadia subduction zone, Earth Planet. Sci. Lett., 156, 173-183, 1998.

[82] Williams MC, Strakey JP, Surdoval WA. The U.S. Department of Energy, Office of Fossil Energy Stationary Fuel Cell Program. Journal of Power Sources. 2005;143:191-6.

[83] Williams MC, Strakey JP, Singhal SC. U.S. distributed generation fuel cell program. Journal of Power Sources. 2004;131:79-85.

[84] Savaniu CD, Irvine JTS. Reduction studies and evaluation of surface modified A-site deficient La-doped SrTiO3 as anode material for IT-SOFCs. Journal of Materials Chemistry. 2009;19:8119-28.

[85] Luo H, Efimov K, Jiang H, Feldhoff A, Wang H, Caro J. CO2-Stable and Cobalt-Free Dual-Phase Membrane for Oxygen Separation. Angewandte Chemie International Edition.50:759-63.

[86] Pine T, Do A-TV, Zhao L, Brouwer J. Operation of a Novel Dry Hydrocarbon Tolerant Intermediate Temperature Solid Oxide Fuel Cell. ASME Conference Proceedings. 2009; 2009:761-6.

[87] Zhao HL, Gao F, Li X, Zhang CJ, Zhao YQ. Electrical properties of yttrium doped strontium titanate with A-site deficiency as potential anode materials for solid oxide fuel cells. Solid State Ionics. 2009;180:193-7.

[88] Goodenough JB, Huang YH. Alternative anode materials for solid oxide fuel cells. Journal of Power Sources. 2007;173:1-10.

[89] Hauch A, Ebbesen SD, Jensen SH, Mogensen M. Solid oxide electrolysis cells: Microstructure and degradation of the Ni/yttria-stabilized zirconia electrode. Journal of the Electrochemical Society. 2008;155:B1184-B93.

[90] Knibbe R, Traulsen ML, Hauch A, Ebbesen SD, Mogensen M. Solid Oxide Electrolysis Cells: Degradation at High Current Densities. Journal of the Electrochemical Society. 2010;157:B1209-B17.

[91] Schefold J, Brisse A, Zahid M. Electronic Conduction of Yttria-Stabilized Zirconia Electrolyte in Solid Oxide Cells Operated in High Temperature Water Electrolysis. Journal of the Electrochemical Society. 2009;156:B897-B904.

[92] Millet P, Ngameni R, Grigoriev SA, Mbemba N, Brisset F, Ranjbari A, et al. PEM water electrolyzers: From electrocatalysis to stack development. International Journal of Hydrogen Energy. 2010;35:5043-52.

[93] Bird, R. Byron, Warren E. Stewart, and Edwin N. Lightfoot. Transport phenomena. John Wiley & Sons, 2007.

[94] Ji, Chuang, Goodarz Ahmadi, and Duane H. Smith. "Natural gas production from hydrate decomposition by depressurization." Chemical Engineering Science 56.20 (2001): 5801-5814.

[95] Bondarev, E. A., et al. "Mechanics of hydrate formation in gas flows." (1976).

[96] Verigin, N. N., I. L. Khabibullin, and G. A. Khalikov. "Linear problem of gas hydrate decomposition in a porous medium." Izv. Akad. Nauk SSSR, Mekh. Zhidk. Gaza 1 (1980): 174.

[97] Pitzer K. S., Peiper J. C., and Busey R. H. (1984) Thermodynamic properties of aqueous sodium chloride solutions. J. Phys. Chem. Ref: Data 13, l-102.

[98] Shindo, Yuji, et al. "Kinetics and mechanism of the formation of CO2 hydrate."International journal of chemical kinetics 25.9 (1993): 777-782.

[99] (July 19th 2010). "Promise of an Untapped Energy Source". Retrieved from: http://www.slb.com/news/inside_news/2010/2010_0719_gas_hydrates.aspx#The

[100] Peakin, W. (May 8th 2013). A Churchillian dynamic, The North Sea industrys future is bound up in politics, technology - and history. Retrieved from: http://www.holyrood.com/2013/05/28747/

[101] Kvenvolden, Keith A. "Gas hydratesgeological perspective and global change." Reviews of Geophysics 31.2 (1993): 173-187.

[102] Brooks, James M., Michael E. Field, and Mahlon C. Kennicutt II. "Observations of gas hydrates in marine sediments, offshore northern California." Marine Geology 96.1 (1991): 103-109.

[103] Submarine Landslides: Selected Studies in the U.S. Exclusive Economic Zone, U.S. GEOLOGICAL SURVEY BULLETIN 2002, Edited by W.E. SCHWAB, H.J. LEE, and D.e. TWICHELL

[104] Ruppel, C., R. Boswell, and E. Jones. "Scientific results from Gulf of Mexico gas hydrates Joint Industry Project Leg 1 drilling: introduction and overview."Marine and Petroleum Geology 25.9 (2008): 819-829.

[105] Hayre, Ryan O., et al. "Fuel Cell Fundamentals." (2005).

[106] Laguna-Bercero MA. Recent advances in high temperature electrolysis using solid oxide fuel cells: A review. Journal of Power Sources. 2012;203:4-16.

[107] Millet P, Ngameni R, Grigoriev SA, Mbemba N, Brisset F, Ranjbari A, et al. PEM water electrolyzers: From electrocatalysis to stack development. International Journal of Hydrogen Energy. 2010;35:5043-52.

[108] Roberts RA, Brouwer J. Dynamic simulation of a pressurized 220 kW solid oxide fuel-cell-gas-turbine hybrid system: Modeled performance compared to measured results. Journal of Fuel Cell Science and Technology. 2006;3:18-25.

[109] Roberts R, Brouwer J, Jabbari F, Junker T, Ghezel-Ayagh H. Control design of an atmospheric solid oxide fuel cell/gas turbine hybrid system: Variable versus fixed speed gas turbine operation. Journal of Power Sources. 2006;161:484-91.

[110] Mueller F, Brouwer J, Jabbari F, Samuelsen S. Dynamic simulation of an integrated solid oxide fuel cell system including current-based fuel flow control. Journal of Fuel Cell Science and Technology. 2006;3:144-54.

[111] Costamagna P, Selimovic A, Del Borghi M, Agnew G. Electrochemical model of the integrated planar solid oxide fuel cell (IP-SOFC). Chemical Engineering Journal. 2004;102:61-9.

[112] Millet P, Ngameni R, Grigoriev SA, Mbemba N, Brisset F, Ranjbari A, et al. PEM water electrolyzers: From electrocatalysis to stack development. International Journal of Hydrogen Energy. 2010;35:5043-52.

[113] Selamet OF, Acar MC, Mat MD, Kaplan Y. Effects of operating parameters on the performance of a high-pressure proton exchange membrane electrolyzer. International Journal of Energy Research. 2013;37:457-67.

[114] Myles TD, Nelson GJ, Peracchio AA, Roy RJ, Murach BL, Adamson GA, et al. Species transport in a high-pressure oxygen-generating proton-exchange membrane electrolyzer. International Journal of Hydrogen Energy. 2012;37:12451-63.

[115] Marini S, Salvi P, Nelli P, Pesenti R, Villa M, Berrettoni M, et al. Advanced alkaline water electrolysis. Electrochimica Acta. 2012;82:384-91.

[116] Remick RJ, Wheeler D. Reversible Fuel Cell Workshop Summary Report. In: Energy USDo, editor.2011